Structural and Electronic Properties of Tantalum-Based Two-Dimensional Materials

Federico Andreatta

PhD Thesis

Supervisor: Jill Miwa

Aarhus University

Department of Physics and Astronomy

March 2021

«A scientist in his laboratory is not a mere technician: he is also a child confronting natural phenomena that impress him as though they were fairy tales.»

Marie Curie

I dedicate this thesis to my children, Teresa and Miriam.

Abstract

The discovery of graphene marked the beginning of a new research field devoted to study and exploit the properties of materials confined at the two-dimensional limit. Among this class of materials, metallic single layer transition metal dichalcogenides were discovered to exhibit exotic physical phenomena, such as charge density waves or unconventional superconductivity. In this thesis, the charge carriers ultrafast dynamics of two-dimensional tantalum disulphide grown in the 1H structural polymorph are investigated by means of time- and angle-resolved photoemission spectroscopy. The time-dependent photoemission intensity is fitted to an energy- and momentum-resolved model in order to track the intriguing interplay between the band structure modifications and the changes in the electronic temperature. It will be shown how the combination of temperature-induced shifts of the chemical potential and changes in static screening contribute to the temperature-dependent energy shift of the valence band. Moreover, the energy exchange between the charge carriers and the lattice is addressed resulting in the observation of electronic temperature-dependent electron-phonon interaction.

The physical properties of the tantalum-based two-dimensional compounds drastically change upon modification of the chemical composition. For instance, bulk tantalum monopnictides, a class of material comprised of a tantalum and a group V element, were recently found to host Weyl fermions, a novel state of quantum matter. In this thesis, an original growth method is presented for the unprecedented epitaxial growth of single layer tantalum phosphide compounds on low-index gold crystal surfaces. The structural and spectroscopic characterization of the compounds is carried out by a combination of scanning tunnelling microscopy, low-energy electron diffraction and x-ray photoelectron spectroscopy techniques. Intriguingly, several by-products of the reaction are found at the surface, including allotropes of phosphorous and phosphorous-driven reconstruction of the (110) gold surface. The selective growth of an isolated phase of single layer tantalum phosphide compounds could permit the unparalleled study of the electronic properties of a two-dimensional Weyl fermion and open the way to future technologies for the production of green energy.

Resumé

Opdagelsen af grafen var begyndelsen til et nyt forskningsfelt dedikeret til studiet og anvendelsen af egenskaberne i materialer begrænset til den todimensionelle grænse. Iblandt denne gruppe af materialer fandt man, at *metallic single layer transition metal dichalcogenides* udviste eksotiske fysiske egenskaber, som f.eks. *charge density waves* eller ukonventionel superledningsevne. I denne afhandling bliver ladningsbærerne og den ultrahurtige dynamik af todimensionel tantalum disulphid groet i den 1H strukturelle polymorf undersøgt via tids-og vinkelopløst fotoemissionsspektroskopi. Den tidsafhængige photoemissionsintensitet bliver koblet til en energi- og impulsopløst model, så man kan måle det spændende samspil mellem båndstrukturmodifikationer og ændringerne i den elektroniske temperatur. Det vises hvordan kombinationen af temperaturinducerede skift af det kemiske potentiale, og ændringer i statisk screening, bidrager til det temperaturafhængige energiskifte i valensbåndet. Ydermere bliver energiudvekslingen mellem ladningsbærerne og gitteret adresseret, som resulterer i observationen af en elektronisk temperaturafhængig elektron-fonon interaktion.

De fysiske egenskaber ved tantalum-baseret todimensionelle stoffer ændres drastisk ved modificering af den kemiske komposition. For eksempel blev *bulk tantalum monopnictides*, en klasse af materialer bestående af tantalum og et gruppe V-element, for nyligt vist at være vært for Weyl fermioner, en ny tilstand for kvatestof. I denne afhandling bliver en original vækstmetode præsenteret for den uforudsete epitaxiale groning af enkeltlags tantalum phosphid stoffer på lavindeks guld krystaloverflader. Den strukturelle og spektroskopiske karakterisering af stofferne er udført via en kombination af skanning tunnel mikroskopi, lavenergi elektrondiffraktion og røntgen fotoelektron spektroskopi teknikker. Interessant nok blev der fundet adskillige biprodukter ved reaktionen på overfladen, blandt andet en allotrop af phosphoroud og phosphorous drevet rekonstruktion af (110) guldoverfladen. Den selektive vækst af en isoleret fase af enkeltlags tantalum fosfid-stoffer kunne åbne et studie uden sidestykke af de elektroniske egenskaber af en todimensional Weyl fermion, og åbne vejen for fremtidige teknologier i produktionen af bæredygtig energi.

Preface and acknowledgements

This is my PhD thesis in experimental physics which has been submitted to the Department of Physics and Astronomy at Aarhus University in Denmark in order to fulfil the requirements for obtaining a Ph.D. degree in Physics. This work has been supervised by Jill Miwa during the period from August 2017 to February 2021. The experimental part was mainly performed at the SGM3 end-station of ASTRID2 (Aarhus STorage RIng in Denmark 2) but a significant part was carried out in Oxford at the ARTEMIS facility at RAL (Rutherford Appleton Laboratory).

The great physicist Sir Isaac Newton wrote once wrote in a letter "If I have seen further, it is by standing on the shoulders of Giants." What better way to express my gratitude to everyone who has more or less directly contributed to the development of this three-year-long project? I would like, therefore, to start from my supervisor, Jill Miwa, in particular for her boundless kindness and availability. Special thanks go also to Philip Hofmann and Søren Ulstrup, who were of great inspiration while leading me through the project from the accomplishment of the measurements to the drafting of the manuscript. Furthermore, I want to say a big thank you to everyone in the group that welcomed me like a family, especially Marco, who I esteem as an experienced mentor and a very dear friend, and Ann Julie, for her great support during the long experiments performed at the SGM3 end station. Last, but not least, I thank all those friends and relatives that morally supported me though these years, especially my wife, Nicole, and my children, Teresa and Miriam, for their great love.

.....

Federico Andreatta – 01-03-2021

Structural and Electronic Properties of Tantalum-Based Two-Dimensional Materials

Danish: *Strukturelle og Elektroniske Egenskaber af Tantalum-Baseret To-Dimensionelle Materialer*

Italian: *Struttura e Proprietà Elettroniche di Materiali Bidimensionali a Base di Tantalio*

List of publications

Publication relevant for this thesis

- **Transient hot electron dynamics in single-layer TaS_2.** F. Andreatta*, H. Rostami*, A. G. Čabo, M. Bianchi, C. E. Sanders, D. Biswas, C. Cacho, A. J. H. Jones, R. Chapman, E. Springate, P. King, J. Miwa, A. V. Balatsky, S. Ulstrup, P. Hofmann, *Phys. Rev. B*, **99**, 165421 (2019).

Other publications

- **Hot carrier-assisted switching of the electron-phonon interaction in 1T-VSe_2.** P. Majchrzak, S. Pakdel, D. Biswas, A. J. H. Jones, K. Volckaert, I. Marković, F. Andreatta, R. Sankar, C. Jozwiak, E. Rotenberg, *arXiv:2011.06358*.

- **Ultrafast triggering of insulator-metal transition in two-dimensional VSe_2.** D. Biswas, A. J. H. Jones, P. Majchrzak, B. K. Choi, T.-H. Lee, K. Volckaert, J. Feng, I. Marković, F. Andreatta, C.-J. Kang, H. J. Kim, I. H. Lee, C. Jozwiak, E. Rotenberg, A. Bostwick, C. E. Sanders, Y. Zhang, G. Karras, R. T. Chapman, A. Wyatt, E. Springate, J. A. Miwa, P. Hofmann, P. D. C. King, Y. J. Chang, N. Lanata and S. Ulstrup, *Nano Lett.*, In press, (2021).

- **Momentum-resolved linear dichroism in bilayer MoS_2.** K. Volckaert, H. Rostami, D. Biswas, I. Marković, F. Andreatta, C. E. Sanders, P. Majchrzak, C. Cacho, R. T. Chapman, A. Wyatt, E. Springate, D. Lizzit, L. Bignardi, S. Lizzit, S. K. Mahatha, M. Bianchi, N. Lanata, P. D. C. King, J. A. Miwa, A. V. Balatsky, P. Hofmann and S. Ulstrup, *Phys. Rev. B*, **100**, 241406(R) (2019).

- **Low-temperature synthesis of a graphene-based, corrosion-inhibiting coating on an industrial grade alloy.** S. Halkjær, J. Iversen, L. Kyhl, J. Chevallier, F. Andreatta, F. Yu, A. Stoot, L. Camilli, P. Bøggild, L. Hornekær, A. M. Cassidy, *Corros. Sci.*, **152**, 1 (2019).

* These authors contributed equally

Contents

Chapter 1

Introduction

This introductory Chapter aims to give an quick motivation and to provide an overview of the study presented in this thesis. A more specific and detailed contextualization of the materials studied in this thesis will be presented in the first Section of each Chapter.

1.1 Two-dimensional materials

Two-dimensional (2D) materials are defined as *sheet-like* structures whose thickness varies from a single- to few-atomic thick layers [1]. For long time it was questioned whether a 2D crystal could be stable at normal ambient conditions [2]. At the beginning, a single layer (SL) of graphite, namely graphene, was accidentally observed by Auger spectroscopy and low energy electron diffraction (LEED) on platinum [3, 4] and nickel [5], but considered as a surface contaminant arising from carbon segregation from the bulk upon annealing. It was only in 2004 when Geim and Novoselov discovered that graphene could be intentionally singled out from a graphite crystal by means of a scotch tape method [6], granting them the Nobel prize in 2010 [7]. Graphene exhibits outstanding in-plane conducting properties due to its linear band structure whose relative quasiparticle is described by a massless Dirac fermion [8], as predicted by Wallace in 1947 [9].

The experimental discovery of the restricted motion of the electrons in the direction perpendicular to the crystal opened up the possibility to explore new electronic properties of matter that were unknown until then, pushing the scientific community to search into new classes of 2D materials beyond graphene. In 2010, for example, a direct bandgap of about 1.8 eV was found emerging in exfoliated MoS_2 monolayer [10]. This material belongs to the group of tran-

sition metal dichalcogenides (TMDCs) which found a renewed research interested since then [11]. In particular, SL metallic TMDCs were recently found to host exiting physical phenomena, such as charge density waves CDWs [12, 13] [1], unconventional superconductivity [14, 15] and magnetism [16, 17]. Among this class of material SL TaS_2 of the 1H polymorph was isolated in 2016 for the first time and its emerging properties compared to those of its bulk counterpart [18]. Moreover, since graphene semimetallic dispersion can easily be gapped at the Dirac point [19] [2], for example by local sp^3 distortions induced by impurities [20], it is desirable to seek for materials that present a more *robust* quasiparticle electronic state. Topologically protected materials [3], like Weyl semimetals [21], were discovered to be more robust against these kind of non-magnetic perturbations because of their particular form of the Hamiltonian [22]. TaP, for example, was found to host Weyl fermionic quasiparticle in 2015 for the first time [23].

These recent advances in the field of 2D materials brought me to investigate the structural and electronic properties of two different tantalum-based atomically-thick materials, namely TaS_2 and TaP [4]. In the following Section, the results of my investigation will be outlined by introducing the structure of the thesis.

1.2 Thesis outline

The main focus of the work performed and described in this thesis is the growth and characterization of the structural end electronic properties of 2D TaS_2 (Chapter 3 and 4) and TaP (Chapter 5) compounds. In the first paragraphs of each Chapter, a quick outlook of the relevant topics will be provided followed by acknowledgements of the different contributions by the collaborators involved in the project.

[1] CDW is a periodic modulation of the charge density, accompanied by a periodic lattice distortion.

[2] The Dirac point is defined by the energy and momentum location where graphene conduction band meets the valence band

[3] The fact that the topological nature of the band structure is protected means that the *shape* of the vector field represented by the Hamiltonian does not undergo to sudden changes, like *tearing* or *gluing*, under the continuous change of an external perturbing parameter. This implies that the spectrum generated by that Hamiltonian cannot experience a drastic transition, for instance, by opening a band gap in a topologically protected semimetallic electronic state.

[4] On a side note, the transition metal *tantalum* was discovered by the Swedish analytical chemist Anders Gustaf Ekeberg in 1802 [24], who gave this name after the mythical Ancient Greek god Tantalus. According to the mythology the Greek divinity was put into punishment by the other gods where he had to suffer for eternal hunger and thirst by having water and fruits near to him without being able to grasp them. The Swedish chemist named it like that partly to allude to the inability of this metal to, when immersed in abundant acid, absorb it and saturate [24]. Tantalum, in fact, is characterized by chemical inertness and oxidation resistance as well as high melting point, density and strength, making it a good material for high-power resistors or vacuum furnace components.

Chapter 2. The comprehensive characterization of the material properties analysed in this thesis required the adoption of several experimental techniques for the analysis of the surface. Such techniques can be grouped in structural analysis techniques, which include scanning tunnelling microscopy (STM) and low-energy electron diffraction (LEED), and techniques for the analysis of the electronic properties, like angle resolved photoemission spectroscopy (ARPES). Moreover, a description of the facilities where the synthesis and characterization of the sample was carried out will be given at the end of the Chapter.

Chapter 3. At this point, the growth and the time-resolved electronic properties of the two-dimensional layer TaS_2 in the 2H polymorph, when perturbed by an ultrafast pump-probe scheme consisting of laser-based femtosecond time-resolved ARPES (tr-ARPES), are explained. In order to track the changes of the spectrum on an ultrafast scale a novel time-resolved fitting method is developed and presented here for describing the energy- and momentum-resolved photoemission intensity at any time delay. At the end of the Chapter the results from the fit are compared to a theoretical description of the system.

Chapter 4. Here the analysis of the results in Chapter 3 is extended by taking into account the dynamics behind the ultrafast relaxation of the charge carrier density in 2D TaS_2. By fitting the electronic temperature extrapolated in Chapter 3 with a system of coupled differential rate equations, it will be shown that the transient state of the electron distribution can drive a temperature change of the phonons that is mediated by electron-phonon interactions.

Chapter 5. The growth and characterization of SL TaP compounds on a Au(111) substrate will be presented. Moreover, several by-products were also observed whose related structure will be analysed in this Chapter. At the last Section of the Chapter, a similar growth method will be presented, but on the different substrate Au(110). A new reconstruction takes place at the surface of Au(110) and is believed to be triggered by the phosphorous adsorbed on the surface.

Chapter 6. Last, the most relevant results will be outlined again. Furthermore, possible new growth method and characterization strategies will be presented to show the way forward in the research of tantalum-based 2D materials.

Chapter 2

Experimental Techniques

Several experimental techniques were adopted for an exhaustive characterization of the materials studied in this thesis and will be presented in the following section. At last, the basic configuration of the facilities where the synthesis and characterization of the sample was carried out will be illustrated and described. This Chapter is inspired from my master thesis [25], and adapted to the needs of this thesis.

2.1 Analysis of the Surface

The superficial properties of materials are of paramount importance for understanding their potential role in, e.g., heterogeneous catalysis, semiconducting devices or adhesives [26, 27, 28]. Moreover, the advent of 2D materials demanded new tools to probe the electronic and structural properties of interfaces [29]. The investigation of the surfaces studied in this thesis were investigated using microscopy, diffraction and spectroscopy based techniques which will be introduced in the following section.

2.1.1 Scanning Tunnelling Microscopy (STM)

Structural properties of atomically thin materials can be probed locally, down to the atomic level. Nevertheless, the highest resolution of an optical microscope will always be intrinsically diffraction-limited [30] to a spatial resolution as high as 250 nm for visible light, it seems therefore urgent to seek for other techniques that works down to the atomic scale.

STM is a microscopy technique which reaches atomic resolution by imaging the electron local density of states (LDOS) across the sample facilitating a real space image of the electron

density at the surface [31]. If a bias voltage V_b is applied between an atomically-sharp metallic tip and the sample, the LDOS can be retrieved from the leakage tunnelling current I_t which arises by the overlap of the electronic wavefunction of the scanning tip and the one of the locally probed atom/molecule at the surface. Such a highly resolved imaging technique was invented in 1982 by Gerd Binnig and Heinrich Rohrer [32, 33] granting them a Nobel prize. Nowadays, STM is worldly spread and considered as a fundamental technique in surface science.

The link between I_t and LDOS can be modelled by the Tersoff and Hamann approximated formula [34]:

$$I_t \propto V_b \rho_s e^{-2\kappa d} \quad \text{where} \quad \kappa = \sqrt{\frac{2m_e\Phi}{\hbar^2}}, \tag{2.1}$$

where ρ_s, in such approximation, is the LDOS near the Fermi level at the sample surface and d is the tip-sample distance. From the definition of κ it is possible to deduct that, given the electron mass m_e and a typical value for the work function Φ for both the metallic tip and substrate of 4 eV, the decay length is around 1 nm. This means that I_t decreases exponentially with d on a nanometer scale, which entails that small changes in d generate a significant deviation in I_t entailing a surprisingly high resolution, down to 0.1 pm along the z direction [35].

A schematic illustration of the STM working principle according to the quantum mechanical tunnelling interpretation is shown in Fig. 2.1(a). If $V_b = 0$ the alignment of the Fermi levels between tip and sample occurs and I_t does not flow. As soon as $V_b > 0$ electrons will flow from the tip to the surface probing the sample empty states; else, with $V_b < 0$, the filled states of the surface will be probed.

Every STM picture collected during the experiments presented here was scanned with a constant current mode where I_t was self-balanced to reach a set constant value. This is possible thanks to a feedback loop circuit that varies d until the deviation between I_t and the set current is minimized [36]. As the tip approaches the sample a higher number of states will tunnel to/from the sample thereby activating the feedback loop and setting d according to Eq. (2.1). In addition, since according to Eq. (2.1) V_b is proportional to I_t, d is also influenced by the choice of V_b. The raster scanning motion of the tip along the x, y and z directions of the surface is

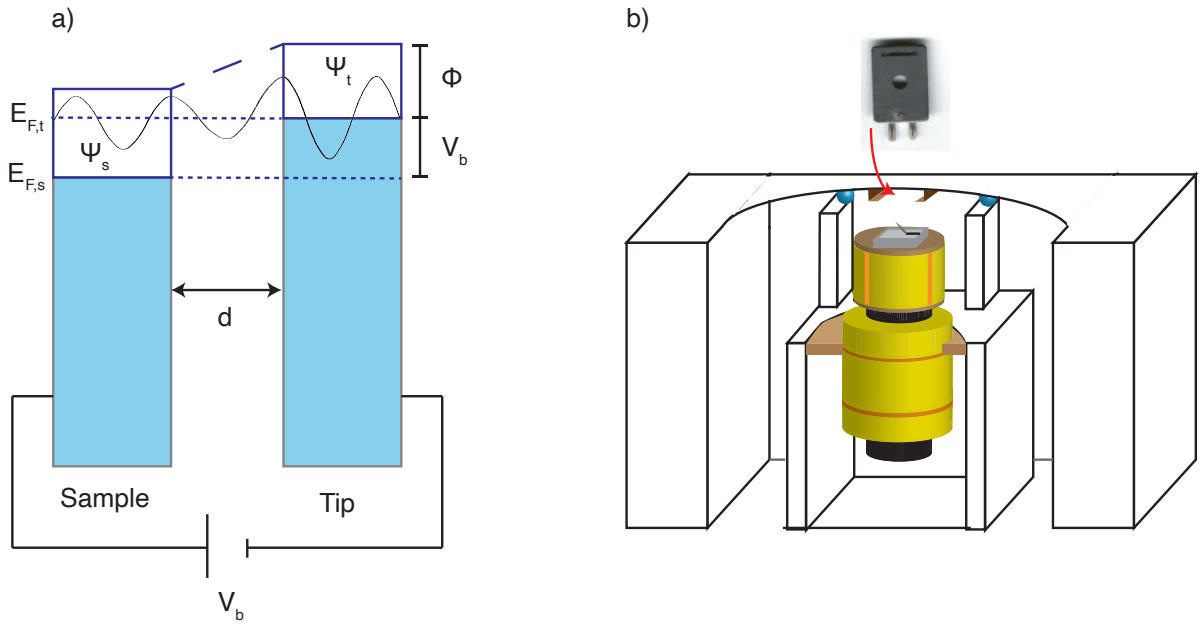

Figure 2.1: (a) Scheme of the energy configuration and representation of the wavefunctions involved during the STM quantum tunnelling. V_b is the bias voltage, d is the tip-sample distance, Φ is the tip workfunction, $E_{F,t}$ and $E_{F,s}$ are the Fermi energies for the tip and sample and Ψ_t and Ψ_s are the wavefunctions for the tip and the sample respectively. In the representation the amplitude of Ψ_t decays exponentially with the thickness of the barrier d as it propagates to the empty states of the sample. (b) Sketch of the Aarhus STM. The supporting shaft is represented by a black cylinder, while the two yellow-orange hollowed cylinders stem for the piezo motor (bottom) and the scanning tube (top), the two balls in blue are insulating bearings and the Macor ring holding the assembly is represented as a brown disk connected to the piezo motor. The sample plate in the picture is inserted under the clamps on the top of the Aarhus STM facing down.

controlled by piezo-electric elements [37]. The feedback loop mediated alteration of d leads to a z(x,y) function with a lateral resolution down to 1 pm. Finally this results in the atomically resolved 2D map of the electron density of state of the sample that is tightly connected with the morphology of the surface. In the current thesis STM was used mainly for the characterization of the surface morphology and of the atomic structures of the different phases at the solid-vacuum interface.

The STM instrument used in this thesis was a home built "Aarhus STM" and its design is represented in Fig. 2.1(b) [38]. The spearhead of the Aarhus STM consists in a rigid and compact design that enables vertical and lateral resonance frequencies as high as 8kHz and 90KHz respectively [39]. This facilitates imaging with very high scanning rate without interfering with

the measurements. The piezoelectric scanner tube shown in the figure is composed of four electrodes (represented in yellow) adherent to a cylindrical shaft (black) which, depending on the voltage applied, allows the fine translation in the x, y and z directions. A linear piezo motor, divided in three coaxial sections, is placed just below, along the shaft's direction, and allows a rough and remote tip approach thanks to an inchworm movement mechanism. The latter is self-limited to a preset value of I_t (0.001 nA) that arises when the tip is in the proximity of the sample. The aluminium block which encloses the piezo motors is held in the UHV chamber by four springs which minimize the background noise coming from external vibrations. Two bearings (blue) provide further electrical, thermal and vibrational insulation between the outer aluminium block and the inner STM house which is connected to the piezo motor through a Macor ring. In this way the STM can be cooled down to 110 K and heated up to 100 K while running at normal operation. The maximum scanning area of $2\mu m \times 2\mu m$ poses a limit of this instrumental technique on addressing the macroscopic structural properties of the sample surface. These can be probed more properly by diffraction techniques as LEED.

2.1.2 Low-Energy Electron Diffraction (LEED)

While STM proves to be an optimal technique when looking at the local structure of the sample, it fails to provide sufficient information concerning its macroscopic structure. LEED, unlike STM, is a diffraction-based structural averaging technique, which means that it gives an average information about the macroscopic order of the analysed surface on a scale of $\approx$ 1 mm [40, 41]. In the present thesis LEED is used as a complementary technique to STM to study the periodic structure and its quality.

The long-scale order of the crystal is studied in LEED thanks to the electron diffraction of a collimated monochromatic electron beam generated by an electron gun and is scattered at the surface. The elastically backscattered diffraction pattern is collected on a fluorescent screen where a set of retarding grids characterized by different applied voltages are adopted to filter inelastically scattered electrons and to focus, as shown in Fig. 2.2.

The electron diffraction takes place because the kinetic energy E_k of the elastically scattered electrons between 10 eV and 300 eV gives the ideal De Broglie wavelength of the order of one

Angstrom, which is comparable to the interatomic distances. Furthermore, the inelastic mean free path IMFP for low energy electrons used in LEED is also on the order of few Angstroms, which means that mostly the surface contributes to the diffraction pattern [42]. Curiously, the IMFP shows a common trend among different materials with respect to the electron energy [43, 44].

The connection between the 2D Bravais lattice describing the periodicity of the crystal surface and the reciprocal lattice associated to the diffraction pattern is ruled by the relation:

$$\mathbf{a}_i \cdot \mathbf{b}_j = 2\pi\delta_{ij} \quad (i,j = 1,2,3), \tag{2.2}$$

where the translation vectors ($\mathbf{a}_1$, $\mathbf{a}_2$) and ($\mathbf{b}_1$, $\mathbf{b}_2$) respectively form the basis of a set of the real space vector $\mathbf{R}$ which describes the direct lattice and the wave vector $\mathbf{G}$ for the reciprocal lattice. This means that any point in the reciprocal lattice can be described by $\mathbf{G} = h\mathbf{b}_1 + k\mathbf{b}_2$, where h and k are the integer Miller indices [45] which stand for a family of lattice straight lines in the 2D lattice defined as diffraction lines. At this point, it is relevant to understand how $\mathbf{G}$ is connected to the diffraction spots coming from the scattered electrons.

In the LEED geometry the electron beam is shoot at normal incidence with respect to the surface, which denotes that the incident wave vector is $\mathbf{k}_{i,\parallel} = 0$. Under this condition, the relation between the reciprocal lattice of the two dimensional crystal and the diffracted spots is straightforward. This is given by Laule conditions of diffraction [46] for a 2D crystal [42]:

$$|-\mathbf{k}_{s,\parallel}| = |\mathbf{G}_\parallel| = d_{hk} = R\sin\theta_{hk} = \frac{R}{|\mathbf{k}_s|}|h\mathbf{b}_1 + k\mathbf{b}_2| = R\frac{\hbar}{\sqrt{2m_e}}\frac{1}{\sqrt{E_k}}|h\mathbf{b}_1 + k\mathbf{b}_2|, \tag{2.3}$$

where R is the distance between the screen and the sample and radius of the LEED screen, θ_{hk} is the angle of the diffracted beam for a given reflection and $\mathbf{k}_s$ is the wave vector at which the elastic scattering occurs. No Laule conditions have to be specified for the momentum component perpendicular to the surface because of the broken periodicity of the crystal in that direction. This could be conceived as a set of straight lines composed of infinitesimally closed spots stemming from the concept of a 2D lattice as a 3D crystal with crystal planes infinitely far from each other.

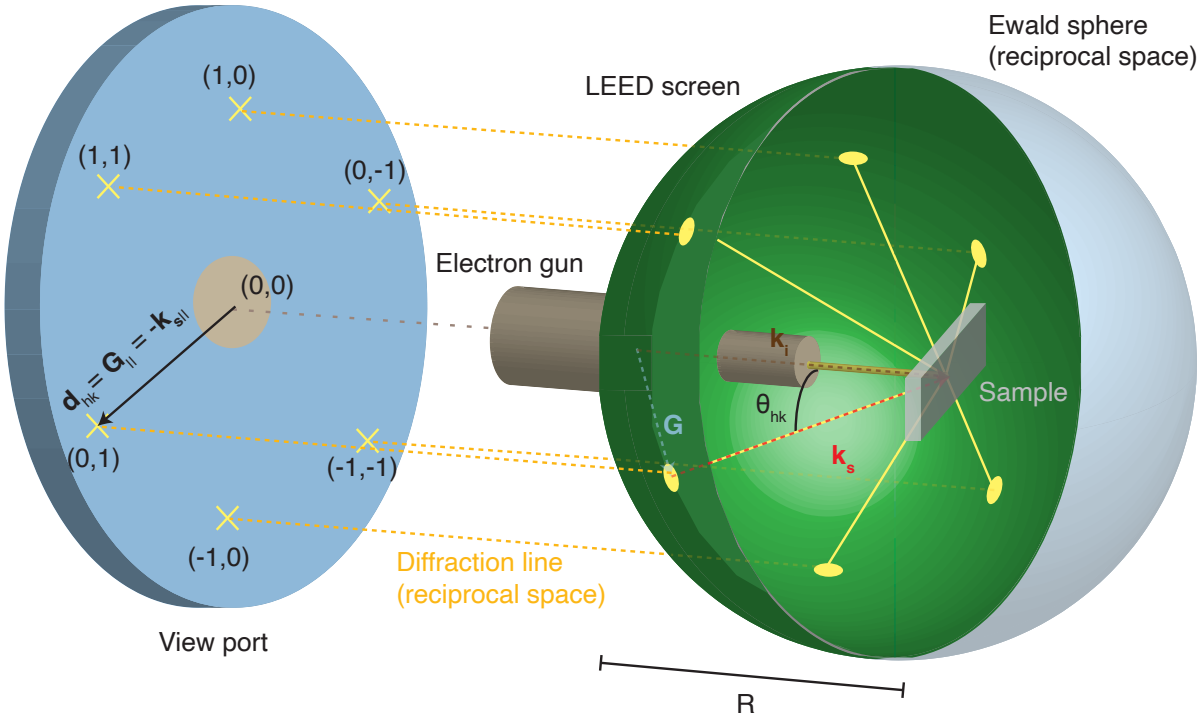

Figure 2.2: Scheme of the LEED apparatus and geometrical construction of the Ewald's sphere (in light blue). An electron gun (brown) shoots monochromatic collimated electron beam into a sample (grey) at distance R from a phosphorous screen (green). The projected diffracted beams in this illustration constitutes an angle θ_{hk} with the normal incidence and is visualised at a reciprocal space distance d_{hk} from the center through the view port. $\mathbf{k}_i$ is the incident wavevector and the radius of the Ewald's sphere, while $\mathbf{k}_{s,\parallel}$ and $\mathbf{G}$ are the scattering wavevector and the reciprocal lattice vector respectively. The miller indices of the diffracted spots projected to the view port are labelled as (h,k).

Fig. 2.2 shows a trigonometric construction which conceptually simplifies the comprehension of the relation between $\mathbf{k}_s$ with θ_{hk} and with $\mathbf{G}$. This is based on the geometrical concept of the Ewald's sphere of radius $|\mathbf{k}_i|$ where $\mathbf{k}_i$ points toward the (0,0,0) 3D reciprocal lattice point at the center of the sphere. In this drawing the Ewald's sphere is overlapped with the LEED's screen for illustration purposes in spite of the fact that the Ewald's sphere is a representation in the reciprocal space while the LEED apparatus is clearly represented in the real space.

As soon as $E_k \propto |\mathbf{k}_i|$ is set by tuning the electron energy of the electron gun, $\mathbf{k}_s$ (red dotted line in Fig. 2.2) will be defined as the vector with modulus $|\mathbf{k}_i|$ and direction determined by the line joining the intersection between the sphere and the diffraction lines (orange dotted lines in Fig. 2.2) with the center of the sphere. In spite of the fact that in this novel representation of the

Ewald sphere the radius $|\mathbf{k}_i|$ might seem constant by changing the electron energy, one should keep in mind that $|\mathbf{k}_i|$ refers to the reciprocal space and varies with E_k while R refers to the real space and is constant. Within this representation it is rather easier to think in terms of the ratio between $|\mathbf{k}_i|$ and sin θ_{hk}. The higher E_k, the bigger the ratio between $|\mathbf{k}_i|$ and sin θ_{hk} and the more diffraction lines would intersect the Ewald sphere. Every time that a diffraction line meets the Ewald sphere diffraction takes place as the Laule condition in Eq. (2.3) is met and $\mathbf{k}_s$ is defined. The diffraction gives rise to a diffraction spot at the LEED screen that can be visualized through a view port. As the reciprocal lattice, labelled by the Miller indices in Fig. 2.2, is formed by the 2D projection of the diffraction lines, a representation of the reciprocal lattice can be obtained by simply imaging a stereographic projection of the LEED screen curvature by placing a camera aligned with the electron beam in front of the view port.

While LEED can provide an accurate description of the lattice parameters of the material investigated, it cannot probe the electronic properties of materials. In this work these properties were investigated by means of photoemission techniques presented in the following section.

2.1.3 Angle Resolved Photoemission Spectroscopy (ARPES)

Important properties of matter such as electrical, magnetic and optical properties are highly determined by the energy dispersion relation of the electrons inside the material. Such energy, defined as binding energy E_{bin}, can be directly probed by photoelectron spectroscopic techniques which are based on the emission of electrons from solids, gases or liquids by ionization from incident photons. This is defined as the photoelectric effect which was first found experimentally by Hertz and Hallwachs in 1887 [47] and theoretically framed by Einstein in 1905 [48] with a quantum mechanical formalism.

Currently, the most sophisticated method for the characterization of electronic structure is ARPES thanks to its ability to map the energy of photoemitted electrons of a given material in the reciprocal space while unveiling information about the collective behaviour of electrons inherent in the photoemission process.

The underlying principles of the photoemission process within an ARPES or a tr-ARPES experiment will be outlined in the following section, while the experimental details concern-

ing the equipment adopted for the accomplishment of the experiments in this thesis will be explained in Sec. 2.2.

Energy and Momentum Conservation in the Three-Step Model

In order to intuitively understand the the underlying principles of photoemission such process can be conceptually divided in three steps in the so-called three-step model, as shown in Ref. [49].

The first step takes place in the electronic states where a monochromatic photon shone onto the sample optically excites an electron from its initial Bloch eigenstates (whose characteristics will be shown in the next section) to a final state in the material, as shown in Fig. 2.3(a). The kinetic energy E_K of the electron's final state depends on how strongly the electron was bonded to the solid in the first place and, therefore, has to fulfil the energy conservation law:

$$E_k = h\nu - E_{bin} - \Phi, \tag{2.4}$$

where $h\nu$ is the photon energy and E_K must be positive so that the work function Φ is the minimum energy required to emit photoelectrons when $E_{bin} = 0$. The energy conservation law is sketched in Fig. 2.3(a)–(c).

Therefore, when $E_{bin} = 0$ in a metal, E_K equals the Fermi energy E_F, that is the energy of the highest occupied state. In other words, when $T = 0$, E_F is the energy at which the total number of states with energy smaller than E_F exactly equals the total number of electrons available in the crystal [50]. Those occupied unlocalised states lying few eV in E_{bin} close to E_F are the ones typically probed by ARPES. These belong to the valence band and determine the electronic properties of a material.

The second step of the three-step model is defined as the migration of the photoelectron to the surface and the consequent probability of a scattering event. When the electron has to travel for distances longer than the IMFP the photoelectron, it will be likely to scatter inelastically changing its momentum and energy. UV light, i.e. photon energies between 5 eV and 100 eV, is commonly adopted to probe the dispersing valance bands near E_F. Under these conditions, for a photoelectron travelling to the surface, an inelastic scattering event occurs every

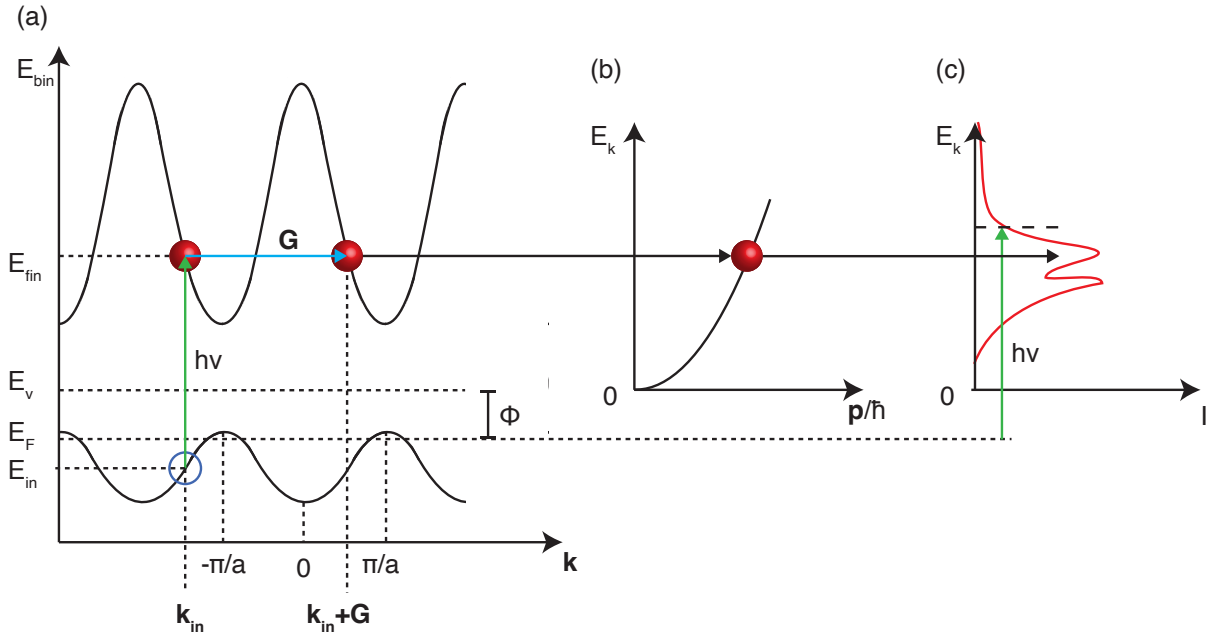

Figure 2.3: The kinematic of the photoemission process represented according to the three-step model with a nearly-free-electron final state (from Ref. [49]). (a) The direct optical transition takes place in step 1 where the electron is excited from a filled state at $E_{bin} = E_{in}$ to a final state at $E_{bin} = E_{fin}$. The Fermi energy E_F, the vacuum energy E_v and the workfunction Φ are also represented. (b) The lattice momentum G is imparted to fulfil step 2 and step 3 where the electron wavefunction propagates through the crystal and matches the free-electron final state in vacuum. (c) The photoelectron spectral intensity is plotted versus its kinetic energy E_k.

5-10 Å, as discussed in Sec. 2.1.2, reason for which ARPES is known as a highly surface sensitive technique. The background intensity in Fig. 2.3(c) is due to the scattering of electrons that happens during step 2

In order to understand the final step of the three-step model, one should take into consideration quantum mechanics and describe the electrons as wavefunctions. According to a standard probability interpretation the wavefunction of an electron is a complex-valued probability amplitude whose modulus square gives the probability density of the electron being found in a certain position in space [51]. It is very important, therefore, to consider how does such a wavefunction looks like for an electron in a crystal.

First of all, considering the crystal as a periodic potential, the electron wavefunction must be also a periodic function in k-space uniquely described by a quantum number n. Such a wavefunction is assumed to be a Bloch function which has the following form [52, 53]:

$$\psi_{n,\mathbf{k}}(\mathbf{r}) = u_{\mathbf{k}} e^{i\mathbf{k}\cdot\mathbf{r}}, \tag{2.5}$$

where $u_{\mathbf{k}}$ is a function characterized by the same periodicity of the crystal. When the Bloch functions are entered as eigenstates in the Schrödinger equation with a periodic potential, the obtained eigenvalues are $E_n(\mathbf{k})$ where both n and $\mathbf{k}$ are quantum numbers. n labels the discrete multiple solutions of the Schrödinger equation for a given $\mathbf{k}$ and each $\mathbf{k}$ leads to a unique solution of the Schrödinger equation. It follows that the function $E_n(\mathbf{k})$, which is the dispersion relation for electrons for the n quantum number, corresponds to a given band and the set $E_n(\mathbf{k})$ correspond to the whole band structure of the crystal.

Secondly, given that the set of $E_n(\mathbf{k})$ describe the band structure inside the bulk, one should consider what happens to the wavefunction when the periodicity is broken in the direction perpendicular to the surface. This is required by the final step of the three-step model, which demands a matching between the electron wavefunction inside the bulk with the free-electron like wavefunction in the vacuum. If the surface is regarded as a simple potential step V generated by the energy offset between the crystal and vacuum, then the $\mathbf{k}$ vector decays in vacuum with its perpendicular component $\mathbf{k}_\perp$ becoming purely imaginary (κ). Under these circumstances the Bloch function at the surface becomes [42]:

$$\psi_{n,\mathbf{k}}(\mathbf{r}) = u_{\mathbf{k}_\parallel} e^{i\mathbf{k}_\parallel\cdot\mathbf{r}_\parallel} e^{-\kappa\cdot r_\perp}. \tag{2.6}$$

The new reformulation of the wavefunction affects the conservation law of the crystal electronic momentum. While the breaking of the translational symmetry of the system at the surface-vacuum interface leads to a change in $\mathbf{k}_\perp$, the parallel component $\mathbf{k}_\parallel$ is conserved, i.e. $\mathbf{k}_{\parallel,out} = \mathbf{k}_{\parallel,in}$, as it can be seen in Fig. 2.4. Note that the momentum contribution imparted by the photon ($|\mathbf{k}_{ph}| = \frac{2\pi}{\lambda} \approx 0.05\text{Å}^{-1}$ for $E_{ph} = 100eV$) is negligible compared to the usual dimensions of the BZ ($|\mathbf{k}_{BZ}| = 2\pi/|\mathbf{r}| \approx 2.5\text{Å}^{-1}$ for graphene), therefore the additional momentum necessary for the electron to match the vacuum free-electron state is imparted by the crystal potential, as pointed out before [54].

In synthesis, the interpretation given by the three-step model allows to retrieve with a common ARPES experiment the original information concerning $\mathbf{k}_\parallel$ of an electronic state, as well its E_{bin}. The way in which the resulting band mapping is carried out will be matter of discussion

in the next section.

The ARPES experiment

When the photoelectron from a given band leaves the surface it carries E_k which depends on $\mathbf{k}_\parallel$, i.e. $E_k(\mathbf{k}_\parallel)$. The detection of $E_k(\mathbf{k}_\parallel)$ is accomplished by shooting an intense monochromatic light from a laser or a synchrotron radiation source in UHV on the sample and by detecting the ejected photoemitted electrons with a hemispherical analyser, as drawn in Fig. 2.4. The spherical azimuthal φ and polar θ coordinates are used to retrieve $\mathbf{k}_\parallel = (k_x; k_y)$ through the following equation [49]:

$$\mathbf{k}_{\parallel,in} = \mathbf{k}_{\parallel,out} = \mathbf{k}_\parallel = \mathbf{k}_x + \mathbf{k}_y = \frac{\sqrt{2m_e E_{kin}}}{\hbar} \sin\theta(\cos\varphi\hat{\boldsymbol{x}} + \sin\varphi\hat{\boldsymbol{y}}). \tag{2.7}$$

Unfortunately, the classical spherical coordinates φ and θ are impractical to be directly evaluated within the ARPES geometry, therefore the emission azimuthal angle ϕ and the emission polar angle Θ are preferably employed as transformed basis for the equivalent representation of $\mathbf{k}_\parallel$ as it can be seen in Fig. 2.4:

$$\begin{aligned} k_x &= \frac{\sqrt{2m_e E_{kin}}}{\hbar} (\cos(\alpha)\sin(\phi) - \sin(\alpha)\cos(\Theta)\cos(\phi)) \\ k_y &= \frac{\sqrt{2m_e E_{kin}}}{\hbar} \cos(\Theta)\sin(\phi), \end{aligned} \tag{2.8}$$

where α is defined as the tilt angle.

An emission azimuthal angle range $[-\beta; +\beta]$ is selected by the analyser along the plane orthogonal to the mirror plane of the analyser, defined as dispersive plane, by an entrance slit aperture downstream of a set of electrostatic lenses. The set of electrostatic lenses influences the range $[-\beta; +\beta]$ depending on the field applied. Moreover, the $\mathbf{k}_\parallel$ resolution depends on the $[-\beta; +\beta]$ selected range but also on the polar angular resolution, which is determined by the acceptance angle in the direction orthogonal to the entrance slit, according to the following formula:

$$\Delta k_\parallel = \sqrt{\frac{2m_e E_k}{\hbar^2}} \cos\Theta\Delta\Theta. \tag{2.9}$$

However, the most important role of the lenses is to retard the electrons linearly so that the

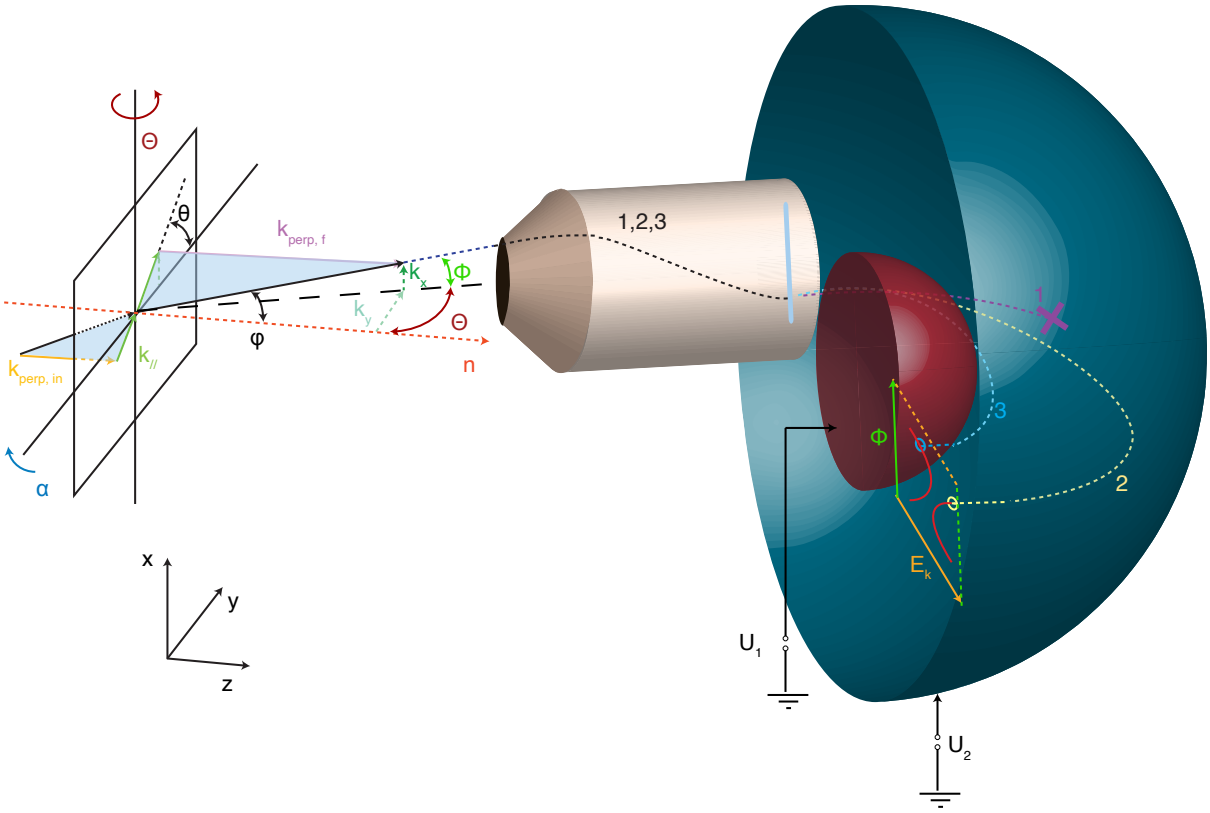

Figure 2.4: Illustration of the photoemission process and of the measurement working principle. The conservation of $\mathbf{k}_{||}$ during the refraction at the interface on the left side alongside the non-conservation of $\mathbf{k}_{perp}$. Furthermore, the $\mathbf{k}_x$ and $\mathbf{k}_y$ components of $\mathbf{k}_{||}$ are represented in the figure. θ and φ are the polar and azimuth angles conventionally adopted in a spherical coordinate system and implemented in Eq. (2.7), whereas Θ, ϕ and α are the polar and azimuth emission angle and the tilt angle respectively which are used in Eq. (2.8). The electrostatic lenses of the analyser are represented in grey, the entrance slit in light blue and the hemispheres in blue and red with where two different negative potentials are applied so as to form a bandpass filter. A representative exemplification of three electrons being collected in the analyser is shown and explained in the text.

ones with the energy of interest E_k enter the hemispheres with an energy E_p. Once the electrons go beyond the entrance slit they feel an electric field produced by the two hemispherical deflectors which deviates the electron path according to their E_k along the mirror plane of the analyser defined as dispersive plane. Here, the electric field produced by the two hemispherical deflectors causes the incoming electrons path to be split according to their kinetic energy. Thus, the deflectors act as pass energy filter which directly determines the interval of kinetic energy selected $E_p \pm \Delta E$, where $\Delta E \propto E_p$, and the energy resolution of the analyser which is given by:

$$\delta E_a = \frac{E_p(S_1 + S_2)}{4R}, \tag{2.10}$$

where R is the mean radius of the analyser and S_1 and S_2 are respectively the widths of the entrance and exit slits.

After the photoelectrons have passed through the hemispheres they pass through an exit slit where a multichannel plate is used to increase their signal before getting accelerated towards a phosphorous screen. Finally, a CCD detector captures the image that is there formed by the photoemitted electrons.

In order to show the working principle of ARPES a simple scenario is represented in Fig. 2.4. Three electrons (1, 2 and 3) with the same $\mathbf{k}_\parallel$ but different E_k are emitted in the (ϕ, Θ) direction, collected through the electrostatic lenses and projected on the phosphorous screen according to their E_k. Electron 1 has an energy of $E_{k,1} > E_p + \Delta E$, where both E_p and ΔE are determined by the applied potential U to the outer hemisphere of the analyser, and therefore it will collide with the outer hemisphere. Electron 2 and electron 3 have an energy of $E_p - \Delta E < E_{k,3} < E_{k,2} < E_p + \Delta E$, therefore electron 2 will travel a longer path because of his higher E_k and, by doing so, the energy resolution is achieved. The result is a 2D "slice" of $E_k(\mathbf{k}_\parallel)$ projected in the 2D detector, as represented in Fig. 2.4, where E_k is acquired as a function of ϕ. In a common ARPES setup, a larger portion of $E_k(\mathbf{k}_\parallel)$ is captured by rotating Θ in steps in order to form a 3D dataset designated as "angle scan" which portraits the photoemission intensity $I(\Theta, \phi, E_k)$. Finally, a transformation of basis from the two angular components ϕ and Θ to $\mathbf{k}_\parallel = (k_x; k_y)$ is performed according to Eq. (2.8) so that the final representation of the photoemitted intensity is given as $I(\mathbf{k}_\parallel, E_{bin})$. This transformation will be later on referred to as k-warping.

Final and Initial States Contribution to the Intensity

A full description of the photoemission process requires more than the energy and momentum conservation laws, as shown in Ref. [49]. In particular, during the first step of the photoemission, the symmetry of the initial and final states has remarkable consequences on $I(\mathbf{k}_\parallel, E_{bin})$. The photoemission intensity is not only influenced by the initial and final state of the single-particle electron, but also by the ones of the hole left behind in the valence band, namely the photohole. Such a photohole, indeed, could be filled again by an electron thanks to interactions

with other electrons or through the lattice. Clearly, the single-particle picture that was adopted until now cannot be satisfactory any more and the photohole interacting with the remaining particles should be rather considered like a new entity *as a whole*. Such an entity is classified as quasiparticle which entails many-body effects that can be deduced from the ARPES photoemission intensity. The connection between $I(\mathbf{k}_{\parallel}, E_{bin})$ and many-body effects can be explained with the following mathematical interpretation.

In a first assumption, the photoelectron is regarded as a non-interacting particle described by single-particle wave functions for the initial $\phi_i^{\mathbf{k}}$ and final $\phi_f^{\mathbf{k}}$ state. Furthermore, the photohole left behind is regarded as a system with (N-1) electrons Ψ_i^{N-1} which could be later found at a certain ionization state Ψ_m^{N-1}. Because of the non-interacting nature of $\Phi_{i,f}^{\mathbf{k}}$ the factorization of the total initial and final wavefunctions is readily applied such that $\Psi_i^N = \phi_i^{\mathbf{k}}\Psi_i^{N-1}$ and $\Psi_f^N = \phi_f^{\mathbf{k}}\Psi_f^{N-1}$. The way in which these initial and final states influence the first step of the photoemission process is mediated by the external magnetic field ruled by the perturbation Hamiltonian H_{int}. The rate of optical transitions is determined by Fermi's golden rule in the following way [55]:

$$\begin{aligned}\Gamma_{f\leftarrow i} &= \frac{2\pi}{\hbar}|\langle\Psi_f^N|H_{int}|\Psi_i^N\rangle|^2\delta(E_f^N - E_i^N - h\nu) \\ &= \frac{2\pi}{\hbar}|M_{i,f}^{\mathbf{k}}|^2|\langle\Psi_m^{N-1}|\Psi_i^{N-1}\rangle|^2\delta(E_k + E_m^{N-1} - E_i^N - h\nu),\end{aligned} \tag{2.11}$$

where the matrix elements $M_{i,f}^{\mathbf{k}} = \langle\phi_f^{\mathbf{k}}|H_{int}|\phi_i^{\mathbf{k}}\rangle$ representing the density of probability of the single photon to excite a single electron in a state f, depends on the light polarization and optical selection rules between the final and initial state of the photoelectron wavefunction crossection. This probability density is combined to the one of the photohole of being left in the ionized state m following the excitation $|\langle\Psi_m^{N-1}|\Psi_i^{N-1}\rangle|^2$ and to the energy conservation law expressed by the last factor of Eq. (2.11). The likelihood of the optical transition event must be related to the observed intensity:

$$\begin{aligned}I(\mathbf{k}, E_k) &\propto \sum_{f,i}\Gamma_{f\leftarrow i}f_{FD}(E_k) \\ &= |M_{i,f}^{\mathbf{k}}|^2\mathcal{A}(\mathbf{k}, E_k)f(E_k, T),\end{aligned} \tag{2.12}$$

where $f(E_k, T)$ is the temperature dependent Fermi-Dirac distribution function and the second term is the so-called photohole spectral function which, from Eq. (2.11), is defined as:

$$\mathcal{A}(\mathbf{k}, E_k) = |\langle \Psi_m^{N-1} | \Psi_i^{N-1} \rangle|^2 \delta(E_k + E_m^{N-1} - E_i^N - h\nu) \tag{2.13}$$

The advantage of writing the spectral function as in Eq. (2.12) is that the photoemitted intensity is directly linked to many-body effects through the spectral function. In fact, the spectral function can be rewritten using a Green's function formalism in the following way [49]:

$$\mathcal{A}(\mathbf{k}, \omega) = \frac{\pi^{-1} |\Sigma''(\omega)|}{(\hbar\omega - \epsilon(\mathbf{k}) - \Sigma'(\omega))^2 + \Sigma''(\omega)^2} \tag{2.14}$$

where $\epsilon(\mathbf{k})$ represents the single-particle energy distribution without any interaction, the so called *bare band*, $\hbar\omega$ is the binding energy and $\Sigma(\omega)$ is the electronic self-energy with real part $\Sigma'(\omega)$ and imaginary part $\Sigma''(\omega)$ that are connected to each other by Kramers-Kronig relations [56, 57]. The electronic self-energy could be conceived as a E_b dependent incremental energy that quantitatively describes the the many-body effects of the photohole. In particular, the real part addresses information about the change in band velocity and the consequent shift in binding energy of the dispersion with respect to the single-particle bare band structure, which is defined as "renormalization" of the bare band. Moreover, the imaginary part describes the lifetime of the quasiparticle linked to possible many-body scattering processes between the photoemitted electrons and phonons, impurities or other electrons. This is experimentally observable thanks to a change in width of the band which is inversely proportional to the lifetime of the quasiparticle [58].

Time- and Angle- Resolved Photoemission Spectroscopy

Until now it was tacitly assumed that electrons are at their equilibrium state before being photoemitted. However, if the electronic structure could be manipulated by a perturbation and measured in that excited state, new out-of-equilibrium electronic properties would be explored. Such a goal requires not only resolution of the electronic structure in energy and momentum, but also in time.

Time- and angle-resolved photoemission spectroscopy is a state-of-the-art technique that probes the responses of an optical excitation on the material band structure. This is essen-

tially achieved by a collinear and temporal overlap of infrared IR and extreme ultraviolet XUV ultrashort pulses, whose time duration is on the order of femtoseconds (10^{-15} s) [59] or sub-femtosecond time scale [60]. In such a setup, the first pulse grants the energy to excite the electron population inducing electron-hole pairs which could be seen as resonant collective excitations, the latter probes this transient electronic structure by transferring enough E_k to observe the band dispersion at sufficiently high $\mathbf{k}_{\parallel}$ after being collected in the hemispherical analyser, as in Fig. 2.4. The time domain is added by setting a tunable time delay between the pump and the probe pulse. While the time resolution is related to the duration of the pulse, the energy resolution, according to Heisenberg principle for which $\Delta E \Delta t > \frac{\hbar}{2}$, is inversely proportional to that. However, when the time duration of the pulse is around 10 fs, the energy resolution is typically limited by experimental components [61].

In this way it is possible to probe the transient unoccupied state, which is normally inaccessible by means of standard ARPES, and explore its dynamical relaxation to its equilibrium state. Furthermore, in a standard ARPES experiment, the properties of the quasiparticles are addressed only on the energy domain. The addition of the time dimension paves the way to observe quasiparticle dynamics by tracking their evolution within their characteristic time-scales. This allowed materials such as high temperature superconductors [62] or CDW driven materials [63] to unveil their quasiparticle behaviour at the ultrafast scale.

It was only recently that ultrashort pulses were achieved in the XUV regime [64] thanks to the high harmonic generation (HHG) technique. This consists of a three-step "rescattering" model [65] based on the non-linear interaction of intense visible or IR femtosecond light pulses with a pulsed jet of many-electron noble gasses like in Fig. 2.5(a) and can be summarised as follows:

1. a rare gas atom is ionized thanks to quantum mechanical tunnelling effect induced by the laser field suppression of the Coulomb potential barrier which corresponds to the electron E_{bin}.

2. The polarity of the electric field switches after half an oscillation cycle of the laser field causing the electron to be attracted toward the ionized atom with a higher E_k. The exceeding E_k that can be gained after the ionization is $3.17\frac{E^2}{2\omega^2}$, where E and ω are the electric field and the fundamental frequency of the laser.

3. The electron experiences a recollision with ion and a higher energy photon is emitted with respect to the frequency of the driving field. This is define as the *recombination process*.

This light source is characterised by a discrete spectrum of odd harmonics that can reach a cutoff energy up to 100 eV. An example is shown in Fig. 2.5(c) [66]. Not only the HHG spectrum provides a wide $\mathbf{k}_{\parallel}$ range which gives access to electronic features far from the center of the BZ, but it also provides a tunable set of photon energies which, according to Eq. (2.12), opens up the possibility to study matrix elements effects on the photoemitted intensity [67]. A drawback of this technique is that when an ultrashort laser pulse is shone on the material it generates electron bunches of high charge density which decrease the momentum and spectral resolution and cause a shift in the electron kinetic energy. This is defined as space charge effect [68, 69, 70] and it carries an energy broadening ΔE that is proportional to $\sqrt{N}$ where N is the number of photoelectrons per pulse [68], which in turn is proportional to the pump fluence. [70, 71].

2.2 The ARTEMIS end station and the SGM3 beamline

The main facilities used for the accomplishment of the experiments will be introduced in the following section.

2.2.1 The SGM3 beamline at ASTRID 2

The end station of the SGM3 beamline is located at the Aarhus STorage Ring facility In Denmark (ASTRID 2) [72] and is represented in Fig. 2.6. SGM3 Beamline hosted the STM, LEED, and ARPES characterization of the samples. ASTRID 2 is a hexagonal 580 MeV synchrotron which delivers XUV energy radiation [73]. The current is kept constant in a top-up mode at 180 mA by means of a top-up injection mechanism in connection to the booster synchrotron ASTRID [73]. In order to emit linearly polarized radiation with higher brilliance the electron beam in ASTRID 2 passes through an undulator. This consists of two parallel arrays of magnets with alternating polarity constraining the electrons to follow a sinusoidal trajectory [72]. Thanks to the tunable gap between the magnets arrays the photon energy can be varied between 10 eV and 150 eV while the acquisition of the photoemitted intensity is taking place. The result is the so-called "photon-energy scan" which allows to explore the $h\nu$ dependent matrix element effects, as it was explained in the previous section.

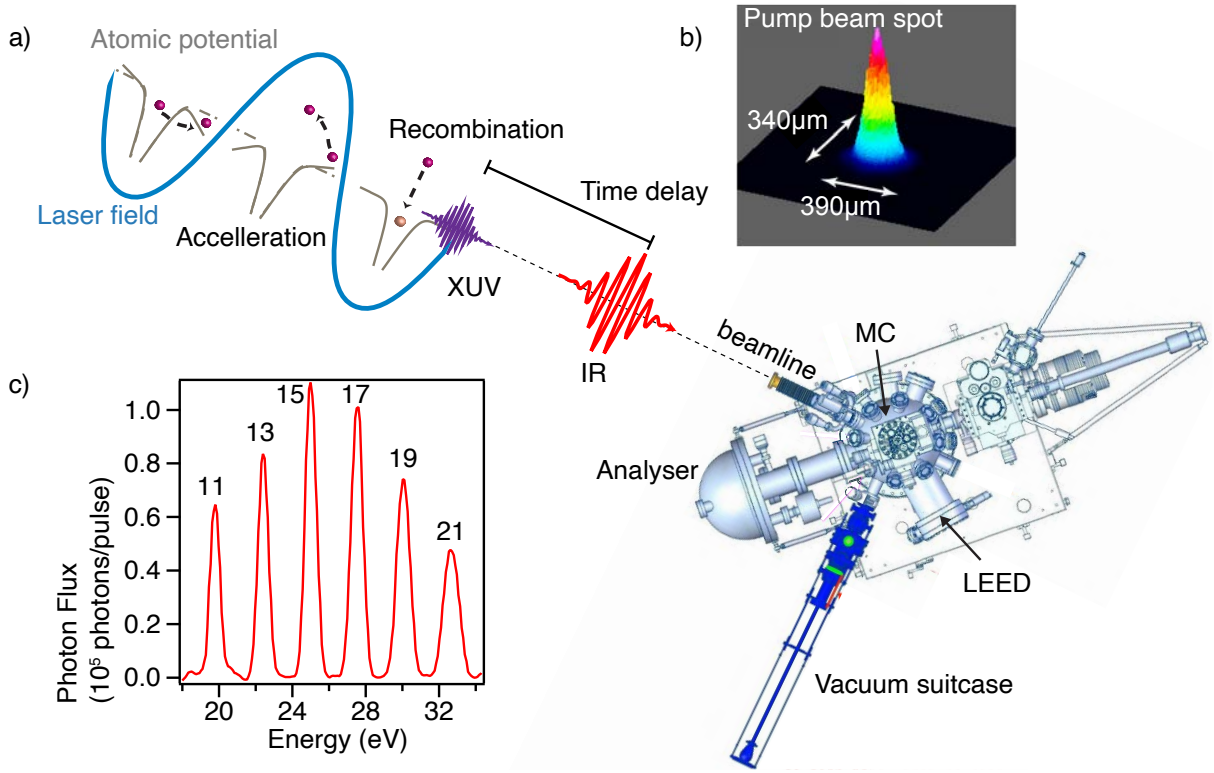

Figure 2.5: (a) The three-step "rescattering" model generating the HHG spectrum in panel (c). A time delay is set between the IR and the XUV pulses that enter into the ARTEMIS endstation and activate the photoemission process like in Fig. 2.4. Courtesy of Cephise Cacho. (b) The spot profile of the pump beam with an energy of 2 eV measured by means of a CCD camera. (c) An example of a HHG spectrum where the energy is plotted versus the photon flux [66].

When ARPES measurements are performed the light is focused and aligned on the sample in the μ-metal main chamber (MC) of the end station through a series of mirrors and slits. A high level of control over the sample movements is required when acquiring an angle scan. This is granted by a fully remotely controlled 6-axis manipulator with a socket where the sample plate can be mounted. The manipulator is equipped with diode, a tungsten filament heater and a closed-cycle He cryostat that allows sample cooling down to $T = 30$ K, while a thermocouple is spotwelded on the rear side of the crystal. The SPECS Phoibos 150 hemi-spherical analyser in the MC allows the acquisition of ARPES spectra following the explanation in Sec. 2.1.3. The LEED optics are also found in the MC, where a base pressure of 5×10^{-11} mbar is kept thanks to a pumping system based on a Ti sublimation pump, a cryo-pump, an ion-pump, a NEG-pump (Non-Evaporable Getter pump) . Furthermore, the MC can also be pumped by the turbo pumps belonging to the two neighbouring preparation chambers PC1 and PC2 where the sample can be transferred. The Aarhus STM is located in PC1 where the Au surface treatment and the

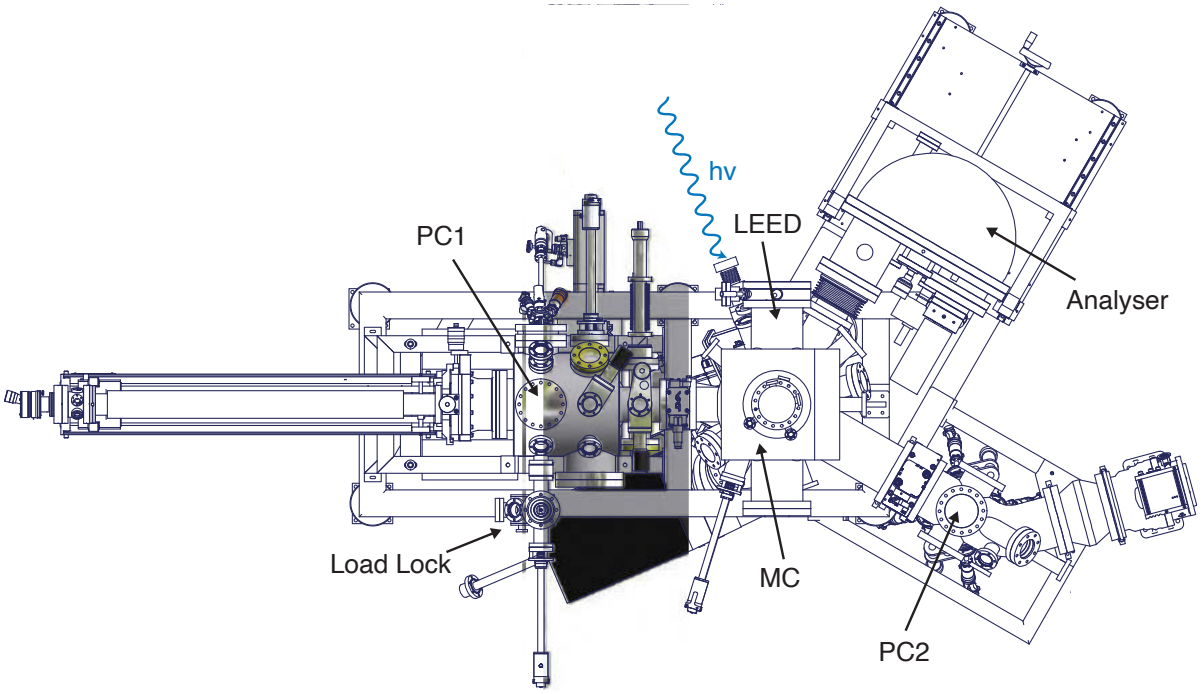

Figure 2.6: Top view of SGM3 end station at ASTRID 2. SGM3 is characterized by LL, MC, PC1 and PC2 chambers separated by valves. Aarhus STM is located in PC1 while LEED and ARPES measurements were carried out on the 6-axis manipulator in MC. The synchrotron radiation with a photon energy *hν* (blue) is projected toward the sample in MC through SGM3 beamline (not shown here).

growth of SL TaP compounds was accomplished, whereas the growth of TaS_2 was done in PC2 where H_2S gas was dosed through a gas line and Ta was evaporated through electron beam heating of a Ta rod from SPECS Gmbh. Both PC1 and PC2 are equipped with a load lock (LL) that allows the insertion of the sample in the vacuum system without venting the preparation chambers. When transferred to a different end station, the sample was transported in a home built vacuum suitcase, coloured in blue in Fig. 2.5(a). The vacuum suitcase was equipped with an ion pump connected to a battery and a passive NEG-pump which prevented contamination of the TaS_2 during its transportation thanks to a base pressure of 5^{-10} mbar.

2.2.2 The ARTEMIS end station at CLF

ARTEMIS is the end station for ultrafast XUV science, shown in Fig. 2.5(a), located at the Central Laser Facility at the Rutherford Appleton Laboratory in the UK. Here the tr-ARPES on the SL TaS_2 was performed. The light source is a high repetition rate (1 kHz) Ti:Sapphire amplified

laser system operating at 780 nm with a typical output power of 12 W and a FWHM duration of 30 fs per pulse [74]. The laser power is split in two paths where 20% of the laser is driven into a gas cell with pulsed Ar gas jet for the HHG. The rest of the power is used in an optical parametric amplifier (HE-Topas) that provides ultrashort pulses covering the spectral range from 235 nm to 15 μm . A considerable issue lies in the working principles of actual monochromators for which the wavelength selection entails a temporal broadening. A new monochromator was designed in collaboration with the University of Padova (Italy) [75] in order to separate high-order-harmonic pulses with high intensity and defined photon energy while preserving their time duration by placing a diffraction grating in between two toroidal mirrors. The pulses are delivered in a synchronised manner through vacuum to the end station thanks to a mechanical delay line. Here, the delay for which the pump and probe pulses reach the sample surface at the same time, namely "time 0", is set. Finally, the photoemitted electrons are collected in a hemi-spherical electron energy analyser (SPECS Phoibos 100). The ARTEMIS end station is capable of capturing electron dynamics on a 30 fs timescale with an energy resolution of 150 meV [76]. The probe beam has a typical size of 100 μm $\times$ 150 μm. This must be spatially overlapped with the slightly bigger pump beam, shown in Fig. 2.5(b), by manual alignment. A critical parameter for the experiment is the fluence of the pump beam $F = \left(E_{pulse} \cos\theta_{incidence}\right) / A_{beam}$, since it is related to the number excited carriers as it will be shown later.

Chapter 3

Electron dynamics in a 2D metal: tr-ARPES of TaS_2 on graphene

This chapter aims to explain the growth and describe the electronic structure characterization of the two-dimensional layer TaS_2 in the 2H polymorph. The perturbation of the electronic structure, including the transient state and relaxation dynamics, was investigated by means of laser-based femtosecond tr-ARPES. A novel method is developed and presented here for fitting the full $\mathcal{I}(E, \mathbf{k})$ at any time delay. This method allows for changes of the spectrum to be tracked on an ultrafast scale. At the end of this chapter the results from the fit are compared to a theoretical model of the system.

The experimental determination of the transient dynamics was accomplished at ARTEMIS laser facility in the UK, while the STM and static ARPES data were acquired at the SGM3 endstation at ASTRID2 in Denmark. This chapter shows the results and follows the structure of the publication in Ref. [77], however it is expanded and adapted to fit the style and contents of this thesis. Therefore, in some sections of this Chapter the formulation of the text may be very similar to that of Ref. [77]. The STM data in Sec. 3.2 and the tr-ARPES data presented in Sec. 3.4 and 3.5 were acquired during my master thesis project [25], however the analysis of the data was fully carried out during the PhD project and all the relevant results are introduced here for the first time (after the publication in Ref. [77]). My main contribution to this project was growing the sample at the SGM3 beamline and performing the measurements at ARTEMIS with coworkers, as well as analysing the experimental data with Søren Ulstrup with whom I was also co-writing the paper mainly together with Habib Rostami, Jill Miwa and Philip

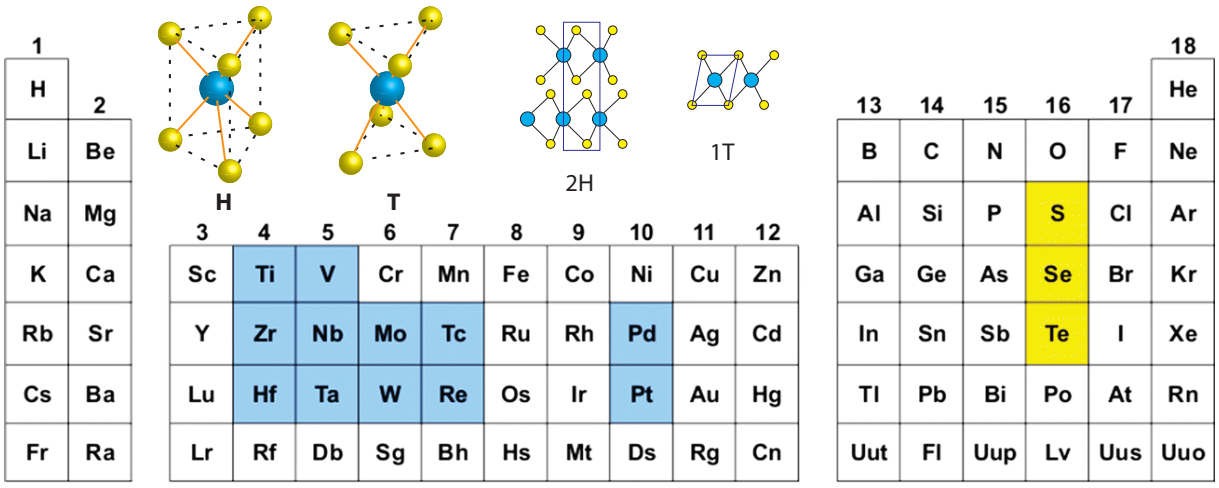

Figure 3.1: Periodic table of the elements. The blue and yellow color highlight the layered transition metal M and chalcogen X, respectively, that could possibly take part in the formation of the MX_2 TMDCs. The two coordination geometries T and H and the typical unit cells 1T and 2H are sketched at the top (adapted from Refs. [82, 25]).

Hofmann. All the theoretical calculations shown at the end of the chapter were performed by Habib Rostami, who was first author of the paper alongside with myself.

3.1 Bulk and two-dimensional metallic TMDC

The scientific research on TMDCs in the bulk form is dated back to the 1960s. In fact, bulk TMDCs were studied as they exhibited several physical properties such as exciton screening, d-band formation, metal to insulator transitions, magnetism and superconductivity [78]. These compounds are characterized by chemical formula MX_2, where M is the transition metal and X the chalcogen, as shown in Fig. 3.1. Solely 40 out of the 100 existing bulk TMDCs are layered and structured in a sandwich-like manner consisting of a mid-layer of a transition metal (M) sandwiched between two layers of chalcogens (X) [79, 80]. The metal atoms share four electrons with the two chalcogens; thus the oxidation state for M is +4 and for X is -2. Typical unit cells of TMDCs are labelled as 1T or 2H, as represented at the top of Fig. 3.1. According to this notation, the number stems from the number of layers needed to complete one unit cell and the letter *T* and *H* represent the octahedral and trigonal prismatic coordination, respectively. The weak van der Waals interactions between adjacent atomic sheets result in easy exfoliation of the layers leading, among other things, to excellent lubricant properties [81].

Among this class of materials, metallic TMDCs [83] (like TaS_2, $TaSe_2$, $NbSe_2$, VS_2, VSe_2,

etc.) typically manifest exotic physical properties in their bulk states, such as CDWs [12, 13] [1], unconventional superconductivity [14, 15] and magnetism [16, 17], as pointed out in Sec. 1.1. Metallic TMDCs recently experienced a surge in research interest due to the discovery of changes of the collective electronic states that arises when this class of material is confined to two dimensions, including drastic changes in CDWs and superconductivity critical temperatures [84, 85]. TaS_2 of the 2H polymorph (2H-TaS_2), for example, was observed exhibiting a enhancement of the superconducting critical temperature upon 2D confinment [18, 86] which was attributed to a boost of the electron-phonon coupling constant [18] or to a reduction of the CDWs amplitude [86]. In general, the discovery of 2D metallic TMDCs could open up the potential applications that are only engineered with graphene to date [83] like energy conversion/storage devices [87], electrodes [88] or photodetectors [89]. In particular, 2D metallic TMDCs are believed to have the potential to supplant their semiconducting counterpart as catalysts due to their superior electrical conductivity and abundant catalytic active sites [90, 91].

The electronic states within 2D metallic TMDCs can be regarded as a 2D electron gas (2DEG), which could be drastically altered and driven into distinct phases by the application of external fields. Phase transitions can occur while tuning the electron-electron interactions by controlling the electric field in high electron mobility transistors [92, 93]. When such systems are tuned into extreme conditions, electronic instabilities, such as a metal-insulator transition [94] or unconventional superconductivity [95], can emerge. Even when simply doped by adopting different substrates or adsorbates, a Fermi level shift on the order of electron volts can be induced in semimetallic 2D materials such as graphene [96, 97, 98, 99], providing access to the relation between the electronic self-energy and the electron/hole density over a wide energy range [100]. In principle, the electronic self-energy is also temperature dependent, but such effects are usually negligible because $k_B T$ at usual experimental temperatures tends to be much smaller than the electronic bandwidth [101, 102]. In order to test this dependence, narrow electronic bandwidths or high electronic temperatures are required. These conditions are ideally met in 2D systems where non-trivial temperature effects are expected to give access to density-dependent many-body phenomena [103, 104].

A vast range of transient electronic temperatures can be accessed by employing an intense and ultrasfast optical excitation in a pump-probe scheme such as tr-ARPES to drive (semi)

[1] CDW is a periodic modulation of the charge density, accompanied by a periodic lattice distortion.

metallic 2D materials out of equilibrium [105]. Such an approach grants the possibility to study instabilities in the electronic system under extreme temperatures and on ultrafast time scales where transient charge order effects and metal-insulator transitions may completely alter the electronic spectrum around the Fermi energy, as has been already observed in bulk metallic TMDCs [106, 107, 108, 109, 110]. For the first time, these extreme conditions were probed by the author of this thesis on a subpicosecond time scale on a metallic 2D TMDC, namely 2D TaS_2 of the 2H polymorph, giving access to low energy excitation dynamics, thereby exploring density-dependent many-body effects, as it will be shown later in this chapter.

Several growth techniques have been developed for the synthesis of 2D metallic TMDCs [13]. In particular, a single layer of 2H-TaS_2 (1H-TaS_2) can be isolated from a bulk cristal by means of mechanical exfoliation [18]. A polymer pick up technique, for instance, can be used to obtain 1H-TaS_2 on a graphene substrate [86]. While exfoliation processes, like the polymer pick up technique, can supply a transferable layer to any substrate, high levels of undesired impurities can occur while transferring the sample [111]. On the contrary, MBE in a UHV environment typically leads to a relatively low level of impurities and favours the epitaxial growth of atomically thin layers, thanks to the typical low deposition rate, while providing large area growth and fine control over the doping level [112].

While the synthesis of the atomically thin isostructural and isoelectronic tantalum diselenides is well established [79, 113, 114], 2D tantalum sulphides films prepared by MBE are less studied because of the high sulphur vapour pressure required in UHV systems [115, 116, 113]. 1H-TaS_2 was already obtained on Au(111) metallic substrate by means of MBE [116]. Furthermore 1H-TaS_2 was grown as a quasi-freestanding monolayer on a graphene/iridium substrate [117, 118] and also on a graphene/6H-SiC(0001) substrate [114]. In the two latter instances, the growth has been carried out by sulphurization of Ta from elemental sulphur evaporated from a FeS Knudsen cell. CDW order close to a (3×3) periodicity is found on 1H-TaS_2 when the hybridization with substrate bands is absent, while CDW is found to be suppressed on Au(111) metallic substrate [116], due to the strong Au-S interactions [119].

In the current chapter it is shown how, for the first time, *in situ* MBE of Ta sulphurized at H_2S low pressures provides a viable way to grow 2D TaS_2 on graphene.

3.2 2D TaS_2 on graphene on SiC

The growth of 2D TaS_2 on graphene on a SiC substrate was carried out at in the preparation chamber PC2 at the SGM3 end station in order to be later transferred to ARTEMIS beamline in the UK for tr-ARPES measurements.

Bilayer (BL) graphene was grown on the Si face of 6H-SiC(0001) by means of the *face-to-face* method, which resulted in micrometer flat terraces [120]. The flat morphology of graphene on SiC provides an ideal platform to control the growth of 2D TaS_2.

A redox chemical reaction is involved in the formation of 2D TaS_2 where four electrons are donated from the metallic Ta(0) to two sulphur atoms coming from two molecules of H_2S. The elements, therefore, rearrange their oxidation states in Ta(+4) and S(-2), leading to the formation of two H_2 molecules. As a result, the occurrence of the sulphurization establishes a metal coordination complex TaS_2 [121]. A two-step growth process inspired by Refs. [116, 122, 123] was involved to create 2D TaS_2:

1. For the first step the sample was kept at room temperature while Ta was evaporated unto the sample during a 2-3 minutes deposition in a H_2S environment (between $p \sim 10^{-6}$ mbar and $p \approx 10^{-5}$ mbar).

2. In a second step, the sample was annealed at $T \approx 890$ K for 20 minutes at the same H_2S pressure, but with the noozle from which the H_2S gas was leaked at a distance of 1cm from the sample surface.

This two-step cycle was repeated until the desired amount of TaS_2 was reached.

The sketch in Fig. 3.2(a) represents the hypothetical reaction proceeding at the surface. It is speculated here that Ta (or TaS_x compounds) intercalates beneath the BL graphene, or between the two graphene layers, on the concave sites of the wavy Moiré superstructure attributed to the mismatch between the SiC and graphene lattice parameters [124], most likely during the temperature raise of the second growth step (step 2a in Fig. 3.2(a)). This speculation is based on the observation of a distorted 1D pattern with a periodicity of ≈ 0.4 nm in the vicinity of the irregularly shaped protrusions typically located at the concave sites. These periodical modulations in the LDOS are shown, for instance, within the area marked by the circle on the STM

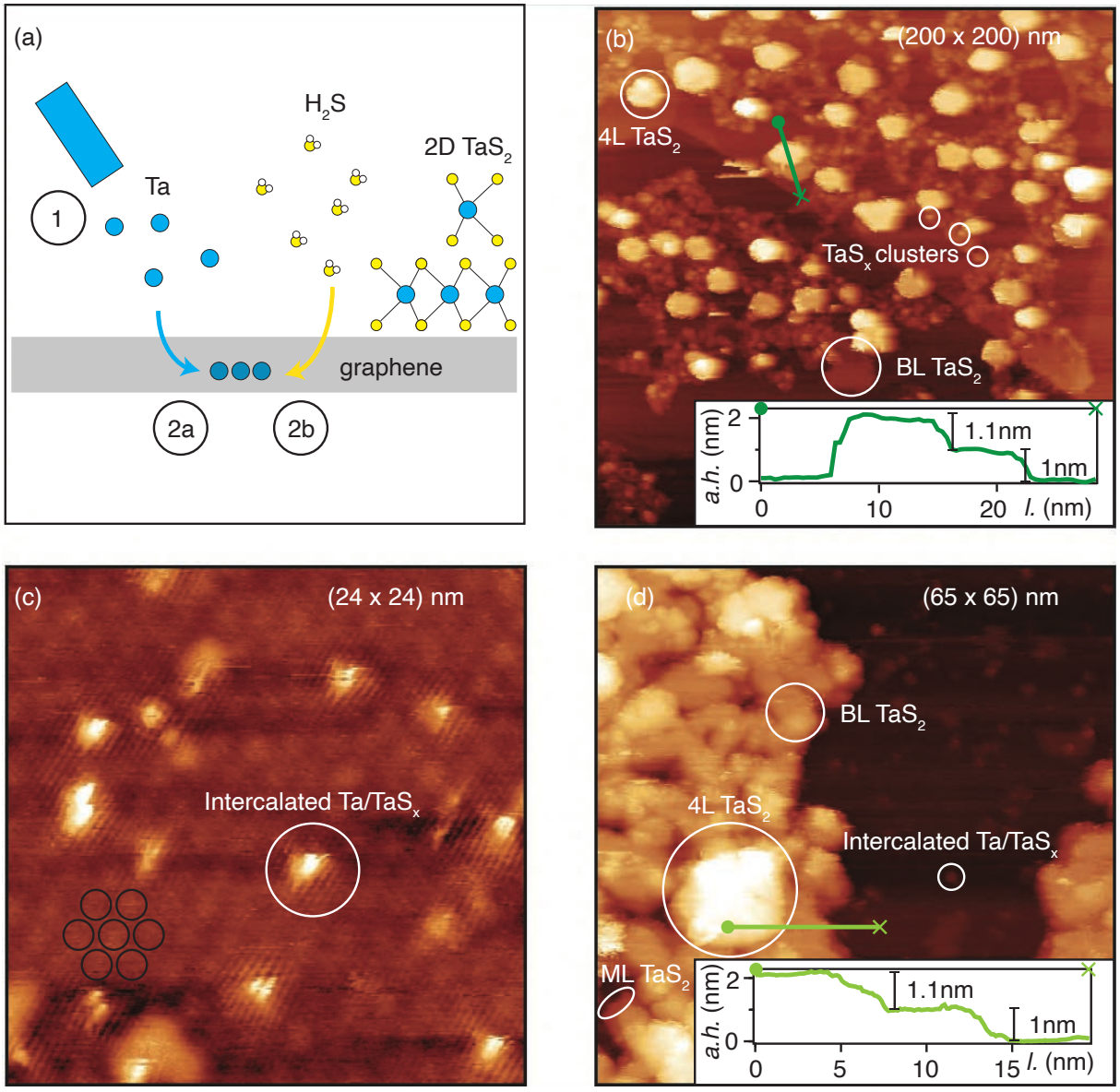

Figure 3.2: (a) Sketch of the reaction at the surface. Ta is evaporated from a Ta evaporator (step 1), intercalates under graphene (step 2a) and reacts with the H_2S gas to form TaS_2 on the graphene surface (step 2b). (b) STM topographic image ($V_b = 2$ V, $I_t = 80$ pA and color scale range of the apparent height $\Delta h = 4$ nm) of TaS_2 nano-islands on graphene obtained at high H_2S pressure ($p \approx 10^{-5}$ mbar) after 1 cycle. An apparent height, *a.h.*, profile is marked by the green arrow in the panel and shown in the inset. (c) STM ($V_b = 0.57$ V, $I_t = 750$ pA and $\Delta h = 0.4$ nm) of graphene on SiC with its typical Moiré structure (marked by black circles) obtained at low H_2S pressure ($p \approx 10^{-6}$ mbar) after 2 cycles. (d) STM ($V_b = 0.57$ V, $I_t = 520$ pA and $\Delta h = 3$ nm) obtained as in (c). The apparent height profile highlighted by the green arrow is shown in the inset.

image in Fig. 3.2(c) for a sample grown at low H_2S pressure ($p \approx 10^{-6}$ mbar). Previous STM based observation of $TaCl_5$ intercalated graphite showed the presence of similar long-periodic patterns belonging to a superstructure on a graphite basal plane, but with different periodicity (0.9 nm) [125]. Intercalation could possibly occur *via* the passage of Ta/TaS_x by defect formation in graphene only favoured at elevated temperatures, as it was observed for Mo [117] as well as for other metals [126, 127, 128]. Further investigations need to be carried out in order to assess the behaviour of Ta on graphene in H_2S atmosphere, thereby better defining the growth mechanism involved in the reaction at the surface.

When the sample is instead heated up at higher H_2S pressure ($p \approx 10^{-5}$ mbar), instead, no more intercalated Ta/TaS_x was observed by STM, however some new flat islands with a characteristic size of a few nm were observed already after one growth cycle following the reaction of intercalated TaS_x with the H_2S gas (step 2b in Fig. 3.2(a)). These irregular hexagonal or triangularly truncated islands shown in Fig. 3.2(b) are located on a topmost position and closely resemble previously recorded TaS_2 nanoislands on graphene, both in shape and typical size [114, 117, 118], while the structure just below the height of the TaS_2 islands shows a percolated network similar to the one observed for MoS_2 on graphene [117]. Despite the resemblance with earlier findings on ML TaS_2 islands, the apparent height, *a.h.*, profile in the insert in Fig. 3.2(b) of *a.h.* $\approx$ 1 nm per TaS_2 sheet seems to be almost double sized with respect to the formerly measured value of *a.h.* $\approx$ 0.5 to 0.65 nm for ML TaS_2 on graphene [118, 114], the latter being more in line with the theoretically estimated value *a.h.* $\approx$ 0.6 (i.e. half of the 2H unit cell) [129, 130, 131, 132]. The calibration of the STM apparent height was carried out at the step of 6H-SiC(0001) terrace edges; however calibration should rather have been accomplished on a different substrate, like on the reconstructed (7×7)-Si(111) surface [133] or Si(001) surface [134], as the step edges of 6H-SiC(0001) do not have an unequivocal height [135]. Therefore, on one hand it cannot be ruled out that the bottom and topmost sheets in Fig. 3.2(b) belong to a wrongly-calibrated and overestimated ML and BL, respectively; however, it is more likely that they actually correspond to a BL and a quadruple layer (4L), respectively, matching in this way the aforementioned apparent height measurements previously performed on ML TaS_2. The last interpretation would require the simultaneous formation of two layers of 1H-TaS_2 to be energetically more favourable than an atomic layer-by-layer growth scheme. In fact, it was observed by earlier studies that, when a lithium doped ML TaS_2 on graphene sample is heated to temperatures identical to the one performed in the current experiment, the morphology of

the TaS_2 completely changes resulting in a total absence of ML TaS_2 and in the solely presence of BL TaS_2 [118]. A careful inspection of the bottom TaS_2 sheet unveils the presence of two distinct layers within the sheet with a typical apparent height of $a.h. \approx 0.55$ ML, in line with the apparent height profiles measured by the previous studies [2]. A small portion of a ML is highlighted, for instance, at the bottom left corner of Fig. 3.2(d).

This peculiar growth mechanism is reminiscent of a Volmer-Weber growth where adatom-surface interactions are weaker than adatom-adatom interactions, causing the formation of three-dimensional adatom islands rather than ML uniform sheets [136]. In spite of the fact that 2D TMDCs typically grow through a different growth mechanisms [137], a similar growth mode to the one hypothesized here was found on 2D metallic $NiTe_2$ [138]. Nevertheless, in this case, the *vertical growth* typical of the Volmer-Weber mechanism would take place only up to the formation of a second layer. Thus, it is speculated here that a Volmer-Weber growth mechanism occurs until a BL is formed, and then the adatom-surface interactions take over allowing the BL sheet to laterally percolate on the surface networking with the other BL islands through a Frank-van der Merwe (layer-by-layer) mechanism. The reshaping of the islands most likely took place through island diffusion and aggregation (Smoluchowski ripening) rather than step edge diffusion generating the characteristic branched and elongated shapes readily visible in Fig. 3.2(b) as it was also observed for MoS_2 on graphene [117]. This non-ordered network could be the cause of the rotationally disoriented domains observed by ARPES in Sec. 3.3.

The overall overgrowth morphology in Fig. 3.2(b) resembles the one of MoS_2 on graphene [122, 117] rather than the one of previously grown TaS_2 on graphene [117, 114]. In fact, similarly to MoS_2, for high pressures ($p \approx 10^{-5}$ mbar) a second sheet nucleates on top the first one already at relatively low coverages. For example, the coverage related to the sample presented in Fig. 3.2(b) is estimated to be $\theta \approx 0.3$ ML and $\theta \approx 0.2$ BL by area analysis of different STM topographic images, while the previously recorded BL/ML ratio for TaS_2 on graphene was much lower [114]. In addition, features that lack well-defined structure are observed within the TaS_2 sheets in Fig. 3.2(b). These may possibly be constituted by unreacted tantalum, or bundles of

[2] The word *sheets*, indeed, is purposely used in relation to 2D structures with a non clarified number of layers each. For the same reason, the name *2D TaS_2* is adopted in this chapter, while *SL TaS_2* was used in the manuscript in Ref. [77], as back then we were not aware of the recent finding discussed in the current paragraph. Nevertheless, as it will be shown by the end of the chapter, this different understanding concerning the sample morphological structure is not believed to significantly affect the interpretation of the critical results of this work.

Ta_6S_6 nanowires similar to the Mo_6S_6 previously observed on graphene [122].

In order to decrease the BL/ML ratio and the number of defects at the surface the H_2S pressure was reduced to $p \approx 10^{-6}$ mbar, as shown for the sample in Fig. 3.2(c) and (d). In this case, as already anticipated, not all of the intercalated Ta/TaS_x reacted with H_2S, however a lower amount of impurities is found at the surface. Furthermore, a coverage of $\theta \approx 0.5$ ML and $\theta \approx 0.08$ BL is measured. Nonetheless, the percolated network perimeter takes a rather undefined shape under these growth conditions, hinting at the presence of multiple TaS_2 crystal orientations, as it will be confirmed in next Section.

While the STM data does not bring an unequivocal interpretation of the growth mechanism, which leaves room for future in-depth analysis, the electronic structure shown in the next section confirms the formation of 2D TaS_2 in the 2H polymorph.

3.3 Electronic structure of 2D TaS_2 on graphene

The BL graphene substrate and 2D TaS_2 electronic structures are inspected through static ARPES and core level spectroscopy along different steps of sample synthesis. Fig. 3.3(a) shows the ARPES spectrum around the $\overline{K}$ point of the BZ of the BL graphene. A split valence band and an occupied conduction band minimum are visible, as expected for high quality n-type BL graphene on 6H-SiC(0001) [139].

After a single growth cycle the photoemission signal arising from sub-monolayer TaS_2 appears in the static ARPES spectrum in Fig. 3.3(b) *via* the coexistence of BL graphene linear band structure around $\overline{K}$ point and Ta $5d_{z^2}$ conduction band structure of TaS_2 along the $\overline{\Gamma} - \overline{K}$ direction of graphene. The higher background and the well-defined Fermi edge away from the dispersive bands are attributed to the presence of defects and non-fully sulfurized TaS_x clusters shown in Sec. 3.2. The Ta 4f core level region presented in the core level spectrum in Fig. 3.3(c) shows characteristic spin-split $4f_{7/2}$ and $4f_{5/2}$ peaks for TaS_2 of the H-polytype. The highly asymmetric peaks with shoulders on the high binding energy sides are caused by many-body interactions with the core hole and charge transfer processes involving the Ta $5d_{z^2}$ conduction band states of 2H-TaS_2 near the Fermi level shown in Fig. 3.3(b) [140].

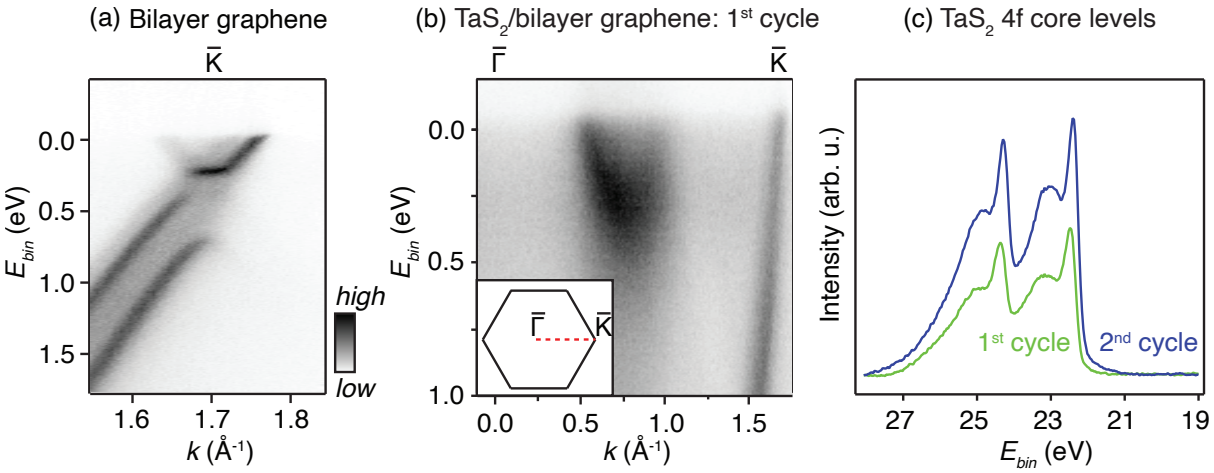

Figure 3.3: (a) Static ARPES spectra of BL graphene on 6H-SiC(0001) and (b) of 2D TaS_2 after a single growth cycle. The dashed line in the insert in (b) shows the $\overline{\Gamma} - \overline{K}$ direction of the BL graphene BZ along which the spectra were collected. (c) Core level spectra of the Ta 4f core level region of 2D TaS_2 after one (green) and two (blue) growth cycles.

Fig. 3.3(c) also shows that a higher TaS_2 coverage is obtained by additional growth cycles. This is verified by an increase in 4f core level intensity as well as a decrease in photoemission intensity from the bands of the underlying BL graphene in the photoemission spectrum (not shown). The sample used for tr-ARPES measurements, whose results are presented in the following part of the Chapter, was prepared by stopping the growth after two TaS_2 growth cycles at H_2S pressure of $p \approx 10^{-6}$ mbar, like the sample presented in Fig. 3.2(c) and (d), to ensure sufficiently high coverage and avoid as much as possible the presence of multilayer domains.

3.4 Electronic structure dynamics of 2D TaS_2

The undoped ML TaS_2 band structure, shown in Fig. 3.4(a), is characterized by a half-filled band with a Fermi surface consisting of hole pockets around the $\overline{\Gamma}$ and $\overline{K}$ points of the 2D Brillouin zone (BZ) [116]. The arrows in Fig. 3.4(a) show the direct optical transitions involving occupied valence band and unoccupied conduction band states that generate excited carriers. The thermalization of these excited carriers takes place via electron-electron scattering processes at a timescale shorter than the experimental temporal resolution, thus only a continuous distribution of hot electrons is experimentally accessible.

Fig. 3.4(b) shows a tr-ARPES spectrum taken near $\overline{\Gamma}$ without optical pumping. The dis-

persive feature with a highest binding energy of ≈400 meV at ≈0.8 $Å^{-1}$ is the electron-pocket between the two hole pockets mentioned above, which crosses the Fermi level at ≈0.5 $Å^{-1}$ and is unoccupied at $\overline{\Gamma}$. No high-symmetry direction in the calculated band structure of Fig. 3.4(a) can be assigned to this observed dispersion in view of the azimuthal disorder between different domains of 2D TaS_2 on the sample. The measurement direction has to be interpreted as an average over all possible orientations, roughly corresponding to an average over the $\overline{\Gamma} - \overline{M}$ and $\overline{\Gamma} - \overline{K}$ directions marked in Fig. 3.4(a) [116]. What differs between these directions is the higher maximum binding energy reached by the double degenerate band along $\overline{\Gamma} - \overline{M}$ with respect to the strong spin-orbit split band along $\overline{\Gamma} - \overline{K}$. Nevertheless, if one considers only small values of $|k|$, the hole pocket character is granted by the dispersion in the two directions being sufficiently similar for the average. Therefore, given the considerations above, a broadening of the features at higher binding energies is visible in the data and is due to integration over all directions in the BZ. The spin-orbit splitting along the $\overline{\Gamma} - \overline{K}$ direction has no direct consequence for the observed band, since the upper spin-split branch is above the Fermi energy. Furthermore, the possible presence of a second or multiple layers could also contribute to the observed broadening along $\overline{\Gamma} - \overline{M}$ by lifting the degeneracy and moving the maximum binding energy to slightly lower values with respect to a scenario with a simple ML involved. In fact, although no calculation has been performed for BL TaS_2, it is reasonable to expect that it resembles the one related to the bulk rather than that of ML, as the unit cell of BL and bulk in the 2H-polymorph are exactly the same. It was shown that the bulk electronic structure [117] is characterized, indeed, by a spin-split state along $\overline{\Gamma} - \overline{M}$; however a state distinct from the spin-split should also appear at $\overline{\Gamma}$ at relatively low E_{bin}, which is not seen in 3.3(b). This would be in contrast with the hypothesis of dominant presence of BL at the surface presented in Sec. 3.2, rather pointing to the presence of ML. In any case, both the ML and BL hypothesis will be considered in the discussion on the relevant results thereon.

The result of optically pumping the system with a photon energy of 2.05 eV, at a fluence of $F = 7.8$ mJ/cm^2 and at a time delay of 40 fs between the pump and the probe pulse (peak excitation of the system) is shown in Fig. 3.4(c). Drastic changes in the spectrum are ascertained: the observed dispersion now broadens well above the Fermi energy, indicating the presence of hot electrons. A way to visualize this more clearly is by considering the difference between the excited spectrum and the equilibrium spectrum in Fig. 3.4(d). Here an excess in photoemitted intensity (red) indicates those states occupied by excited electrons while the depletion (blue)

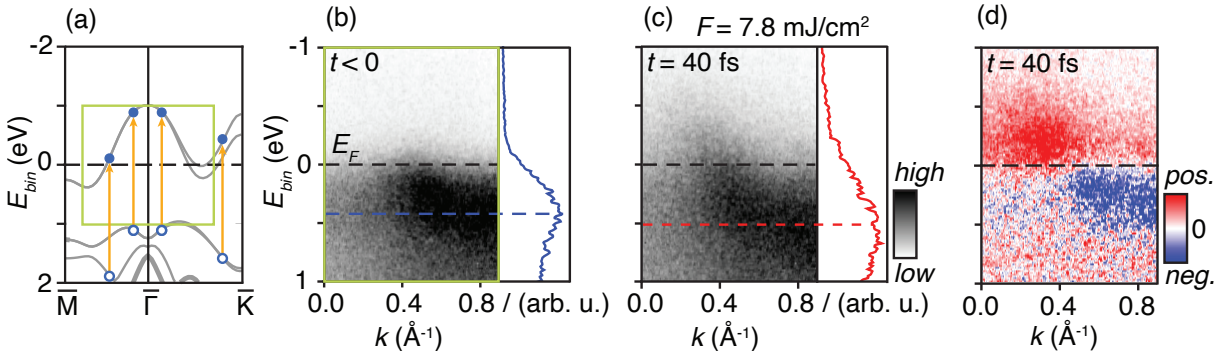

Figure 3.4: (a) DFT Calculated dispersion from Ref. [116] with instances of possible direct electron (filled circles) and hole (open circles) transitions (arrows). The region enclosed by a green square labels the (E,k)-space probed in the tr-ARPES experiment thereon. (b) Left: Measured tr-ARPES spectrum of the 2D TaS_2 dispersion around E_F: before optical excitation ($t < 0$), at sample temperature of 300 K. Right: Energy distribution curve taken at $k_{min} = 0.81$ Å^{-1} corresponding to the band's highest binding energy. An estimate of the peak position is given by the dashed blue line. (c) tr-ARPES data as in (b) but at the peak of optical excitation ($t = 40$ fs). Right: Energy distribution curve taken as in (b). (d) Difference spectrum: intensity difference obtained by subtracting the intensity for $t < 0$ in (b) from that at $t = 40$ fs in (c).

denotes states occupied by excited holes. It is evident from Fig. 3.4(d) that a majority of excited hot electrons lie above the Fermi energy.

Unexpectedly, the shift between the maxima of the energy distribution curves (EDCs) in Fig. 3.4(b) and (c) suggest that whereas the position of the Fermi edge remains constant, the entire dispersion is shifted to higher binding energies by $\gtrsim$100 meV. Shifts of the band structure to higher binding energy upon excitation is not expected for metallic systems. Naively, one might think that space charge and surface photovoltage effect could be the cause of the measured shifts of the spectrum [141, 142, 70]. Despite the fact that the latter mainly found to affect the tr-ARPES results on much longer time scales than relevant here [141], both effects lead to a rigid shift of the entire spectrum in energy, including the position of the Fermi energy. As it will be shown in more detail in the data analysis below, this is not the case for the data reported here.

The presence of a broad artificial linewidth at the band's highest binding energy challenges the conventional analysis of both energy and k-dependent photoemission intensity of the band. Furthermore, the relatively small bandwidth complicates the disentanglement of the time-

dependent Fermi-Dirac carrier distribution and the band shift in question. In the following Section a viable approach to keep track of the relevant changes in the electronic structure is presented.

3.5 Fit of a simulated model spectral function to $\mathcal{I}(E,\mathbf{k})$

An accurate determination of the band structure changes at different sample temperatures and pump fluences requires quantitative analysis of the observed effects. The complexity of the situation explained above and the many unknown parameters render the conventional approach of fitting energy or momentum distribution curves by simple models impractical. It was demonstrated that, extracting the electronic temperature from such fits can be already problematic even for very simple situations [143, 144, 145]. Instead, a novel approach is introduced here. The single particle dispersion, many-body effects and the electronic temperature can be extrapolated in a single fit from the energy and $k-$dependent photoemission intensity, such as in Fig. 3.5(a), by fitting it to a model based on a resolution-broadened spectral function.

The photoemission intensity measured in an ideal ARPES experiment $\mathcal{I}(E,\mathbf{k})$ was given in Eq. (2.12). The energy- and $k-$dependent matrix element $\mathcal{M}_{if}^{\mathbf{k}}$ is expected to vary only weakly since, in the present case, the data are only collected for a small range of energy and k and for a fixed photon energy and polarization.

The azimuthally averaged photoemission intensity from 2D TaS_2 is phenomenologically modelled as:

$$\begin{aligned}\mathcal{I}(E,k) = (\mathcal{O}+\mathcal{P}E+\mathcal{Q}k)\,\frac{\pi^{-1}\left(\alpha+\beta E+\gamma E^2\right)}{(E-(ak^2+bk+c))^2+(\alpha+\beta E+\gamma E^2)^2}\,(e^{E/k_BT_{el}}+1)^{-1}\\ +\left[(a_b+b_bE)+A_d\frac{\pi^{-1}w_d}{(E-\epsilon_d)^2+w_d^2}\right](e^{(E-\zeta)/k_BT_{el}}+1)^{-1},\end{aligned} \tag{3.1}$$

where the actual measured intensity is modelled by a convolution of $\mathcal{I}(E,\mathbf{k})$ with the appropriate energy and momentum resolution functions $G(\Delta E)$ and $G(\Delta k)$, assumed to be Gaussian. All energies, E in Eq. (3.1), are references to the experimentally determined Fermi energy in the spectrum that is taken as the zero-level reference in this first part of the Chapter. An empirical linear dependence on E and k that could arise from, e.g., small matrix element variations, is taken into account by the three parameters $\mathcal{O},\mathcal{P},\mathcal{Q}$ in the first factor of the term. These param-

eters are set to match the calculated photoemission intensity to the experimental results. The second factor in the first term represents the spectral function in which the single particle is considered as a parabolic dispersion, $ak^2 + bk + c$, where its minimum position is constrained at $k_{min} = b/2a = 0.81$ Å^{-1}, as determined from a high-resolution ARPES spectrum in like in Fig. 3.3(b). The complex electronic self-energy appearing in the spectral function is comprised of a real part ϱ re-normalizing the dispersion and a imaginary part Γ broadening the features, as explained in Sec. 2.1.3. Here it is empirically assumed that the real part is zero and that $\Gamma = \alpha + \beta E + \gamma E^2$. This will always result in an increased broadening at higher energies that accounts for the azimuthal averaging over the somewhat anisotropic band structure. Care should thus be taken, to assign physical significance to ϱ and Γ. In the current experiment these quantities are phenomenologically fitted to the experimentally determined electronic structure at the expense of their original physical meaning, as it will be clarified later. In the third factor of Eq. (3.1) the Fermi-Dirac distribution, with T_{el} referring to the electronic temperature in the 2D TaS_2, dictates the population of the states at any time delay. In addition to the description of the 2D TaS_2 spectral function, it is necessary to account for the background intensity, which is expressed in the second term of the equation. The background intensity was empirically determined to have a linear energy dependence characterized by a offset a_b and slope b_b plus a non-dispersive defect level, which was observed in the experiment at energy $\epsilon_d = 0.31$ eV with constant amplitude A_d and width w_d. The background and defect features are both connected to a Fermi-Dirac function with a different cut-off ζ, which proves necessary to capture the re-distribution of background intensity at any time delay in the excited state.

All parameters in Eq. (3.1) are determined in a first instance using the high-resolution static ARPES data taken at ASTRID2 at a photon energy of 25 eV, i.e. the same photon energy as used for the probe pulse in the tr-ARPES experiment. For example, as the sample temperature is known, it can be fixed in the optimization process. The result of the fit is the one presented in Fig. 3.5.The excellent agreement between the measured photoemission intensity in (Fig. 3.5(a)) and the modelled intensity in (Fig. 3.5(b)) is further illustrated by the EDC-cuts extrapolated at the Fermi level crossing (k_F) and at the band minimum (k_{min}) in Fig. 3.5(c) and (d), respectively. The highest binding energy, in this fit, reaches a value of 350 meV. The light gray lines of these cuts represent the $(a_b + b_b E)$ component of the background (BG) function in the second term of Eq. (3.1).

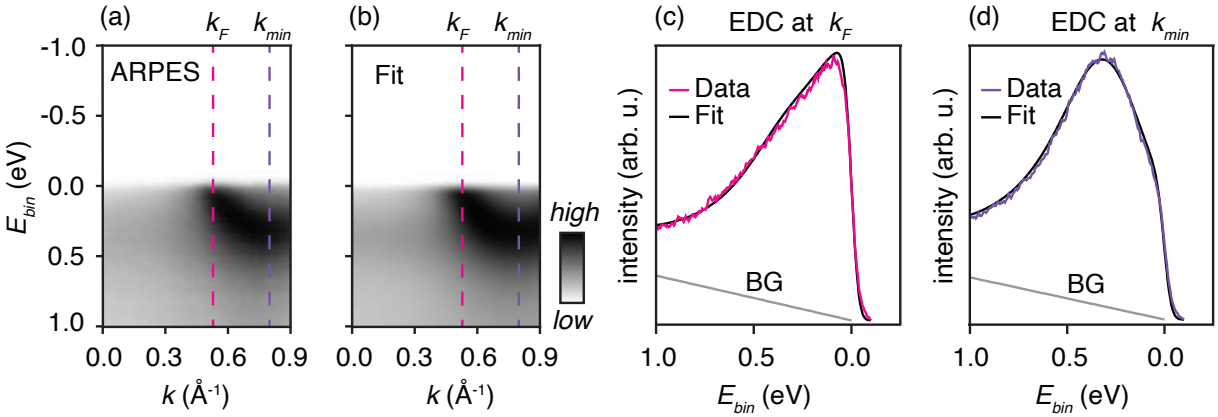

Figure 3.5: (a) Static ARPES spectrum of the 2D TaS_2 parabolic state with the Fermi level crossing at k_F and the band minimum located at k_{min}. (b) Modelled intensity according to Eq. (3.1) over the measured region of (E, k)-space shown in (a). (c) and (d) Example EDCs of the measured data and intensity fit taken along the dashed vertical lines shown in (a) and (b) at (c) k_F in pink and (d) k_{min} in purple, respectively. The light gray line marked "BG" represents the background intensity in the fit.

After the fit performed in Fig. 3.5, the parameters extrapolated from the fit of static ARPES are carried over to the tr-ARPES spectra acquired in equilibrium conditions ($t < 0$) where the background and defect intensity-related parameters are allowed to be adjusted together with the energy resolution ΔE to account for the different beamline and detector properties that limit the energy resolution. Note that ΔE has to be fitted for $t < 0$ where $T_e = T_{sample}$ is momentarily fixed, with T_{sample} being the measured sample temperature. This allows to decouple the broadening generated by the experimental resolution to the one caused by T_{el}. Once these parameters have been determined, α, β, c, T_{el} and ζ are allowed to vary for all time delays, while the position of the observed Fermi energy E_F', i.e. the energy zero of Eq. (3.1), was kept constant.

In this way α and β are let free to accommodate an observed increase in linewidth which, as pointed out before, has no physical relation to the imaginary part of the self-energy. ζ takes into account the redistribution of the excited state of the background intensity, which does not necessarily behave in the same way as the excited state of the metallic state. Finally, c and T_{el} are tracking the behaviour of 2D TaS_2 band shift and the change of electronic temperature, respectively, on the probed ultrafast time scale. This approach leads to an excellent agreement between fit and data for different settings of the laser fluence and sample temperature. For example, Fig. 3.6 shows representative results for the application of this fitting method to three

different time-resolved data sets measured at a certain fluence and sample temperature.

Fig. 3.6(a)–(c) in panel (II) show the measured dispersion at equilibrium, at maximum excitation ($t = 40$ fs) and at a later time delay $t = 350$ fs, while (f)–(h) in the same panel show the relative modelled photoemission intensities, obtained as described above. The redistribution of background intensity following photoexcitation is also taken into account from Eq. (3.1). The excellent description of the data is illustrated in the comparison between measured ((d) and (e)) and fitted ((i) and (j)) intensity differences for time delays of 40 fs and 350 fs and also in the direct comparison between measured and fitted EDC-cuts at k_F and k_{min}, as shown in (k) and (l). Fits of similar quality are obtained for data sets taken at different sample temperatures and pump laser fluences in panel (I) and (III).

The extracted dynamic changes of the dispersion in terms of band shift and electronic temperature T_{el} from data in Fig. 3.6 panel (II) are given in Fig. 4.1 in the next chapter. The similar behaviour in the extracted dynamic changes of the band shift and T_{el} indicates that these two parameters are correlated. This correlation will be matter of discussion in the next section.

3.6 Electronic temperature-dependent band shifts

In order to quantify the band shift, the parameter ΔW is introduced, defined as the difference between the band minimum energy in the excited and equilibrium state, that is the change of the parameter c in Eq. (3.1).

Figure 3.6 ***(facing page)*****:** Time dependence of the excited-state signal in 2D TaS_2 and spectral function simulations. (II): (a)–(c) tr-ARPES data obtained at the given time delays for an optical excitation energy of 2.05 eV and a pump laser fluence of 7.8 mJ/cm^2 with $T_{sample} = 300$ K. The spectrum in (a) was taken before optical excitation. The fitted parabolic dispersions derived according to Eq. (3.1) are shown on top of the spectra and coloured to distinguish the different time delays. (d) and (e) Difference spectra determined by subtracting the equilibrium spectrum in (a) from the excited state spectra in (b) and (c). (f)–(j) Simulated intensity (difference) corresponding to the measured data in (a)–(e). (k),(l) Comparison of EDCs from measurements (symbols) and simulations (lines) at k_F and k_{min}, respectively (see pink and purple lines in (f)). Panels (I) ($F = 4.4$ mJ/cm^2, $T_{sample} = 103$ K) and (III) ($F = 8.4$ mJ/cm^2, $T_{sample} = 73$ K) are plotted in an identical manner to panel (II) to facilitate a direct comparison.

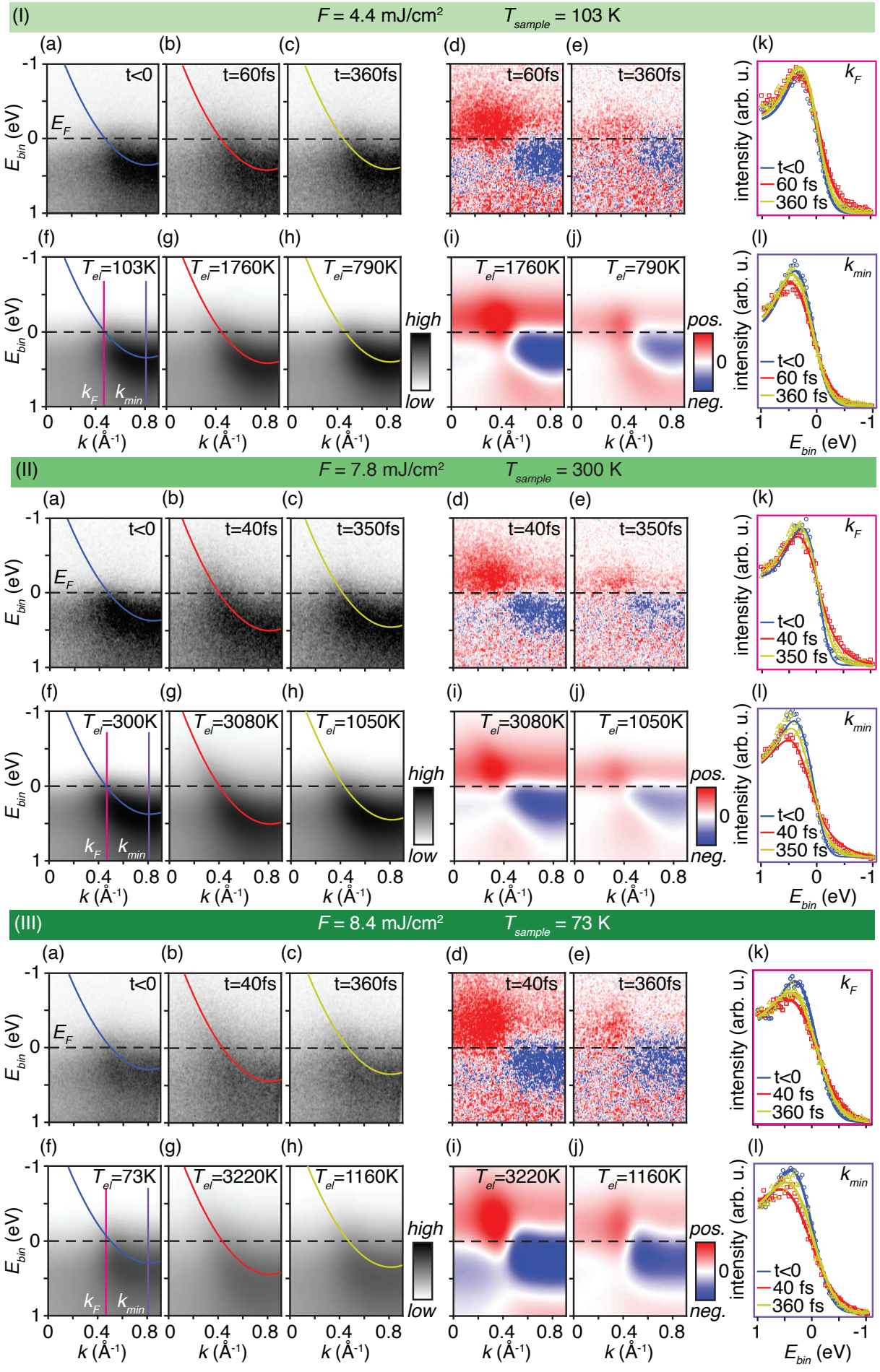
(I) F = 4.4 mJ/cm² T_sample = 103 K
(II) F = 7.8 mJ/cm² T_sample = 300 K
(III) F = 8.4 mJ/cm² T_sample = 73 K
(a) (b) (c) (d) (e) (k)
(f) (g) (h) (i) (j) (l)
t<0
t=60fs
t=360fs
t=40fs
t=350fs
E_F
E_bin (eV)
k (Å⁻¹)
T_el=103K
T_el=1760K
T_el=790K
T_el=300K
T_el=3080K
T_el=1050K
T_el=73K
T_el=3220K
T_el=1160K
k_F
k_min
high
low
pos.
neg.
0
intensity (arb. u.)
t<0
60 fs
360 fs
40 fs
350 fs

Note that the quantity ΔW is not related to the rigid shift of the entire photoemission spectrum caused by the space charge and surface photovoltage effects introduced in Sec. 2.1.3 as it does not entail a shift of the whole photoemission intensity. Nevertheless, an increasing rigid shift of the whole photoemission intensity towards lower binding energies was observed. This effect sets in after several picoseconds, with a maximum shift of up to 200 meV. The effect is likely caused by space charge effect resulting from the pump-induced high electron density that affected the kinetic energy of the emitted photoelectrons as they propagated to the electron analyzer, as evidenced by the fact that it shows an inversely proportional dependence on T_{sample} and a direct proportionality with F. However, it is not possible to exclude *a priori* that surface photovoltage effects of the SiC substrate were also involved [146, 70] even though they typically take place on a longer nanosecond time scale [147, 141]. In this case the surface photovoltage effects could be present as a constant shift within the delay time interval investigated in this study. In any case, due to the similar magnitude of the space charge induced shift and ΔW and because of the large relative uncertainty of ΔW on a picosecond scale, it became hard to distinguish the change of the parameter c in Eq. (3.1) from the shift related to the space charge effects after a few picoseconds after excitation. Therefore the snapshots of the photoemitted intensity above 5 ps where the shift occurs have been omitted. In any case, being the relaxation process very fast, the TaS_2 state near the Fermi level has nearly reached a quasi-equilibrium state and ΔW is approximately zero for these time delays. The carrier dynamics at these later phase of the relaxation process will be further investigated in Chap. 4.

Note that no boundary condition of a fixed k_F value has to be set when the fit is constrained to a rigid band shift, therefore no changes of the carrier effective mass were recorded. This fitting procedure was chosen because the broad Fermi-Dirac distribution was not affecting the spectral region of the band maximum in binding energy, making the position of the band an experimentally well-accessible quantity. Moreover, it is observed that the change in k_F resulting from a rigid shift of the dispersion is relatively small (< 0.05 Å^{-1}). This would be much harder to resolve than the energy shift because of the broad Fermi-Dirac distribution. Nevertheless, minor changes in the dispersion and of the Fermi wave vector cannot be completely excluded, even though the assumption of a merely a rigid shift of the band appears justified because of the resulting high fit quality at all time delays.

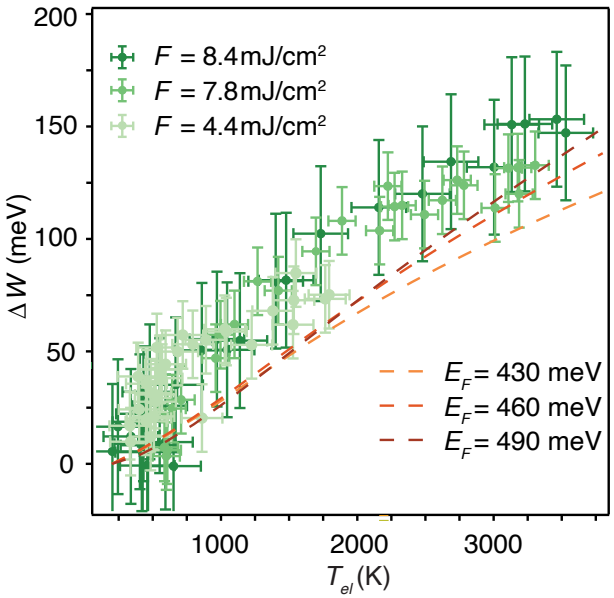

Figure 3.7: Temperature-induced band shift, using data for different choices of T_{sample} and F. The data points ΔW as a function of T_{el}. The curves are obtained from the calculated change in the occupied bandwidth as a function of T_{el} for three hypothetical different values of the Fermi energy of the system (chemical potential at $T_{el} = 0$.)

In Fig. 3.7 the data points obtained at different fluences and sample temperatures from Fig. 3.6 are plotted in terms of the respective ΔW as a function of T_{el} uncovering a strong correlation between ΔW and T_{el}.

In the present section, causality between the band shift and a temperature-induced shift of the chemical potential, which is required to conserve the total charge in the system, will be explored. The possibility of additional shifts caused by the temperature-dependence of the electronic screening is also addressed here.

Under typical experimental conditions, $k_B T$ is much smaller than the Fermi energy, meaning that changes of the chemical potential are small compared to the zero-temperature Fermi energy in a metallic system. This is clearly not the case here. Indeed, the width of the Fermi-Dirac function at T_{el} such as 3000 K quantifies the occupied bandwidth of 2D TaS_2, and temperature-induced shift of the chemical potential should thus be taken into consideration.

In the last part of this Chapter, the absolute BZ band minimum, $E_{k_\circ}$, will be redefined as the zero of the energy scale, therefore the temperature-dependent occupied bandwidth measured

in the experiment is now conceived as

$$W(T_{el}) = \mu(T_{el}) - \Sigma_\circ(T_{el}), \tag{3.2}$$

where $\Sigma_\circ(T_{el})$ is the real part of the self-energy at the band minimum position, $k_\circ$, and, as the number of charges needs to be conserved in the system, the chemical potential, μ, is determined by the assumption of a fixed number of electrons, N, at any temperature [3].

$W(T_{el})$ thus has two contributions, the first one, μ, arising from the temperature-dependent chemical potential and the second one from the electron-electron interaction that affects the energy of the band minimum via the self-energy, $\Sigma_\circ(T_{el})$. When the system is heated from the equilibrium temperature, T_{eq}, to T_{el}, the temperature-induced change of the bandwidth reads

$$\Delta W(T_{el}) = W(T_{el}) - W(T_{eq}) = \Delta\mu(T_{el}) - \Delta\Sigma_\circ(T_{el}) \tag{3.4}$$

where $\Delta\mu(T_{el}) = \mu(T_{el}) - \mu(T_{eq}) \approx \mu(T_{el}) - E_\mathrm{F}$ and $\Delta\Sigma_\circ(T_{el}) = \Sigma_\circ(T_{el}) - \Sigma_\circ(T_{eq})$. $\Delta\mu(T_{el})$ here is also affected by self-energy effects (if present), since the consequent rigid shift of the entire band is compensated by a change in the chemical potential as will be discussed later.

In Fig. 3.8(a), the resulting shift of the chemical potential is plotted as a function of electron filling in the layer, in this case expressed in terms of the Fermi energy. Note that the Fermi energy (i.e. the chemical potential at zero temperature) has now a different meaning with respect to the one assigned in the first part of the Chapter as, according to Eq. (3.4), now it is positioned according to the assumed filling of the band. In fact, the definition of E_F, strongly impacts the degree of changes in $\mu(T_{el})$. As seen in Fig. 3.8(a), if the band is assumed to have a very low filling (E_F roughly below 0.3 eV), the temperature increase will lead to a decrease of the chemical potential, the other way round for high filling (E_F roughly above 0.3 eV).

The most appropriate value of E_F should be chosen considering that the band minimum determined from the static high-resolution ARPES experiment at k_{min} in Fig. 3.5 is 350 meV.

[3]

$$N = \int_{-\infty}^{\infty} \frac{\rho(E)}{e^{\beta(E-\mu)}+1} dE, \tag{3.3}$$

where $\beta = 1/k_\mathrm{B}T_{el}$ and $\rho(E)$ is the energy dependent density of states

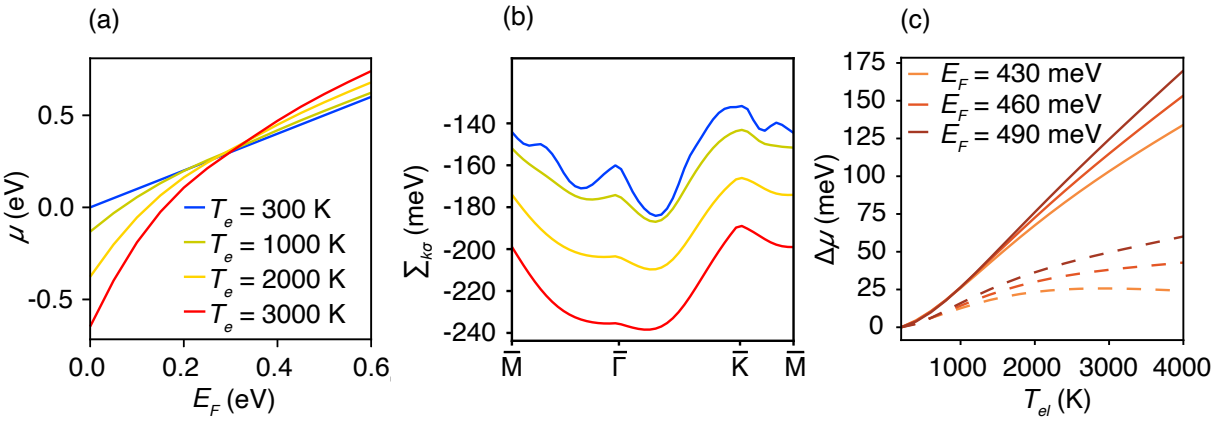

Figure 3.8: (a) Chemical potential as a function of the Fermi energy at different values of T_{el} with a given linewidth of $\Gamma_{\mathbf{k}\sigma} = 10$ meV and $\Sigma_{\mathbf{k}\sigma} = 0$. (b) Real part of the electronic self-energy plotted along high-symmetry lines of the BZ for $E_{\mathrm{F}} = 430$ meV (T_{el} as in (a)). (c) Chemical potential shift as a function of T_{el} for three different values of the Fermi energy. Solid (dashed) curves are related to the absence (presence) of self-energy effects on the chemical potential.

However, if the azimuthal disorder is taken into account, this value does not represent the Fermi energy, but roughly the highest binding energy obtained from the spectral average between the $\overline{\Gamma} - \overline{M}$ and $\overline{\Gamma} - \overline{K}$ directions. In reality, the actual Fermi energy corresponds to the highest binding energy spotted along $\overline{\Gamma} - \overline{M}$, which, according to the DFT calculated band structure for a ML TaS_2, is found to be ≈80 meV higher than the average highest binding energy of 350 meV. Even though the DFT calculated band structure was not evaluated for a higher number of TaS_2 layers, the highest binding energy along $\overline{\Gamma} - \overline{M}$ is expected to be found even at higher values with respect to the average highest binding energy, as the band Ta $5d_{z^2}$ is believed to spin-split for a higher number of layers, removing the degeneracy and increasing the overall bandwidth. Therefore, three different values of the Fermi energy ($E_F = 430$ meV, $E_F = 460$ meV and $E_F = 490$ meV) are arbitrarily chosen to provide a good estimate of the Fermi energy from the experimental data.

The temperature-induced shift in the chemical potential is plotted as solid line in Fig. 3.8(c) as a function of T_{el} for three different values of the Fermi energy. The effect of a temperature-induced chemical potential shift cannot be neglected in order to possibly explain the observed band shift ΔW due to the extreme temperatures reached and the small bandwidth.

Moreover, a relevant contribution from the self-energy correction is also expected as soon as

the strongly temperature-dependent screening of the Coulomb interaction is taken into consideration. For instance, it is well-known that the electronic self-energy has a significant impact on the measured dispersion of electronic states in static ARPES, even for simple metals [148, 149] and even more so when temperature-induced change in electronic screening could be generated by the large T_{el} range probed in the present experiment.

In fact, as T_{el} is very high under such experimental conditions, the Fermi-Dirac distribution function experiences a considerable broadening which becomes similar to the entire bandwidth (i.e. $k_B T_{el} \approx E_F$). The probability of virtual transitions, $E_{\mathbf{k}\sigma} \rightarrow E_{\mathbf{k}+\mathbf{q}\sigma}$ (where $\sigma = \pm$ labels a particular spin-split branch), are reduced by this strong broadening for all values of $\mathbf{q}$ in the BZ. The semi-Pauli-blocking effect that is generated by such broadening diminishes the number of virtual electron-hole excitations, leading to a weaker screening effect.

The temperature-dependent screening effect is taken into account by the static screened exchange self-energy $\Sigma_{\mathbf{k}\sigma} = \mathrm{Re}[\Sigma(E, \mathbf{k}, \sigma)]_{E \rightarrow E_{\mathbf{k}\sigma} - \mu}$, which is the real part of the self-energy correction for a particular spin-split branch within the whole BZ [116] and is given by [101]:

$$\Sigma_{\mathbf{k}\sigma}(T_{el}) = -\frac{1}{L^2} \sum_{\mathbf{q} \in \mathrm{BZ}} \frac{v_{\mathbf{q}-\mathbf{k}}}{1 - v_{\mathbf{q}-\mathbf{k}} \chi(\mathbf{q} - \mathbf{k}, T_{el})} f(E_{\mathbf{q}\sigma}, T_{el}), \tag{3.5}$$

where L is the sample side length, $\chi(\mathbf{q} - \mathbf{k}, T_{el})$ is the density-density susceptibility defined in Ref. [101], $v_{\mathbf{q}} = 2\pi e^2/(\epsilon_{\mathrm{eff}}|\mathbf{q}|)$ is the bare Coulomb interaction in 2D with $\epsilon_{\mathrm{eff}} \approx (1 + \epsilon_{\mathrm{sub}})/2$. Note that ϵ_{eff} is the effective dielectric constant and $\epsilon_{\mathrm{sub}} \approx 22$ is the dielectric constant of the graphene/SiC substrate [150]. Note that the Coulumb interaction is believed to be well approximated as 2D even for a BL TaS_2.

A weaker screening of the Coulomb interaction (lower value of $\chi(\mathbf{q}, T_{el})$) at high electronic temperature entails a stronger many-body effect. As anticipated, the explicit self-energy calculation points toward a very strong temperature dependence, with changes of ≈100 meV over the experimental temperature range, as depicted in Fig. 3.8(b).

Despite the strong $\mathbf{k}$ dependence of $\Sigma_{\mathbf{k}\sigma}$, the change of self-energy with temperature is mainly characterized by a rigid shift of the whole band which must be compensated by an opposite shift of the chemical potential in order to conserve the particle number. Thus, as

many-body effects are included in the calculation of the chemical potential, the newly calculated chemical potential shifts (dashed lines) in Fig. 3.8(c) experience a large difference with the chemical potential shifts without self-energy corrections (solid lines). Neither the change in the chemical potential nor the one the self-energy is directly experimentally accessible, but only their combination in ΔW according to Eq. (3.4). Fig. 3.7 finally compares the experimental data to the theoretical results obtained from Eq. (3.4) for the three different values of E_F, showing a qualitative agreement between experiment and calculation. By a comparison between the theoretical results in Fig. 3.7 and 3.8(c), it is possible to deduce that including static screening to a first order leads to a bandwidth change of merely $\approx$ 15 meV at $T_{el} \approx 4000$ K [4]. However, based on the considerations formulated above, a hypothetical presence of multilayer TaS_2 would imply a higher value of E_F, thereby showing a better quantitative agreement with the data.

In conclusion, in this chapter it has been shown that optical pumping leads to significant changes in the occupied bandwidth of the 2D metallic TaS_2 and strong variation of heating of the electron gas. The data were analysed quantitatively by means of a 2D fitting scheme describing the entire resolution-broadened photoemission intensity. The extrapolated band shifts are theoretically explained by taking into account the chemical potential shift required to conserve charge neutrality in the presence of a hot electron population as well as the temperature-dependent many-body screening effect. It is speculated that a higher number of layers is taken into consideration the theoretical description moves toward a better quantitative agreement with the data, confirming the hypothesized presence of multilayer domains of TaS_2.

In the next Chapter, the carriers relaxation will be addresses taking into account the role of the lattice in the dissipation of the energy measured by the subpicosecond decrease of the electronic temperature. This will bring intriguing considerations concerning the nature of electron-phonon interactions in this material.

[4] Note that the experimentally observed highest binding energy of the band does not coincide with the occupied bandwidth, whereas the *change* in its binding energy is identical to the theoretically calculated ΔW

Chapter 4

Hot carrier relaxation in 2D TaS_2

This chapter aims to extend the analysis of the results in Chap. 3 by considering the dynamics behind the ultrafast relaxation of the carrier density in 2D TaS_2. It will be shown how the transient state of the electron distribution can drive a temperature change of the phonons mediated by electron-phonon interactions.

The results presented in this Chapter are derived from the analysis introduced in Chap. 3 following the pubblication in Ref. [77]. However, the analysis shown in this Chapter was described neither in Ref. [77] nor elsewhere and is set forth here for the first time. These results are planned to be finalized in a manuscript and submitted to a relevant scientific journal after some final theoretical contributions will be developed by co-workers. The data analysis presented in this Chapter was mainly carried out by myself, with the contribution of Paulina Majchrzak, Jill Miwa and Søren Ulstrup.

4.1 Tracking the electron-phonon interaction on a ultrafast scale

While in Chap. 3 the electron-electron interactions played a major role in understanding the temperature-dependent many-body screening effects, the focus of this Chapter will be shifted to electron-phonon interactions.

Nuclei and electrons constitute two fundamental building blocks of all the visible material universe, thus the study of the interaction between these two is ever-present in condensed matter physics [151]. For example, electron-phonon interactions are at the heart of fundamental physical properties of metals such as resistivity [52, 152, 153] or phonon-mediated supercon-

ductivity [154, 155]. In particular, the conduction electrons can screen the ionic vibrations [156], leading in some cases to a softening of certain phonon modes, known as a Kohn anomaly [157]. Moreover, the confinement of the dimensionality can drastically reduce the dielectric screening thereby enhancing the electron-phonon interactions and the CDW strength with it [158, 159]. Not only the reduced dimensionality, but also the optical perturbation and evolution of the electronic and lattice degrees of freedom can drive a considerable change in the electron-phonon coupling of thin films [160] and most recently of 2D TMDCs [161].

Hereby, by tuning the pump fluence within a pump and probe scheme, a wide range of electronic temperatures is explored on the 2D metallic TMDC TaS_2 introduced in Chap. 3, giving access to a considerable change of the screened electron-phonon interactions on a ultrafast scale [162, 105, 59].

4.2 Electronic temperature decay

tr-ARPES measurements of SL TaS_2 were shown in Fig. 3.5 in Chap. 3 in terms of subsequent snapshots of the photoemitted intensity following an optical pump pulse [77]. These were obtained at increasing higher time delays within a region of the $(E;k)$-space contained in the grey box shown in Fig. 3.3(a) tracking the carrier ultrafast dynamics on a femtosecond scale. As the system underwent optical excitation the hot electrons extended on the unoccupied band above the centre of the Fermi-Dirac distribution.

The dynamic changes that were extracted from the model fit of the dispersion during the relaxation process are given in Fig. 4.1(a) and (b). Fig. 4.1(a) shows the time dependent ΔW (i.e. the difference between the band minimum energy in the excited and equilibrium state defined in Chap. 3), which exceeds 100 meV at the peak excitation, corresponding to roughly a third of the total occupied bandwidth [77]. Fig. 4.1(b) shows the electronic temperature T_{el}, exceeding 3000 K at the peak excitation due to the relatively low value electron heat capacity C_{el}, as it will be shown later in grater detail. Both T_{el} and ΔW are well defined already at 40 fs and they show a similar trend toward higher time delays. The time-dependent ΔW and T_{el} are fitted best by a double-exponential decay function with a relaxation time τ_1 well below 1 ps and a slower one, τ_2 [77]. Even though measurements acquired above 5 ps were disregarded for the difficulties in

accounting for space charge and surface photovoltaic effects in the model fit of the photoemitted intensity, the measurements could still be extended up to 30 ps, without noting significant change in ΔW and T_{el} (not shown here), meaning that the values of τ_2 presented in Fig. 4.1(a) and (b) were probably underestimated and could be much higher. Nevertheless, as τ_2 cannot be determined with certainty, from now on only time delays up to 2.5 ps will be considered, i.e. just enough to disregard τ_2 while preserving the quality of a single exponential fit.

The similarity in the fitting results between ΔW and T_{el} was explicated in Chap. 3 and depends on the relation shown in Eq. (3.4). In this Chapter the focus will be on the time evolution of T_{el} that is related to the transfer of the electronic energy to the lattice.

4.3 Transfer of the electronic energy to the lattice

A sketch shown in Fig. 4.1(c) illustrates the nature of this energy exchange. The ultra-short laser pulse incident on the sample creates a non-equilibrium distribution within the electron gas, characterised by carrier population inversion. Subsequent thermalisation via electron-electron scattering processes occurs on a timescale quicker than our experimental time resolution of 40 fs, as it was pointed out in Sec. 3.4. Therefore, the hot carrier population can be fully accounted for by a Fermi-Dirac distribution, $f(E, T_{el})$, with heightened T_{el} for the whole time scale probed in this experiment [77]. In fact, when the laser pulses are relatively long and intense, the thermalization of nonequilibrium electrons in metals is expected to happen even on a attosecond time scale, i.e. immediately compared to the characteristic time of electron-phonon energy exchange ranging from hundreds of femtoseconds to hundreds of picoseconds [163].

Typically, while electrons are very hot from the beginning of the relaxation process, the lattice is not expected to be immediately heated due to their larger heat capacity [162, 164]. This imbalance leads to the gradual energy exchange between these two systems, and studying how quickly the energy is transferred, which kind of phonons are involved and if there are any bottlenecks in the carrier relaxation is the aim the study in this Chapter.

The electron-hole recombination, as represented in Fig. 4.1(c) and (d), is mediated by energy transfer to the lattice *via* incoherent coupling of the hot electrons to the phonon popula-

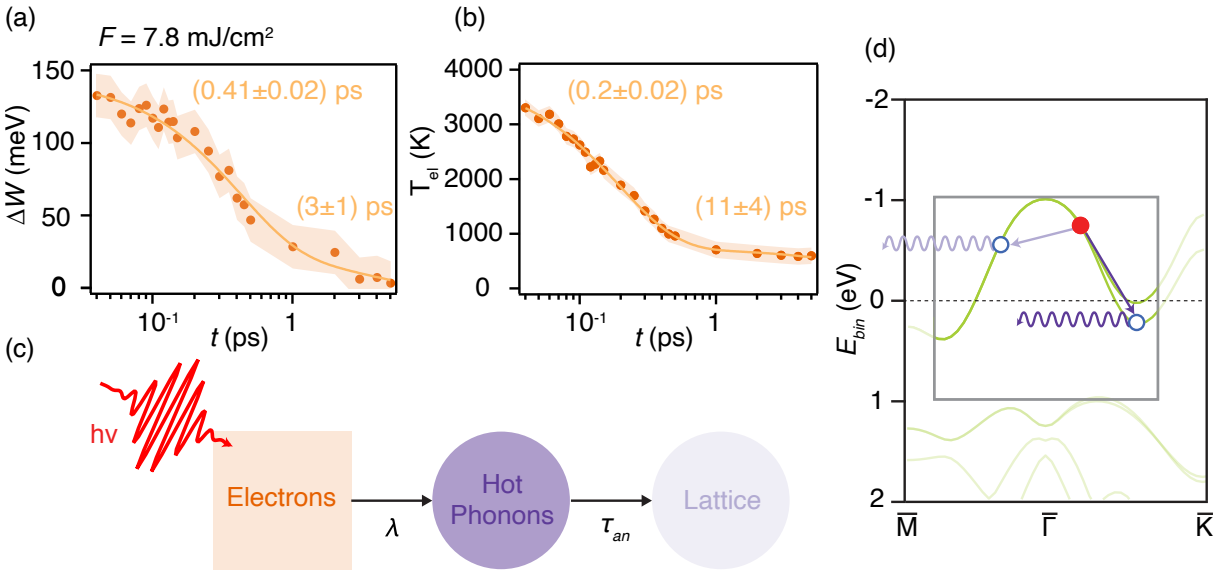

Figure 4.1: (a) and (b) Parameters extracted from the data set presented in Fig. 3.5 for a pump fluence of $F = 7.8$ mJ/cm^2 and sample temperature of $T_{sample} = 298$ K. (a) Extracted band shift ΔW as a function of time delay within the error bar estimated from the model fit (shaded area) [77]. A double exponential function fit is shown (solid line) and the characteristic relaxation times τ_1 and τ_2 are given. (b) Corresponding data and fit for the time dependent electronic temperature T_e. (c) Sketch of the energy transfer during the excitation and relaxation process. The pump pulse (red) gives energy to the electrons (orange) which generate hot phonons (deep purple) depending on λ from Eqs. (4.1) and (4.2). Hot phonons dissipate their energy to the lattice batch (light purple) depending on the time scale τ_{an} from Eqs. (4.2) and (4.3) [162]. (d) Representation of the relaxation of an electron (red filled circle) filling a hole (blue open circle) on the band structure of SL TaS_2 by emission of a strongly coupled sc phonon (deep purple wavy arrow) or a weakly coupled phonon mediated by sc phonons (light purple wavy arrow). The region enclosed by the grey square highlights the portion of the $(E;k)$-space probed in the TR-ARPES experiment, as also seen in Fig. 3.3.

tion through different competing channels with characteristic decay times and electron-phonon coupling strengths. In graphene, for example, the hot carrier dynamics is dominated by a fast decay (0.2 ps) mediated by optical phonons and a slower one (3 ps) assisted by impurities (supercollisions) and acoustic phonons [105, 59]. The fast characteristic time constant of the carrier relaxation in graphene clearly recalls τ_1 of SL TaS_2, pointing at the presence of excitations of a specific set of phonon modes in the TaS_2 layer that couple strongly with the hot electrons gas.

In particular, the anisotropy of the electron-phonon interaction can be considered by distinguishing between two lattice subsystems at two distinct effective temperatures depending

on the electron-phonon coupling strength λ. Above an arbitrary critical value, λ_c, strongly-coupled (sc) phonons set in [165]. These are represented for SL TaS_2 in deep purple in Fig. 4.1(c) and (d). On the contrary, weakly-coupled and nearly noninteracting phonons account for the remaining modes of the crystal lattice [162], as shown in light purple. The electronic temperature, T_{el}, as well as the temperature of the sc phonons, T_{ph}, and that of the remaining lattice batch, T_{lat}, fully define the temporal evolution of the dynamics through a system of three time dependent energy transfer rate equations in a phenomenological three temperature model (3TM) [162, 105].

$$\frac{dT_{el}}{dt} = \frac{F\,S(t)}{\beta} - \frac{N_A\,\pi\lambda\,g(E_F+\mu(T_{el}))\,[\hbar\omega_{ph}]^3}{\hbar}\frac{n_{el}-n_{ph}}{C_{el}}, \tag{4.1}$$

$$\frac{dT_{ph}}{dt} = \frac{N_A\,\pi\lambda\,g(E_F+\mu(T_{el}))[\hbar\omega_{ph}]^3}{\hbar}\frac{n_{el}-n_{ph}}{C_{ph}} - \frac{T_{ph}-T_{lat}}{\tau_{an}}, \tag{4.2}$$

$$\frac{dT_{lat}}{dt} = \frac{C_{ph}}{C_{lat}-C_{ph}}\frac{T_{ph}-T_{lat}}{\tau_{an}}, \tag{4.3}$$

where in the Eqs. (4.2) and (4.3) an anharmonic phonon-phonon coupling term is added to the two-temperature model determined by Allen [166] in order to account for the lattice temperature T_{lat} [162, 167, 105]. F, $S(t)$ and β in the first term of Eq. (4.1) refer to the pump fluence, the Gaussian pulse shape that describes the laser field of the pump pulse and the absorbed thermal energy per unit area, respectively. As the measurement of the pump fluence was unstable across different datasets, the value attributed to the fluence was calibrated by matching to a calibration line based on a linear fit of several consistent fluence measurements [77]. In the second term of Eq. (4.1), N_A refers to the Avogadro's number, λ is the electron-phonon coupling strength, ω_{ph} is the frequency of a single Einstein phonon mode, n_{el} and n_{ph} are Bose-Einstein distributions at T_{el} and T_{ph}, respectively, $g(E_F+\mu(T_{el}))$ is the electronic DOS evaluated at $E_F+\mu(T_{el})$, where the chemical potential, μ, is modulated by T_{el} as described in [77]. τ_{an} in Eqs. (4.2) and (4.3) is the anharmonic phonon-phonon decay time parameter represented in Fig. 4.1(c) that accounts for the typical time scale that is required to for the sc phonons to transmit energy to the remaining lattice. C_{el}, C_{ph} and C_{lat} are the electronic, sc phonon and lattice heat capacities, respectively. These will be addressed later in greater detail.

The phenemenological 3TM relies on fitting the temperature extrapolated from the simulation of the photoemitted intensity, T_{data}, while having a set of parameters from Eqs. (4.1)–(4.3)

free to vary, as later explained. This fit is run for different datasets acquired at increasing pump fluences and at different sample temperatures, T_{sample}, as shown in Fig. 4.2(a)–(c). While in Fig. 4.1(b), T_{data} is represented only from the excitation peak onward, in Fig. 4.2(a)–(c) is also shown at negative time delays and around the temperature rise. In order to perform the best fit, it is necessary to account for the rise first by fitting the parameters β and a $S(t)$, as they are strongly constrained by the maximum of T_{el}, i.e. $T_{el,max}$. Despite the fact that β has the dimension of a heat capacity, it is not a well-defined quantity during the out-of-equilibrium transient state in the presence of the pump pulse [105]. It should rather be taken as a scaling parameter as it depends on a number of factors such as scattering and pump-probe overlap which are local in nature and therefore cannot be modelled easily. A further fitting step, letting λ and τ_{an} free to vary while fixing all the other parameters, provides an electronic temperature fit that lies within the data error bars, as seen in Fig. 4.2(a)–(c). A λ- and τ_{an}-resolved image of the minimized χ^2 associated to the fits in panels Fig. 4.2(a)–(c) is displayed in panels Fig. 4.2(d)–(f). The χ^2 maps were adopted to explore the correlation between λ and τ_{an}.

From the fit, T_{ph} and T_{lat} were also obtained following Eqs. (4.1)–(4.3), as well as other relevant constants, like $T_{el,max}$ that takes place at time $t_{el,max}$, the maximum of the phonon temperature $T_{ph,max}$ and $t_{ph,max}$ and the characteristic relaxation times of T_{el}, T_{ph} and T_{lat} (τ_{el}, τ_{ph} and τ_{lat}, respectively). While $T_{el,max}$ is simply related to the number of carriers that are excited above E_F, $t_{el,max}$ describes, within the limit of time resolution, how long does T_{el} requires to be found at the related excited state, and τ_{el} how long does T_{el} requires to fall of a factor of $1/e$ (note, therefore, that the general constant $\tau_{el,ph,lat}$, defined simply as τ from here on, is qualitatively different from τ_{an} as it solely describes the temperature relaxation time, while τ_{an} refers to phonon-phonon coupling extrapolated from the 3TM rate equations). The value of τ_{el}, seen in Fig. 4.2(a)–(c), results being similar to τ_1 from Fig. 4.1(b). The reason is that the decay of T_{data} in Fig. 4.2 is now best fitted by a single exponential function rather than a double exponential function. In fact, time delays were considered only up to 2.5 ps, disregarding the dynamics taking place at longer times. $t_{ph,max}$ describes how fast the sc phonons respond to the energy transfer from the electron gas and τ_{ph} is a measure of how fast does T_{ph} decays. Exception is made for τ_{lat} that is defined here as a rise characteristic time related to an increase of T_{lat} of a factor $(e-1)/e$. The reason behind a different definition of τ_{lat} is that, as mentioned before, a plateau is established after $t = 1$ ps that would decay at time delays that were not probed in this experiment. Hence, τ_{lat} measures the typical time scale of energy exchange between sc

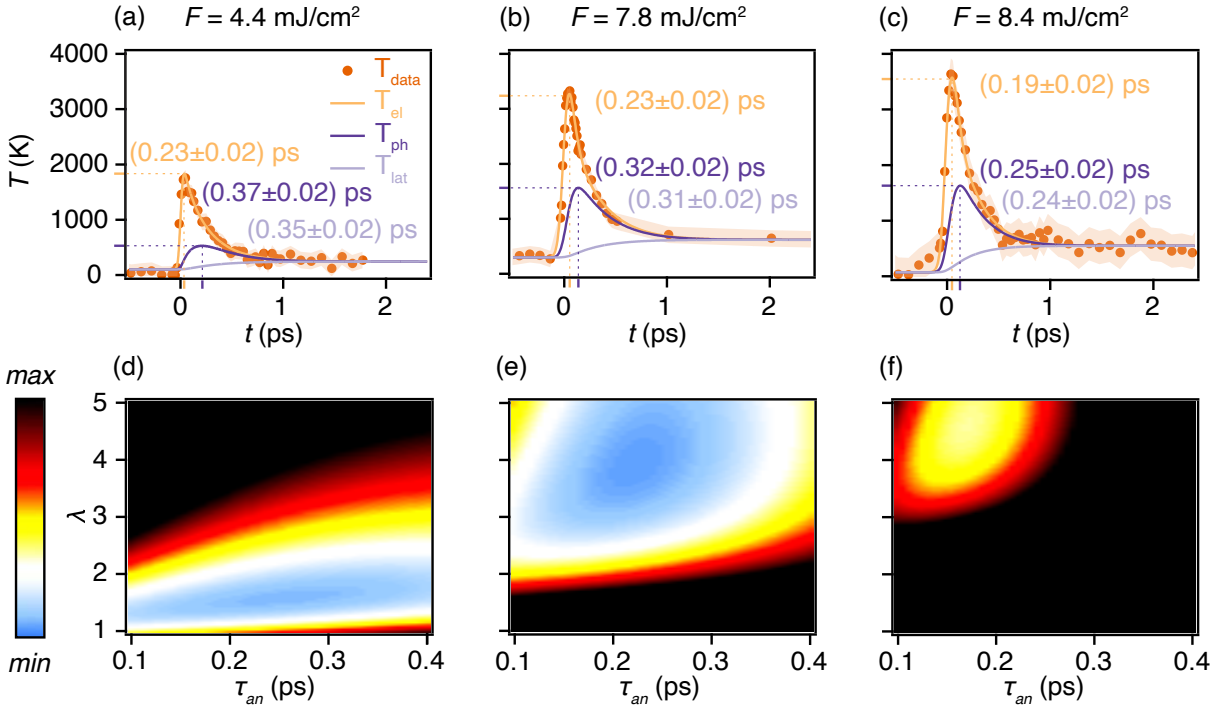

Figure 4.2: (a)–(c) Temporal development of T_{data}, within the related error bars obtained from the simulations (shaded area), and of T_{el}, T_{ph} and T_{lat} for a pump fluence and sample temperatures of (a) $F = 4.4$ mJ/cm^2, $T_{sample} = 103$ K, (b) $F = 7.8$ mJ/cm^2, $T_{sample} = 298$ K and (c) $F = 8.4$ mJ/cm^2, $T_{sample} = 73$ K. An Einstein mode at 15 meV was considered in order to account for the calculated heat capacities involved in the 3TM fits in this figure. The characteristic relaxation time constants, τ, are given in the panels for T_{el}, T_{ph} and for the heating of the lattice, T_{lat}. $T_{el,max}$ and $T_{ph,max}$ as well as the related time delays $t_{el,max}$ and $t_{ph,max}$ are labelled by ticks on the axis in orange and deep purple respectively. (d)–(f) Measure of the goodness of the 3TM fit in (a)–(c), respectively, by plotting the χ^2 value as a function of λ and τ_{an}.

phonons and the lattice batch in order to reach a metastable state at $T_{el} > T_{sample}$.

From the constants extrapolated from the fits in Fig. 4.2(a)–(c), it is possible to observe a consistent pattern across increasing pump fluence datasets. First, $T_{el,max}$ and $T_{ph,max}$ are monotonically increasing with fluence. This is not surprising because the number of hot electrons excited in the conduction band increases as the pump laser fluence increases, involving a raise of T_{el} that is proportional to the number of excited electrons. Thus, a higher $T_{el,max}$ necessitates an increase in $T_{ph,max}$ as the energy is transmitted to the sc phonons. T_{el} equilibrates with T_{ph} and T_{lat} (i.e. $T_{el} \simeq T_{ph}$) around 1 ps after the excitation, regardless of the pump fluence. This is not to be given as granted, as in graphene, for example, T_{el} equilibrates with T_{lat} at longer

timescales [105]. Even more surprising is the monotonous decrease of $t_{ph,max}$, τ_{ph} and τ_{lat} with fluence. In fact, these respectively imply a faster rise and subsequent decrease of T_{ph}, as well as a faster increase in T_{lat}. Therefore, this behaviour points toward a general faster response of the lattice to the changes in the carriers distribution as the fluence increases. On the other hand, nothing can be said for $T_{el,max}$, as it always lies at $t = 0$ within the given error bar, confirming that the thermalization takes place within the experimental time resolution.

In order to better understand the reasons behind this response, it is necessary to address the calculation of the parameters λ and τ_{an} in the fitting of T_{data} by means of λ- and τ_{an}-resolved χ^2 maps, as shown in Fig. 4.2(d)–(f). Here, it is clear that as the fluence increases the optimal value of the fitting parameter λ also increases while the optimal τ_{an} decreases. This is a clear indication that the fast and strong response of the lattice vibrational modes to the carrier excitation is triggered by the increase of λ. A fluence-dependent decreasing value of τ_{an}, instead, explains why the sc phonons give out energy to the lattice faster involving a shorter τ_{ph} and τ_{lat}. The value of χ^2 resulting from the fit is more localized with respect to λ at lower fluences, meaning that the uncertainty associated with the determination of λ will be proportional to fluence and, therefore, to the associated value of λ, while no significant variation is observed in terms of the uncertainty related to τ_{an}.

As the 3TM in the current analysis is a phenomenological model, it is appropriate to explore different physically meaningful variants of the model to prove the stability of the fits. For instance, the very interpretation of the heat capacity $C = \lim_{\Delta T \to 0} \frac{\Delta Q}{\Delta T}$, where ΔQ is the discrete amount of heat required to raise the temperature of an object by ΔT, didn't find a unilateral interpretation in history [168, 169, 170]. Thus, also in this experiment, understanding which physical model of C is most suitable to the system is a question of major concern. The heat capacities in this study are generally defined as:

$$C_{el} = N_A\, k_B\, \frac{d}{dT_{el}} \int_{-\infty}^{+\infty} g(E_F + \mu(T_{el}))\, E\, f(E, T_{el})\, dE', \tag{4.4}$$

$$C_{ph} = N_A\, k_B\, \frac{d}{dT_{ph}} \int_{\omega_i}^{\omega_f} D(\omega)\, \hbar\omega\, n(\omega, T_{ph})\, d\omega', \tag{4.5}$$

$$C_{lat} = N_A\, k_B\, \frac{d}{dT_{lat}} \int_{-\infty}^{+\infty} D(\omega)\, \hbar\omega\, n(\omega, T_{lat})\, d\omega', \tag{4.6}$$

where k_B is the Boltzmann constant and D is the phonon DOS.

C_e can be derived numerically by the knowledge of the electronic DOS of the system [77], whereas C_{ph} and C_{lat} require D and of the Eliashberg function for SL TaS_2, $\alpha^2\mathcal{F}(\omega)$, which was determined by means of density functional perturbation theory by Hinsche *et al.* [132]. By consideration of the value of $\lambda = 2\int_0^{+\infty} \frac{\alpha^2\mathcal{F}(\omega)}{\omega} d\omega$ across the momentum and frequency dependent phonon modes, a high value of λ above an arbitrary $\lambda_c = 1$ was found at a phonon frequency of $\omega_{ph} = 120\ \mathrm{cm}^{-1}$, corresponding to an energy of $\hbar\omega_{ph,1} \simeq 15$ meV. Furthermore, from the theoretical calculations of the renormalization of the electronic structure due to electron-phonon interaction, kinks are predicted to take place in the low temperature regime at a phonon frequency of $\omega_{ph} = 360\ \mathrm{cm}^{-1}$, which corresponds to energies of $\hbar\omega_{ph,2} \simeq \pm 45$ meV around E_F in the SL TaS_2 band, roughly corresponding to the maximal available phonon energy [132]. As it is not possible to assume *a priori* which phonon strongly couples to the hot electrons, a test of C_{ph} at both energies $\hbar\omega_{ph,1}$ and $\hbar\omega_{ph,2}$ is carried out. In order to numerically determine C_{ph}, the integral in Eq. (4.5) has to be run within an arbitrary phonon energy range $\Delta\hbar\omega = \hbar\omega_f - \hbar\omega_i$ around the values $\hbar\omega_{ph,1}$ and $\hbar\omega_{ph,2}$. For the sake of verifying the effect of $\Delta\hbar\omega$ on C_{ph}, two different values of $\Delta\hbar\omega$ were also tested, namely $\Delta\hbar\omega_{Small} = 1.7$ meV and $\Delta\hbar\omega_{Large} = 4.8$ meV. In this way, it should be possible to asses how a different number of sc vibrational resonators included in $\Delta\hbar\omega_{Small,Large}$ will affect C_{ph} and, therefore, $T_{ph}(t)$. The two chosen frequencies, $\hbar\omega_{ph,1}$ and $\hbar\omega_{ph,2}$, are highlighted within the phonon energy interval $\Delta\hbar\omega_{Small}$ in Fig. 4.3(b). Moreover, as the phonon dispersion around $\hbar\omega_{ph,1}$ and $\hbar\omega_{ph,2}$ is almost flat, an Einstein model can be also considered for both phonon energies of the sc mode:

$$C_{ph,E} = N_A\, k_B \left(\frac{\omega_{ph}}{k_B T_{ph}}\right)^2 \frac{e^{\omega_{ph}/k_B T_{ph}}}{\left(e^{\omega_{ph}/k_B T_{ph}} - 1\right)^2}. \tag{4.7}$$

In this way, 6 different models of C_{ph} were tested in total. These are shown in Fig. 4.3(a) alongside C_{el} and C_{lat}. It was verified that when $\Delta\hbar\omega_{Small}$ at $\hbar\omega_{ph,2}$ is implemented in Eq. (4.5) the optimal value of χ^2 is obtained for the fits in Fig. 4.2(d)–(f)

4.4 Fluence-dependent electron-phonon coupling

Fig. 4.4(a)–(d) show the pump fluence dependence of some of the relevant parameters presented in the previous paragraph, namely T_{max}, t_{max} and τ, obtained as in Fig. 4.2(a)–(c), but

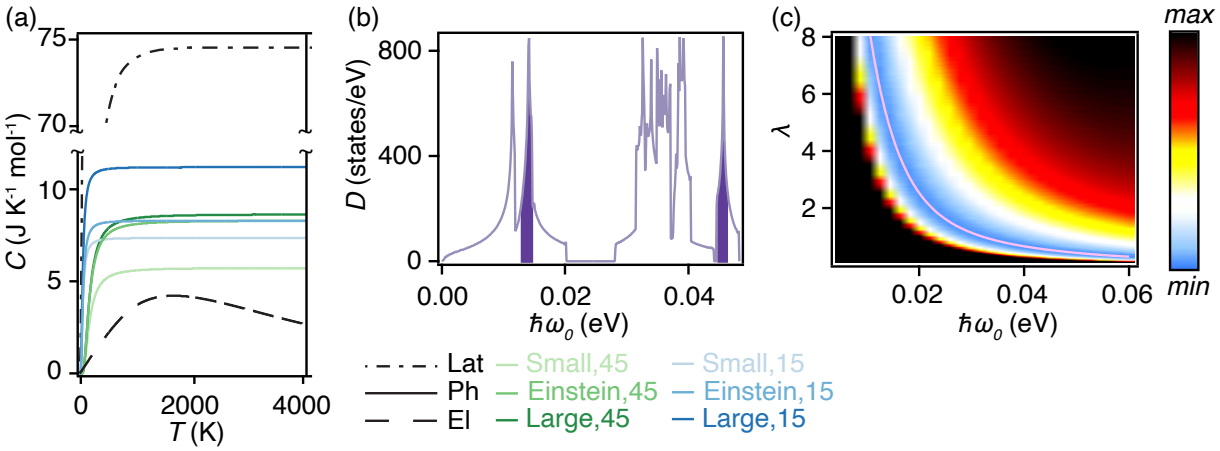

Figure 4.3: (a) Temperature-dependent C_{el}, C_{ph} and C_{lat}. The dashdotted line, the solid line and the dashed line refer to lattice, sc phonon- and electron-related parameters, respectively. Blue (green) colours are used when $\hbar\omega_{ph,1} = 15$ meV ($\hbar\omega_{ph,2} = 45$ meV) is adopted in Eqs. (4.1), (4.2), (4.5) and (4.7). *Small* (*Large*) implies that Eq. (4.5) was used to define C_{ph} with $\Delta\hbar\omega_{Small} = 1.7$ meV ($\Delta\hbar\omega_{Large} = 4.8$ meV), while *Einstein* refers to $C_{ph,E}$ in Eq. (4.7). (b) Phonon DOS, D, as function of phonon energy. The phonon energy range $\Delta\hbar\omega_{Small} = 1.7$ meV is labelled by a shaded area in deep purple around $\hbar\omega_{ph,1} = 15$ meV and $\hbar\omega_{ph,2} = 45$ meV. (c) χ^2 as a function of λ and $\hbar\omega_0$. A double exponential fit of the λ dependent χ^2 minima is overlaid to the graph in pink.

now involving six different phenomenological models, as explained in the previous paragraph and in the figure caption. Fig. 4.4(a) clearly confirms that, despite the different models, the linear increase of both $T_{max,el}$ and $T_{max,ph}$ is consistent with the behaviour presented for the analysis of Fig. 4.2(a)–(c), as it does not vary across different models within the estimated error bars.

Likewise, $t_{max,ph}$ in Fig. 4.4(b) presents a consistent linear behaviour when compared to Fig. 4.2(a)–(c) across the fitting models, even though in this case there is a more pronounced difference in the line steepness, depending on the model. For instance, the largest deviation in steepness is obtained between the *small* model at $\hbar\omega_{ph,1} = 15$ meV and *large* model at $\hbar\omega_{ph,2} = 45$ meV which reflects the highest difference in the values of the related C_{ph} in Fig. 4.3(a) at the Doulong Petit limit. Despite the large changes in $t_{max,ph}$, it is not possible to resolve any change of $t_{max,el}$ within the time resolution of our experiment and, most likely, a precise tracking of the charges at excitation could be done only on a subfemtosecond time scale. Furthermore, as the differential equations are set-up such that the energy must flow from elec-

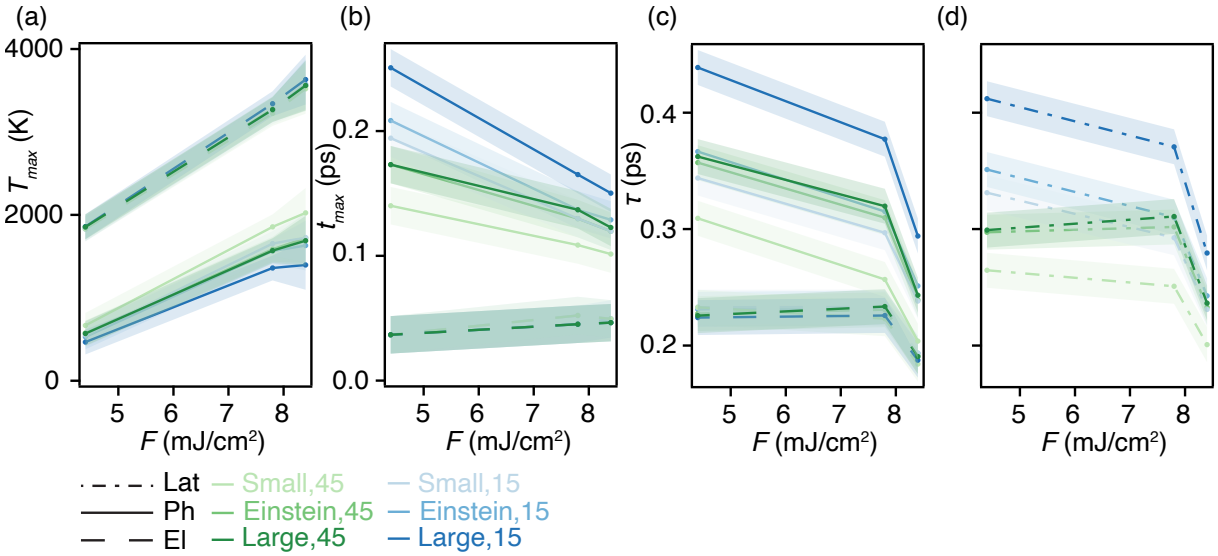

Figure 4.4: (a)–(d) Legend as in Fig. 4.3(a). Temperature-dependent C_{el}, C_{ph} and C_{lat}. Pump fluence dependence of (b) T_{max}, (c) t_{max} and (d) τ. The coloured shaded area refers to the estimated error bars.

trons to phonons, the values of $t_{max,ph}$ are greater than $t_{max,el}$ at any fluence, confirming that the carriers are always the one to be excited first with respect to the phonons.

τ in Fig. 4.4(c) and (d) manifests a somewhat more complex behaviour in relation to fluence. The general value of τ undergoes a sudden drop at $F = 8.4$ mJ/cm^2 suggesting a non-linear relation of τ with fluence. It is speculated that a threshold to the increase in anharmonic coupling is found at increasing fluences, however more datasets should be taken at several fluences, especially around $F = 8$ mJ/cm^2, to clearly assess whether such threshold is established or not. Despite the fact that τ_{el} is typically the shortest, pointing to a faster dynamics, τ_{ph} and τ_{lat} show similar time length, indicating a similarity between the lifetime of the excited sc phonon state and the characteristic time at which T_{lat} increases. This, at the end, results in T_{ph} and T_{lat} equilibrating with T_{el} almost at the same time, as it was shown in Fig. 4.2(a)–(c). The value of τ_{ph} and τ_{lat} is clearly influenced by the fitting model adopted, comparably to $t_{max,ph}$ in Fig. 4.4(b).

Once again, the calculation of the parameters λ and τ_{an} in the fitting of T_{data} plays a pivotal role in understanding the ultrafast dynamics of SL TaS_2. In Fig. 4.5(a) and (b), λ and τ_{an} are respectively displayed as a function of pump fluence. First of all, it is evident that λ always shows a clear monotonously increasing relation with fluence. As pointed out before, an

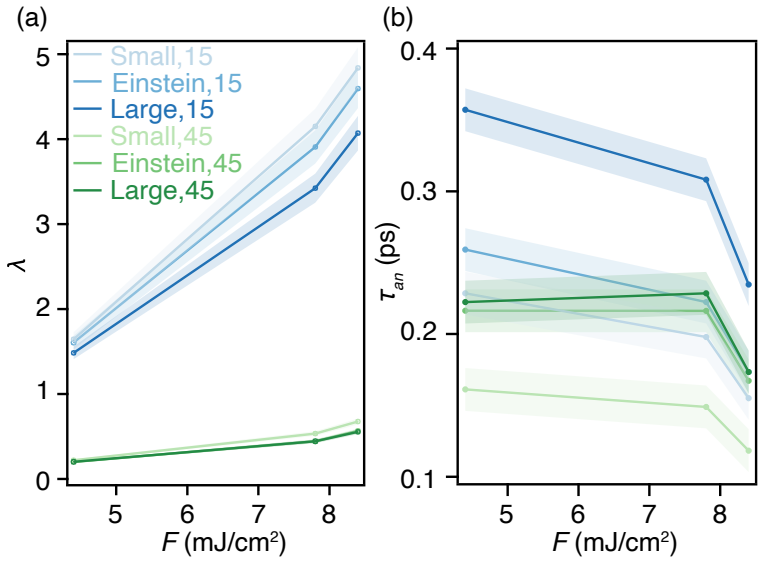

Figure 4.5: Pump fluence dependence of (a) λ and (b) τ_{an} as extrapolated by the minimum of the χ^2-maps. Colour scale and labels are the same as Figs. 4.3 and 4.4. The extrapolated λ related to *Small, 45* in (a) is hidden behind λ related to *Large, 45*. The coloured shaded area refers to the estimated error bars.

increasing value of λ involves a more efficient energy transmission between the carrier population and the sc phonons for which the values of $T_{max,ph}$ will be higher and that of $t_{max,ph}$ lower. This effect is attributed to the impact of electronic screening on the lattice vibrations that could be obtained at such a high temperature regime. Further investigation on the alteration of the electron-phonon interactions through the excitation and relaxation processes needs to be carried, similarly to previous researches on 1T-VSe_2 [161]. This would require the calculations of T_{el}-dependent phonon dispersion and associated mode-resolved electron-phonon coupling. Furthermore, it is evident that there is a clear separation in the λ values that depends on $\hbar\omega_{ph}$. In fact, by running the fit for several increasing Einstein frequencies it emerges that the best value of λ is inversely proportional to $\hbar\omega_{ph}$ according to a double exponential relation, as it was shown in Fig. 4.3(c). It should be pointed out that, as $\lambda > 2$ is considered unphysical, $\hbar\omega_{ph,2}$ should be rather taken into account in line with the fact that best value of χ^2 were obtained at that phonon energy.

Finally, in Fig. 4.5(b), τ_{an} shows a similar behaviour to τ in Fig. 4.4(c) and (d). Indeed, the value of τ_{an} is apparently constant until a fluence of $F = 7.8$ mJ/cm^2, but then it suddenly drops at $F = 8.4$ mJ/cm^2. This indicates that the sc phonons tend to transfer energy to the

lattice faster only at very high fluences, motivating the similarity with τ_{ph} and τ_{lat}. τ_{an} show a strong model dependence which is highly influenced by the value of C_{ph} at the Doulong Petit limit.

In conclusion, it was demonstrated that the ultrafast dynamics in TaS_2 are well described by a three-temperature model in which the energy is transferred in a first moment by the excited electrons to the sc photons which later release their energy to the lattice batch. Curiously, the strength of the electron-phonon coupling interaction, as well as the characteristic time scales involved in the phonon relaxation, depends on the experimental pump fluence. It is speculated here that the fluence-dependent electron-phonon interaction is a consequence of the notable changes in the screening caused by the wide range of the electronic temperatures explored. Such a hypothesis could be addressed by implementing the calculation of the phonon dispersion and associated mode-resolved electron-phonon coupling by means of time-dependent density functional perturbation theory for a direct comparison with the temperatures extrapolated from the experimental data.

Chapter 5

Single layer tantalum phosphide compounds

This Chapter is based on the growth and characterization of single layer tantalum phosphide compounds on a Au(111) substrate. The growth resulted in several by-products whose structural analysis will be carried out in this Chapter. Finally, a similar growth procedure will be presented for a different low-index gold crystal surface, Au(110). A novel phosphorous driven reconstructions is observed to take place at the surface of Au(110) and is studied in this Chapter.

The room temperature Aarhus STM and LEED used for the characterization of the samples in the current experiments were located at the SGM3 beamline at ASTRID2 synchrotron based in Aarhus (DK) where the core levels photoemission spectroscopy, usually labelled as X-ray photoemission spectroscopy (XPS) even when performed in the ultraviolet spectrum, by means of synchrotron light was also carried out.

In accordance with the rules of the Graduate School of Natural Sciences, parts of this Chapter were also used in the progress report for the qualifying examination of my PhD education. The contents of this Chapter were neither published nor submitted to a scientific journal. The nature of the research expounded in this Chapter is preliminary, further experimental investigation needs to be carried out in order to conclude the project and draft and submit a manuscript. The sample growth and the data analysis was mainly accomplished by myself with a partial contribution from Ann Julie Holt.

5.1 Single layer TaP compounds as catalysts of the future

TMDCs were introduced in Sec. 3.1 as layered materials which found a renewed interest due to their exotic physical properties, as CDW and unconventional superconductivity, that can be altered by their confinement in two dimensions. 2D TaS_2 was grown in order to explore the many-body interactions involved upon ultrafast carrier excitation. Other than quantum confinement and perturbation of charge carriers, a third way could be simply taken to investigate new many-body physics phenomena: tuning the chemistry of the Ta compound.

In fact, when a group V *pnictogen* element is used instead of the group VI *chalcogen*, the nature of the compound completely changes giving rise to novel quantum states of matter that were unexplored until a few years ago. That is the case, at least, for transition-metal monopnictides, comprised of a transition metal and of a pnictogen element in equal atomic concentration. These are characterized by a tetragonal non-centrosymmetric unit cell divided in of 4 equidistant transition metal planes, interpenetrated with as many pnictogen planes, where each plane exhibits a squared arrangement of the atomic sublattice [171], as sketched in Fig. 5.1(a). The transition metal monopnictide TaAs was recently discovered to host semimetallic dispersion like graphene, with the difference that the low energy excitations are *Weyl fermions* that obey to the Dirac equation derived by Hermann Weyl [172], making TaAs a *Weyl semimetal* [21]. Other studies have also confirmed the presence of topologically protected Weyl semimetals within transition metal monopnictide family [173], including TaP [23], that endow this class of materials with exceptional properties such as extremely large magnetoresistance and ultra-high carrier mobility [174]. Moreover, single crystal TaP was found to be an ideal platform for the study of the interplay between superconductivity and the non-trivial Weyl topological order since the recent discovery of its superconducting state at ambient pressure [175].

The Weyl quasiparticles are believed to be of key importance in catalytic activity and stability of TaP toward the hydrogen evolution reaction (HER, $2\,H^+(aq) + 2\,e^- \longrightarrow H_2(g)$) [176], which is the half cathodic reaction of the water electrolysis ($2\,H_2O(l) \longrightarrow 2\,H_2(g) + O_2(g)$). Photocatalysis of water splitting could, one day, become a breakthrough in environmentally friendly technologies: for example it could be used for storing solar energy in the form of hydrogen on a global scale [177]. Right now platinum is known to be the most effective catalyst toward HER [178]. Nevertheless, its scarcity makes it inconvenient for technological use. Weyl

semimetals are presented as good candidates for replacing topologically trivial metallic catalysts since their surface states are assumed to be topologically robust granting a stable supply of itinerant electrons at the surface, as represented in Fig. 5.1(b). Furthermore, an enhanced room temperature electron mobility of the carriers, caused by the massless fermions in semimetals, drastically reduces the probability of electron-hole recombination, leading to a more efficient redox reaction [176].

Thinning down TaP to the 2D limit, while retaining the lack of inversion symmetry, could uncover exciting electronic properties bringing a new light to the yet unexplored quantum confinement of a Weyl semimetal [179]. For example, 2D Weyl semimetal with intrinsic magnetic ordering are predicted to show new quantum anomalous Hall effect at the crystal edges [179] [1]. The stable supply of topologically protected electrons at the edges of the 2D Weyl semimetal could grant more active metallic edge sites than, for example, those of the SL MoS_2 catalyst [180]. Besides, monolayer trigonal prismatic Ta_2P was predicted to be thermodynamically stable and to show high HER performance by oxygen functionalization [181]. Nevertheless, the prediction of high performance of Ta_2P was based only on the DFT calculated free energy, which is a necessary but not sufficient conditions to determine the HER activity [178]. Thus, experimental evidence is required both to discover possible new fundamental properties of quantum matter while exploring new exciting applications for this class of 2D materials.

The synthesis of atomically thin TaP compounds at the surface could represent a viable way to investigate the catalytic activity of these promising candidates for a greener future. Not only TaP, but also phosphorous *alone* can exhibit bright catalytic properties that one day could have a great impact in modern technology, as it will be shown in the next Section.

5.2 New allotropes of phosphorous

The word *phosphorus* finds its root in the Greek name meaning *light-bringer*. Perhaps it is not a surprise that this material carries exceptional optical properties. In fact, the 2D counterpart of bulk black phosphorous, namely *phosphorene*, has a direct bandgap whose size is dependent on the number of layers [183]. The tunable bandgap energy, alongside with the high hole mobility

[1] The quantum anomalous Hall effect takes place in 2D magnetic insulating system and is characterized by dissipationless chiral channels on the edge of the sample [179].

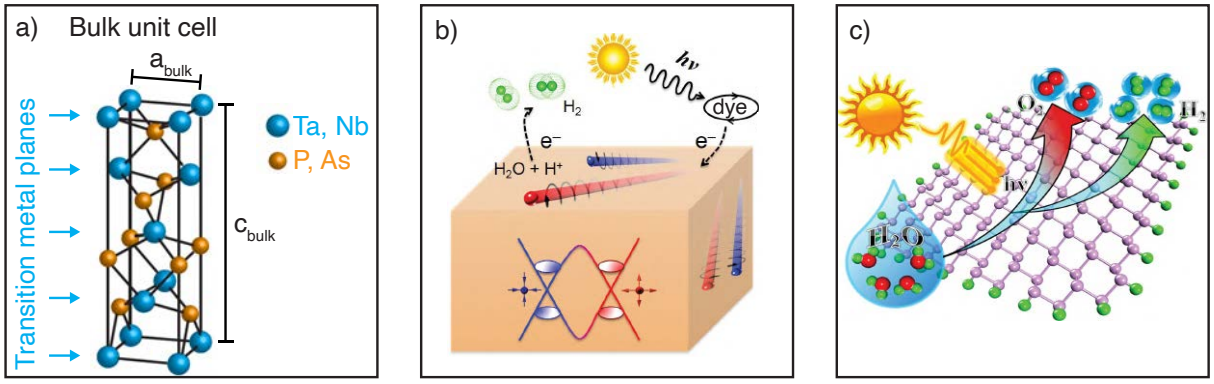

Figure 5.1: (a) Ball model of bulk unit cell of transition-metal monopnictide compounds with space group symmetry $I4_1md$, No. 109 [173]. (b) Model expressing the concept of HER reaction on a Weyl semimetal. The dye is excited and, in the presence of a sacrificial agent, transfers an electron to the surface of the Weyl semimetal, leading to charge separation and, thereby, reducing water to hydrogen. Weyl semimetallic dispersion is represented together with the Weyl fermions travelling on the surface with opposite chirality (blue-red) (from Ref. [176]). (c) Representation of the photocatalysis of water splitting on BlueP quantum dots (from Ref. [182]).

at room temperature [184], makes it an attractive material for electronics and optoelectronics [185, 186]. Furthermore, phosphorene was observed to retain the 2D carrier confinement also in a multilayer thickness [184] which could make the fabrication of phosphorene based devices easier for future applications. Phosphorene was first isolated in 2014 by mechanical exfoliation [185], but synthesis of phosphorene on industrial scale remains still a challenge. It is interesting, therefore, to explore alternative paths for the production of phosphorene.

Among other allotropes of phosphorous, blue phosphorous was predicted to show a formation energy only 2 meV/atom higher than that of black phosphorous and to have an indirect bandgap of ≈ 2 eV tunable with the number of layers [187]. According to theoretical studies, the band gap of *blue phosphorene* (BlueP), a single layer of blue phosphorous, can be also tailored by applying in-layer strain [188] or transverse electric field [189]. Recently, because of its affinity to gas molecules, BlueP has found room in gas sensing applications [190]. BlueP has been synthesized by MBE on Au(111) substrate by deposition of elemental phosphorous [191].

Besides, it has been shown that the spatial distributions of highest occupied and lowest unoccupied molecular orbitals and the size of the band gap varies with the size of BlueP quantum dots. In particular BlueP 0-dimensional nanostructures with lateral diameters between 0.9 nm

and 3 nm are shown to give reasonable reducing and oxidizing capabilities for the full water splitting reaction assisted by visible light [182], as shown in Fig. 5.1(c).

The primary target of the current experiment was to grow epitaxially and characterize atomically thin TaP compounds at the surface of Au(111). As pointed out before, no transition metal pnictide has been grown at the single layer limit to date and, therefore, there is need for experimental evidence on the electronic structure of this novel state of matter [179].

The growth attempt of SL TaP brought to the synthesis of the by-product BlueP [187, 191], which is studied here in detail. In the current project, an alternative path involving PH_3 gas as a precursor for the epitaxial growth of BlueP on Au(111) is presented for the first time in the next Section.

5.3 Growth and structural characterization

Both BlueP and SL TaP compounds are grown epitaxially on Au(111) by means of MBE in UHV. Such a technique was chosen to keep a relatively low level of impurities and to favour the epitaxial growth of atomically thin layers thanks to the typical low deposition rate. It was predicted that BlueP would form preferentially on substrates with hexagonal arrangement of atomic lattice, whilst black phosphorus would rather grow on a substrate with rectangular lattice [187]. Besides, this kind of substrates does not necessarily preclude the possibility to crystals characterized by a square lattice, as the tetragonal TaP presented in Fig. 5.1(a), to form at the surface, as it was demonstrated by our group at the SGM3 beamline [192]. Thus, the choice of Au(111) closely-packed hexagonal lattice certainly plays a major role on the chemical selectivity, i.e. the yield of the chemical reaction at the surface. In fact, it will be shown in Sec. 5.6 that the growth of SL TaP compounds is affected by the choice of the substrate.

Furthermore, the choice of PH_3 as precursor gas is deeply motivated. The high level of toxicity makes PH_3 unpopular among research groups and, even though it has been mainly used to create highly abrupt doping profiles in semiconducting materials [193, 194], it was rarely adopted as reactant gas in a MBE growth process. Nevertheless, PH_3 has been proven to be a good reactant for the production of bulk TaP compounds *via* cracking on Ta surface in a fur-

nace [195]. Additionally, SL TaS_2 was successfully grown by our group at Aarhus University on Au(111) by means of Ta sulphidisation by the related hydrogen calchogenide H_2S [116], and for the reaction with other transition metals [196, 197]: a hint that PH_3 could also be dehydrogenated and react with ta in similar conditions to form SL TaP compounds. In the current project an innovative approach for the phosphidation of Ta by PH_3 on Au(111) for the production of SL TaP compounds is presented.

The use of STM and LEED is of great relevance for monitoring the growth process. While STM gives access to changes in the structure of the surface down to the atomic scale, LEED allows to keep track of changes in the average 2D periodical structure of the overgrowth. In the following two Subsections the reactivity of Au(111) with PH_3 and Ta is presented and the influence of the Ta deposition time (t_{Ta}) on the growth product is shown.

5.3.1 Ta and PH_3 on Au(111)

The experimental growth was accomplished with a base pressure of 2×10^{-10} mbar in the preparation chamber PC1 presented in Sec. 2.2.1. Subsequent 10 min cycles of sputtering at 1.5 KeV Ar^+ at different exposure angles of the sample were followed by annealing at 900 K for 30 min. The procedure was repeated until the surface was atomically clean, exposing the regular $22\times\sqrt{3}$ herringbone reconstruction [198], as shown in the inset in Fig. 5.2(a). The pristine Au(111) surface showed sharp LEED diffractions spots of the herringbone reconstruction recognisable in Fig. 5.2(b) by the satellite spots [199] marked by the green circles in the figure inset. The scan shown in the inset in Fig. 5.2(a) provides atomic resolution and allows the determination of the Au interatomic distance that can be calibrated according to the reference value given above. In order to have a statistically relevant estimate of such and later values of interatomic distances, a Fourier transform (FT) is applied to the atomically resolved image, as shown in the small inset in Fig. 5.2(a), the profile of the FT spots is fitted with Gaussian functions and the reciprocal space length is measured and converted to a real space distance. The reciprocal lattice vectors $\mathbf{a}^*_{Au-STM,1}$ and $\mathbf{a}^*_{Au-STM,2}$ labelled in Fig. 5.2(a) have equal modulus and result in a Au lattice constant $a_{Au-STM} = (0.28 \pm 0.01)$ nm taken with respect to both first nearest neighbours in the BZ labelled in yellow in the FT inset in Fig. 5.2(a). Since this value is coincides with the reference value estimated by previous STM

studies ($a_{Au} = (0.281 \pm 0.007)$ nm [200]) within the uncertainties, it can be assumed that the the in-plane coordinates do not need to be scaled for the follow-up measurements performed on the Au(111) crystal.

The calibration of the z-coordinate was determined by comparing the measured height between two neighbouring Au terraces $a.h. = (0.18 \pm 0.01)$ nm with the STM-based reference value of 0.235 nm [201], resulting in a calibration factor of 1.28 that has to be included for the measured height values thereon [2]. Several profiles were measured and fitted by Boltzmann bent step function to account for the step height and the uncertainty was determined by a convolution of the average uncertainty with the experimentally limited z-resolution of the Aarhus STM. The latter cannot be easily evaluated as it depends on factors such as the tip state or the electrical and mechanical noise. Therefore, the experimental uncertainty must be determined from case to case, however a lower limit is arbitrarily set to 0.01 nm for both lateral and vertical resolution.

Another important parameter that requires calibration is the deposition rate of Ta, deposited through electron beam evaporation unto the surface, as shown in Fig. 5.2(c). A reference Ta flux, quantity related to the deposition rate, is obtained through STM based area determination of 180 sec deposition time of Ta ($t_{Ta} = 180$ sec) on Au(111) ($F = 4.35 \times 10^{16}$ atoms $m^{-2}s^{-1}$) following a calibration method presented in Ref. [202]. The average apparent height of a Ta cluster is $a.h. = (0.25 \pm 0.01)$ nm.

Finally, Fig. 5.2(d) illustrates an STM image of "negative testing" of PH_3 on Au(111) at the same experimental condition of the experiment shown in Sec. 5.3.2, meaning that no Ta was dosed in order to observe the sole effect of PH_3 on the Au(111) substrate. The action of PH_3 at $p = 2 \times 10^{-7}$ mbar and $T = 600$ K for 1 h and 10 min resulted in a lifted herringbone reconstruction. The pits formed at the elbows of the herringbones could be probably ascribed to mild corrosion of Au in that region. Similar results were obtained for $T = 900$ K and $p = 2 \times 10^{-7}$ mbar (not shown here). Currently, there are no studies on the reactivity of Au(111) surface with PH_3, however similar studies were conducted with the parent compound H_2S [203], proving that

[2] As the measured step height varies depending on the convolution of LDOS of the tip with the one of the sample and it does not necessarily represent the effective topographical height, any value of height should be considered as a calibrated apparent height, *a.h.*

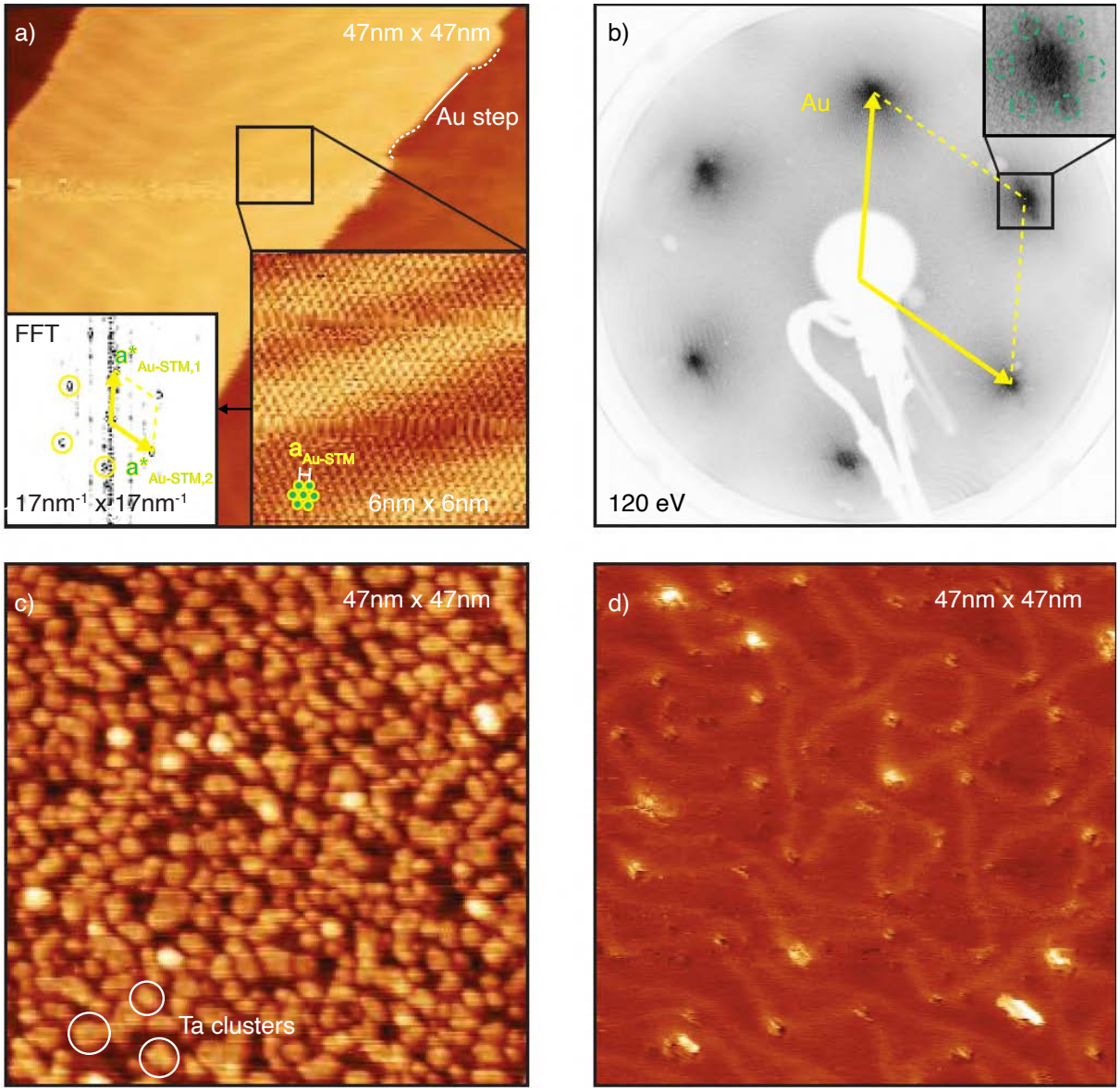

Figure 5.2: STM and LEED of Au(111). (a) STM topographic image of sputtered and annealed Au(111) ($V_b = 1.07$ V, $I_t = 0.11$ nA and color scale range of the apparent height $\Delta h = 0.5$ nm). The big and small insets show atomically resolved Au(111) lattice, marked by the yellow-green circles ($V_b = 1.07$ V, $I_t = 0.38$ nA and $\Delta h = 0.05$ nm), and the relative FT image, respectively. (b) LEED of Au(111). The yellow arrows mark the Au(111) reciprocal lattice vectors, while the green circles in the inset mark the satellite spots related to the herringbone reconstruction. (c) STM topography of Ta clusters on Au(111) ($V_b = 1.25$ V, $I_t = 0.21$ nA and $\Delta h = 0.5$ nm) after 90 sec of Ta deposition at $F = 4.35 \times 10^{16}$ atoms m^{-2}s^{-1} resulting in a coverage of $\theta \approx 0.5$ ML.(d) STM topographic image of Au(111) ($V_b = 0.55$ V, $I_t = 1.03$ nA and $\Delta h = 0.5$ nm) after exposure to PH_3 at p=2×10^{-7} mbar and $T = 600$ K for 1 h and 10 min.

H_2S would neither absorb nor react as PH_3 at similar temperatures on Au(111). Studies were also conducted on PH_3 on Ag(111), showing that PH_3 would not crack at the surface [204]. A more systematic study of Au reactivity to PH_3 by means of mass spectrometry in UHV and XPS could be helpful in the future to understand the reactivity of PH_3 with Au(111) more in depth. Anyway, it was shown that Au(111) does not assist the decomposition of PH_3 enough to obtain phosphorous-based crystal structures at the surface. In the next section it will be shown how Ta is found to be a necessary catalyst for cracking PH_3 at high temperatures, granting the possibility to several new phosphorous and TaP crystal structures to grow at the surface of the Au(111) crystal.

5.3.2 Effect of t_{Ta} on the growth

The actual growth method was firstly elaborated to grow SL TaP, whereas BlueP and other phases resulted as by-product of the reaction at the surface. The growth method consists of two, or eventually three, steps represented in Fig. 5.3(a).

1. In a first step the sample was exposed to a Ta flux at $F = 4.35 \times 10^{16}$ atoms $m^{-2}s^{-1}$ for a tunable deposition time of 60 sec $< t_{Ta} <$ 300 sec.

2. In a second step, the sample was heated up to temperatures of 600 K $< T <$ 1050 K for 20 min in PH_3 atmosphere at $p = 2 \times 10^{-7}$ mbar. Afterwords, the sample was left to cool down to room temperature in the same PH_3 atmosphere or, as it will be shown in Sec. 5.5.2, in UHV environment.

3. A third step could eventually occur where the sample was post-annealed up to temperatures of 800 K $< T <$ 1050 K in UHV.

Several phases are found at the surface, with variable yield depending on the growth conditions. In the first place, some domains were characterized by an hexagonal arrangement of the lattice, marked in Fig. 5.3(b)–(d). These corresponds to the BlueP phase, which will be described in Sec. 5.4. Then some nanoislands are marked in Fig. 5.3(c) and (d). These have a typical irregular rectangular shape, which will be ascribed to SL TaP in Sec. 5.5.1. The surface was also overlaid with clusters that often accumulated at the edges of the TaP islands or on the Au(111) step edges. In this Section, instead, the effect of the growth conditions on the growth

yield is considered.

In particular, the effect of t_{Ta} has proven to be of central importance in the reaction yield, meaning that the quantity of Ta at the surface (or eventually intercalated during the reaction) represents a critical factor. This is evident from the evolution presented in the sequence of panels in Fig. 5.3. On one hand, from a rough analysis of the STM data, it was possible to deduce that an increase in t_{Ta} causes a decrease in average island surface area of BlueP, from $A = (100 \pm 20)$ nm^2 for $t_{Ta} = 60$ sec to $A = (20 \pm 5)$ nm^2 for $t_{Ta} = 180$ sec, alongside with a decrease in BlueP coverage, from $\theta \approx 0.3$ ML for $t_{Ta} = 90$ sec to $\theta \approx 0.16$ ML for $t_{Ta} = 180$ sec. On the other hand, the TaP islands did not change in average island surface area ($A = (80 \pm 10)$ nm^2) with t_{Ta}, but they increased in coverage, from $\theta \approx 0.05$ ML for $t_{Ta} = 60$ sec to $\theta \approx 0.13$ ML for $t_{Ta} = 180$ sec. The nucleation of BlueP is assumed to take place exclusively from the step edges of Au(111) since no BlueP domains are found elsewhere, as it can be seen in Fig. 5.3(b)–(d); SL TaP, instead, did not show any preferential nucleation site on the Au(111) surface.

The evolution of the LEED pattern based on t_{Ta} represented in Fig. 5.3(e)–(g) also confirms an increase in coverage of SL TaP and a decrease in coverage of BlueP while increasing t_{Ta}. In fact, Fig. 5.3(e) resembles the diffraction pattern of BlueP which fades away already at Fig. 5.3(f), leaving room for the diffraction pattern of SL TaP that becomes more and more intense from Fig. 5.3(e) to (g). A more detailed explanation of the diffraction patterns will be given in Sec. 5.4 and 5.5.1 for BlueP and SL TaP, respectively. For $t_{Ta} = 300$ sec neither a clear LEED pattern is recognisable nor the relative STM revealed the step edges of Au (not shown here), implying that an unidentified irregular overgrowth fully covers the surface.

The fact that BlueP is formed in PH_3 atmosphere in the presence of Ta, as shown in Fig. 5.3(b)–(d), but not with Au alone, as seen in Fig. 5.2(d), could be a hint that Ta is the only element to act as a catalyst in lowering the activation energy for the decomposition process of PH_3. Different annealing temperatures were tested while dosing PH_3 with $t_{Ta} = 180$ sec. No hint of reaction was seen by STM at $T = 600$ K, but a similar reaction yield to the one shown in Fig. 5.3(c) was observed at $T = 800$ K (not shown here). This implies that the minimum temperature for the reaction to take place lies between $T = 600$ K and $T = 800$ K. It is relevant at this point to make a comparison with the furnace reaction of bulk Ta with PH_3 presented in Ref. [195].

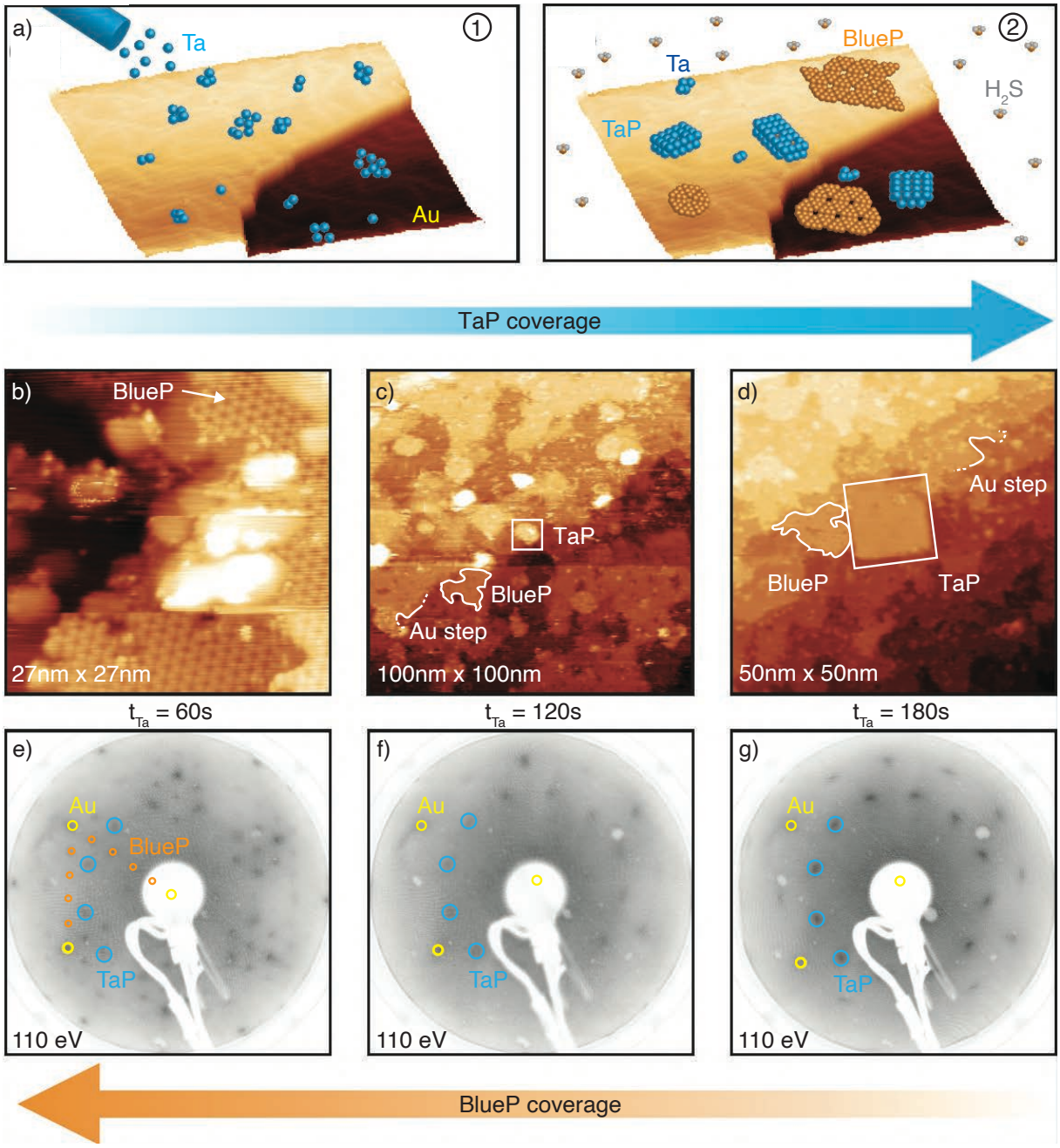

Figure 5.3: (a) Two-step growth model of SL TaP and BlueP on Au(111). Ta is deposited in step 1 and exposed to PH_3 in step 2 at high T. (b)–(d) STM topographic images of SL TaP and BlueP labelled in the panels obtained at increasing or decreasing coverage depending on t_{Ta}. (b) ($V_b = 0.5$ V, $I_t = 0.44$ nA and $\Delta h = 0.5$ nm), (c) ($V_b = 0.77$ V, $I_t = 0.18$ nA and $\Delta h = 1$ nm) and (d) ($V_b = 0.42$ V, $I_t = 0.55$ nA and $\Delta h = 1.5$ nm). (e)–(g) LEED images at different growth stages obtained by tuning t_{Ta} as in panels (b)–(d). The Au(111) diffraction spots are always marked by the yellow circles, while the BlueP and SL TaP diffraction spots are marked in orange and blue, respectively.

According to the measurements of the gaseous reactants partial pressures through quadrupole mass spectrometer and the XPS spectra analysis of reacted Ta, PH_3 was proven to react with Ta at temperatures above 500 K. The pyrolyzed gaseous PH_3 was assumed to form TaH_x at $T \approx 600$ K and TaP compounds at $T \approx 1100$ K that would start to decompose above 1200 K. However, neither a direct prove of the presence of TaH_x was given in Ref. [195] nor direct evidence was found in the current work. A more systematic investigation on Ta core levels in the future could help in understanding the reactivity of Ta at different reaction temperatures. In the following Section the BlueP structure will be presented.

5.4 Study of the BlueP and P-trimer phase structures

DFT calculations [205, 206] showed that at adequately low P coverages, P adatoms prefer to stay apart rather than forming dimers or trimers. Nevertheless, when the surface is populated by sufficiently many P adatoms, nucleation of P islands becomes unavoidable. These would begin to organise as a P-trimer covered surface (P-trimer phase) which, however, was never experimentally observed. In the current experiment it is seen for the first time that a triangular-shaped hexagonal pattern is present at the surface whose measured unit cell constant of $|\mathbf{a_{tr}}| = (0.51 \pm 0.01)$ nm is comparable to the value of $\sqrt{3}|\mathbf{a_{Au}}| = 0.49$ nm of a $(\sqrt{3} \times \sqrt{3})$ R30° composite unit cell with three atoms per unit cell, as represented in the inset in Fig. 5.4(a), superimposed on the STM image. This hypothetical model is proposed based on the predicted tendency of P adatoms to form trimers at sufficiently high P coverage and based on the matching with the observed geometry and lattice constant. Unfortunately, it was not possible to clearly distinguish the coverage of phosphorous by the STM analysis due to the complex morphology of the overgrowth. Moreover, DFT calculated models of the P-trimer phase are shown only for a GaN(001) substrate [205] and not for Au(111). In GaN(001) the trimers are disposed along the same unit cell of the one in Fig. 5.4(a), but they are relatively rotated of 30°. A similar arranging of P-trimers was experimentally detected on Ge(111) [207]. Atomic resolution could elucidate in the future whether the supposed model matches with the atomic lattice.

According to Ref. [206] the P-trimer phase on Au(111) is believed to be a intermediate phase of BlueP, which is reached for higher coverages of P adatoms. The preferred kinetic pathway

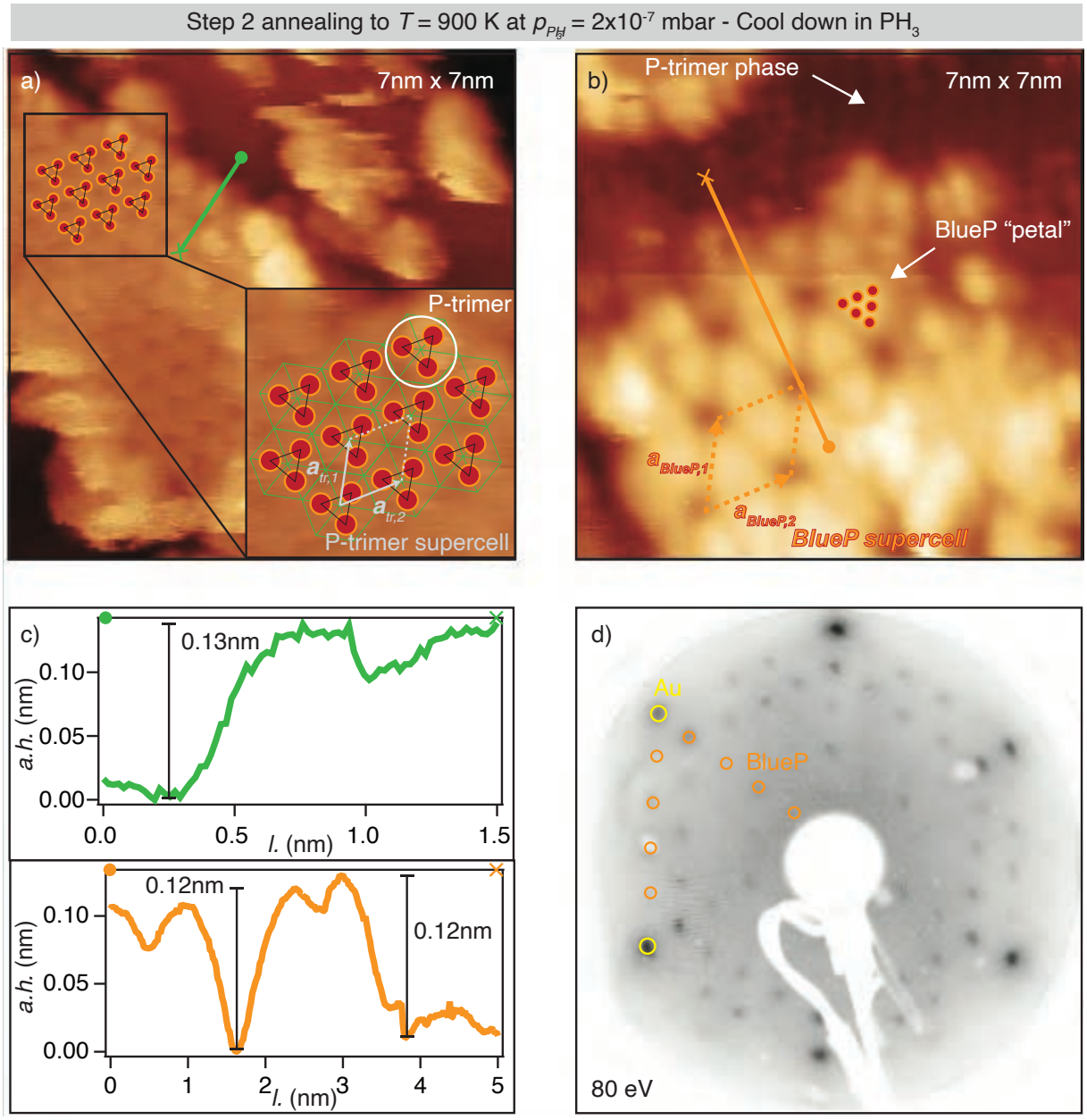

Figure 5.4: STM and LEED of BlueP and P-trimer phase on Au(111). (a) STM topographic image of the P-trimer phase (V_b = 0.05 V, I_t = 1.04 nA and Δh = 0.3 nm). The circles connected by triangles represent the P-trimers, the green lines in the inset mark the Au(111) lattice underneath and the grey lines delimit the unit cell of the P-trimer phase. (b) STM image of a BlueP island on Au(111) (V_b = 0.05 V, I_t = 1.04 nA and Δh = 0.3 nm). The atomic structure of BlueP is superimposed to a *petal* of the hexapetalous-flower-like pattern with orange-red circles. The BlueP supercell is also represented in the image. The sample scanned in panel (a) and (b) was obtained with t_{Ta} = 180 sec. (c) Line profile corresponding to the green (orange) line in panel (a) (panel (b)). (d) LEED image of a sample obtained with t_{Ta} = 60 sec. Yellow circles mark diffraction spots relative to (1×1)-Au(111) and orange circles the ones relative to (5×5)-Au(111) superstructure (or equivalently (4×4)-BlueP).

towards epitaxial growth of BlueP followed a sequential growth behaviour while increasing the P coverage (generated from thermal decomposition of InP) defined as half-layer by half-layer growth model. For low coverages they observed a one-dimensional (1D) chain structure, that would convert to a $(\sqrt{3} \times \sqrt{3})$ R30° superstructure which would in turn become BlueP by increasing the coverage through a dewetting process. During this process the BlueP grows on top and at the expense of the already formed $(\sqrt{3} \times \sqrt{3})$ R30°. In the current work neither the $(\sqrt{3} \times \sqrt{3})$ R30° superstructure nor the 1D chain structure were identified, but a similar dewetting process could potentially transform the P-trimer phase into BlueP. In fact, the P-trimer phase was often lying underneath BlueP, like in Fig. 5.4(b). The measured step height of P-trimer phase is $a.h. = 0.13 \pm 0.01$ nm and is represented by the line profile in Fig. 5.4(c) in green taken from Fig. 5.4(a). This seems to coincide with the upper half-layer of BlueP $a.h. = 0.12 \pm 0.01$ nm as well as with the buckled height of $a.h. = 0.12 \pm 0.01$ nm acquired along the centres of the hexapetalous-flower-like BlueP that will be introduced below. Both apparent heights are shown by the line profile in Fig. 5.4(c) in orange taken from Fig. 5.4(b). Such values are also in agreement with the expected difference in height of 0.12 nm between the top and bottom layers of phosphorus estimated by means of DFT calculation equilibrium configuration [208].

The structure of BlueP results in a top and bottom layers of P atoms where the low- and high-buckled atoms on Au(111) reduce the average P-P bond by 7.8% compared to a freestanding configuration [208]. The resulting unit cell is described by the lattice constants $\mathbf{a}_{BlueP,1}$ and $\mathbf{a}_{BlueP,2}$ distinguished by a trench-like region separating two petals, as shown in Fig. 5.4(b).The modulus of the measured lattice constant of the supercell $|\mathbf{a}_{BlueP-STM}|$ was measured ranging from 1.25 nm to 1.46 nm. The big level of uncertainty is caused by irregularities in the BlueP lattice visible in Fig. 5.4(b) that were also reported elsewhere [209]. The LEED pattern marked by orange circles in Fig. 5.4(d) shows the well-established (5×5) superstructure with respect to the Au(111) unit cell, defined as (5×5)-Au(111), which corresponds to the (4×4) BlueP supercell, identified as (4×4)-BlueP [206, 208, 210, 209].

5.5 Study of the SL TaP compounds structures

As it was mentioned above, the Ta was found to react with PH_3 at elevated temperatures to produce TaP compounds. In the following sections two potential new candidates phases of SL TaP are presented for the first time: a phase belonging to the tetragonal crystal family (T-phase) and another belonging to the hexagonal crystal family (H-phase). Finally a p(2×2) superstructure is found at the surface, which does correspond to neither of the above mentioned phases.

5.5.1 T-phase of SL TaP

The very complex surface morphology and composition of the reaction yield makes the simultaneous analysis of BlueP and SL TaP quite challenging. Therefore, it is desirable to be able to select only one component by desorption of the other or to grow only one in the first place. In the current project a post-annealing procedure is attempted at $T_{PA} = 800$ K for 20 min in UHV (performed on a sample with $t_{Ta} = 180$ sec in the first step and $T = 900$ K for 20 min in PH_3 atmosphere at $p = 2 \times 10^{-7}$ mbar in the second step) and left no traces of BlueP or P-trimer phase, as shown in Fig. 5.5.

Fig. 5.5(a) gives a large overview of the sample morphology after the post-annealing. The steps of Au(111) are marked in the Figure and match with the height of Au(111) steps, but no bare Au could be observed. Instead, the surface is uniformly covered by an unknown phase and is characterized by several holes, clusters (possibly composed of unreacted Ta, or Ta with different oxidation states in TaP_x compounds) and islands that are labeled in Fig. 5.5(a). This unidentified phase is associated to amorphous P on Au(111), as a similar phase was studied by STM imaging in Ref. [191]. The measured depth of the holes is characterized by a two-step height of $a.h. = (0.14 \pm 0.01)$ nm for each step (not shown here). Such an apparent height does match neither the Ta clusters apparent height of $a.h. = (0.25 \pm 0.01)$ nm given in Sec. 5.3.1 nor the monoatomic Au step apparent height of 0.235 nm; thus the substrate could be possibly covered by two layers of amorphous phosphorous.

The nanoislands that are found on the substrate often present a irregular rectangular shape and they show two different heights with respect to the amorphous P phase. These are labelled by *low island* and *high island* in Fig. 5.5(a). The low islands have a typical step apparent height

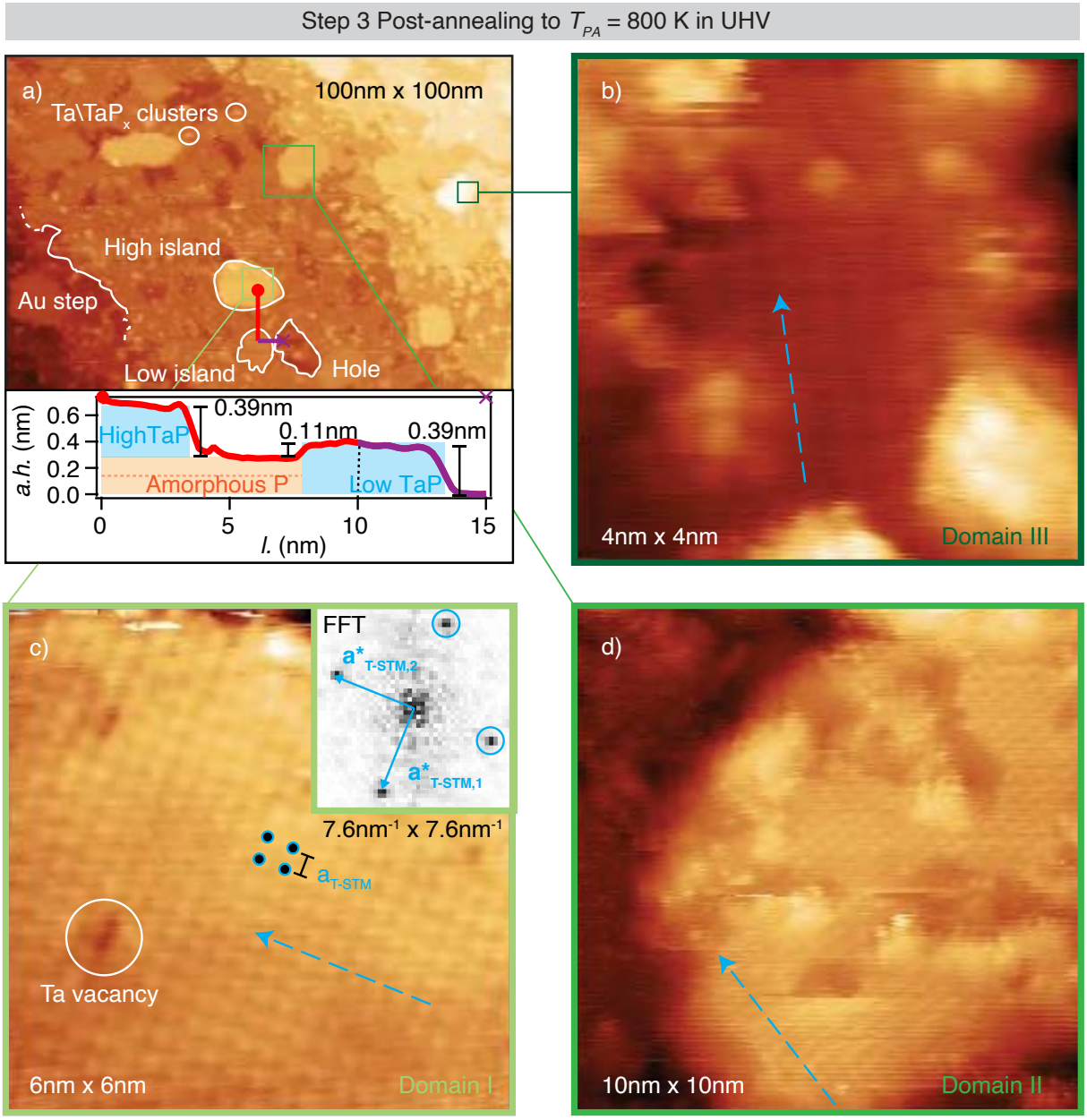

Figure 5.5: STM images of SL TaP of the T-phase on Au(111) for a sample obtained with t_{Ta} = 180 sec and post-annealing at T = 800 K for 20 min in UHV. (a) large scale STM topographic image (V_b = 0.42 V, I_t = 0.74 nA and Δh = 1.7 nm). The Au step, clusters, high and low islands and hole are marked in the image. The inset shows a red-purple *L-shaped* line profile taken across a high and a low islands and a hole. (b) STM close-up image of an island in (a) (V_b = 0.001 V, I_t = 0.79 nA and Δh = 0.3 nm), (c) STM close-up image of an island in (a). The inset shows the FT of the image with the peculiar square reciprocal lattice (V_b = 0.001 V, I_t = 0.71 nA and Δh = 0.2 nm). (d) STM close-up image of an island in (a) (V_b = 0.001 V, I_t = 0.46 nA and Δh = 0.5 nm). The dashed blue arrows in (b) and (d) were obtained by adding up a rotation of 30° starting from the arrow in (c). The TaP square lattice is marked by the blue circles in panel (c).

of $a.h. = (0.11 \pm 0.01)$ nm with respect to the P amorphous phase and the high islands show a typical step size of $a.h. = (0.39 \pm 0.01)$ nm, as it can be seen from the *L-shape* line profile in red-purple taken across these two different islands in Fig. 5.5(a). This entails a difference between the top of the high and low islands of ≈ 0.28 nm, which is equal to the sum of the the two stacked layers of unidentified composition. This means that the high and low islands are actually of the same height, but they are laying on top of the double-P-layer and Au(111) surface, respectively. As SL TaP compounds were never isolated from the bulk to a substrate, it is not possible to compare the island apparent height with any reference value. However, it was found that the Ta interplanar distance in the bulk unit cell of TaP, shown in Fig. 5.1(a), is equivalent to $c_{bulk}/4 = 0.284$ nm [23]. On top of that, the unit cell of a single layer would relax with respect to the bulk and the bond length between Au and SL TaP, should also be taken into account. Therefore, here it is speculated that the measured step height of $a.h. = (0.39 \pm 0.01)$ nm corresponds to a SL TaP belonging to the space group symmetry $I4_1md$ presented in Sec. 5.1, whose unit cell is comprised of a layer of phosphorous sandwiched between two adjacent Ta planes characterized by a squared arrangement of the atomic sublattice. This phase will be named T-phase thereon.

The atomic resolution of the nanoislands presented in Fig. 5.5(b)–Fig. 5.5(d) is characterized, indeed, by an atomically resolved square lattice, marked by blue circles in Fig. 5.5(c). This coincides with the square sublattice presented in Sec. 5.1, confirming the presence of SL TaP of the T-phase. Low-bias filled-state tunnelling conditions were needed to possibly probe the atomic resolution of the square lattice. The FT analysis of several islands, as the one shown in the inset in Fig. 5.5(c) with reciprocal lattice vectors $\mathbf{a}^*_{T-STM,1}$ and $\mathbf{a}^*_{T-STM,2}$ with identical modulus, results in the lattice constant $a_{T-STM} = (0.34 \pm 0.01)$ nm which is highlighted in Fig. 5.5(c). The islands are found to be arranged on top of the substrate in three different domains rotated 30° with respect to each other. A simple rotation of 30° and 60° of the blue arrow aligned with the lattice in *domain I* in Fig. 5.5(c) proves that the three domains are rotated of 30° between themselves. The surface of the islands is often characterized by Ta vacancies, like the one shown in Fig. 5.5(c) that were ascertained to move at room temperature around the surface of the island, merging and splitting again. Similar Ta vacancies were also observed in the bulk TaP and associated to an anionic pnictide deficiency [211]. The island scanned in Fig. 5.5(d) shows a rather ill-defined edges dipped in a continuum. A possible explanation for such a shape is that the growth process was quenched by cooling the sample which, in other cases,

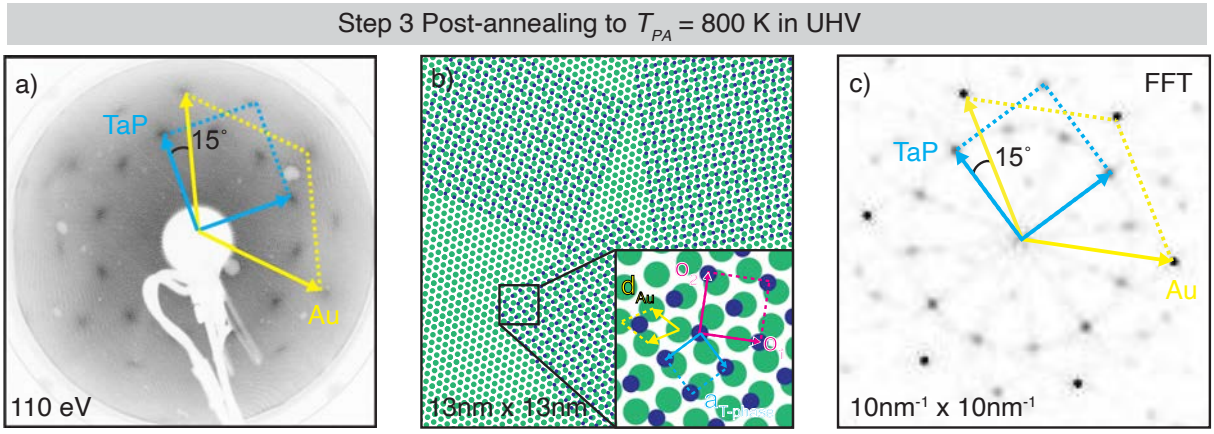

Figure 5.6: (a) LEED of the sample scanned in Fig. 5.5. The blue reciprocal vectors delimit the square BZ related to the square lattice of SL T-phase TaP which is rotated 15° with respect to the yellow hexagonal BZ of Au(111). (b) Ball model (top view) of three domains of the square lattice (deep purple) rotated of 30° with respect to each other and tilted 15° with respect to the hexagonal lattice underneath. The inset shows a square non-primitive unit cell of T-phase of SL TaP with lattice parameters $\mathbf{o}_1$ and $\mathbf{o}_2$. (c) FT of the ball model in panel (b). The blue and yellow BZ are taken from panel (a), enlarged and rotated to prove the correspondence between the FT related to the ball model and the LEED pattern.

shows a more compact structure.

At first glance the lattice constant of Au(111) $a_{Au} = (0.28 \pm 0.01)$ nm [200] is quite different from the STM measured lattice constants of the SL T-phase TaP $a_{T-STM} = (0.34 \pm 0.01)$ nm, so no epitaxial growth of TaP is expected unless other ways to match the lattices are taken into account. In effect, the ratio between second nearest neighbours in Au(111) and second nearest neighbours of the Ta sublattices $\sqrt{3}a_{Au}/\sqrt{2}a_{T-bulk} = 1.037$ (with $a_{T-bulk} = 0.332$ nm [23]), meaning that an elongation of $\approx$ 3.7% would be needed to adapt the SL T-phase TaP square lattice to the Au(111) hexagonal one [3]. According to this interpretation the atomic lattice constant of SL T-phase TaP would be $a_{T-phase} = 0.344$ nm, which is in agreement with $a_{T-STM} = (0.34 \pm 0.01)$ nm. Moreover, this value is relatively close the lattice constant derived by the reciprocal lattice labelled in blue on LEED image in Fig. 5.6(a) of $a_{T-LEED} \approx 0.33$ nm [4].

[3] Larger values than $\approx$ 3.7% lattice mismatch were observed, e.g. heteroepitaxy of Ge on Si can take place with a 4% mismatch between Ge and Si [212].

[4] An accurate estimate of the uncertainty given to this value should take into account aberration of the camera lenses and tilt of the camera used to capture the LEED patterns or inclination of the sample surface in the UHV chamber [213], which were not considered in this experiment. The Au(111) diffraction spots were taken as a reference to determine a_{T-LEED} [214]

Similar examples of STM and LEED of hexagonal layers on top of square lattice, like FeO(111) on Pt(100) [215], or square layers on top of hexagonal lattice, like epitaxial FeTe thin films on Bi_2Te_3 [192, 80], can be traced in the literature. In the first case the hexagonal lattice would orientate in two possible domains orthogonal to each other, in the latter one the square lattice of FeSe orientates in three different domains rotated 30° with respect to each other. In fact, from the LEED and STM it is clear that FeTe thin films on Bi_2Te_3 shares the same orientation of SL T-phase TaP on Au(111), but in FeTe the square lattice is incommensurate with respect to Bi_2Te_3 leading to a 1D Moiré superstructure. Instead, no hint of Moiré superstructure could be recorded with LEED and STM for SL T-phase TaP on Au(111). In order to better understand the nature of the commensurability between the two lattices a ball model of the square TaP lattice (deep purple) with lattice constant $a_{T-phase}$ on top of the Au(111) hexagonal lattice (green) with lattice constant a_{Au} is shown in Fig. 5.6(b). The inset of Fig. 5.6(b) shows a close-up of the model where a composite unit cell ($\mathbf{o_1}$, $\mathbf{o_2}$) of the square lattice is considered alongside $a_{T-phase}$ and a_{Au}. It is possible to see that the square lattice is commensurate with respect to the hexagonal lattice only along $\mathbf{o_1}$, while no commensurability could be assessed along $\mathbf{o_2}$.

In order to compare the ball model in Fig. 5.6(b) with the LEED pattern in Fig. 5.6(a), three-fold rotational domains of the square lattice rotated 15° with respect to the Au(111) are introduced, and a FT of the image is performed and displayed in Fig. 5.6(c). The reciprocal vectors of Fig. 5.6(c) are just rotated and proportionally scaled from those in Fig. 5.6(a) to prove that the LEED pattern arises from the three-fold rotational domains of the square lattice rotated 15° with respect to the Au(111) substrate.

5.5.2 H-phase of SL TaP and p(2×2) superstructure

In order to explore the effect of post-annealing temperature on the sample morphology, a post-annealing step at a higher $T_{PA} = 1000$ K of 20 min was performed on a sample with $t_{Ta} = 180$ sec in the first step and $T = 900$ K for 20 min in PH_3 atmosphere at $p = 2 \times 10^{-7}$ mbar in the second step. Afterwords STM imaging and XPS were acquired as shown in Fig. 5.7(a)–(c). Some differences were found with respect to the sample presented in the previous section: a reduced amount of small mobile irregular clusters populated the surface and more frequently they would be located on the corners of triangularly shaped holes, as shown seen in the STM

in Fig. 5.7(a). The holes thickness was measured to be $a.h. = (0.14 \pm 0.01)$ nm, as shown by the green line profile in the inset of Fig. 5.7(b), meaning that only one layer of the P-amorphous phase is left after the high temperature post-annealing procedure. This time not only the square lattice of the T-phase TaP in Fig. 5.7(a) was atomically resolved by STM (not shown here), but also the Au lattice underneath the amorphous phase could be observed down to the atomic scale in Fig. 5.7(b). This made possible to further demonstrate that the direction of the T-phase of SL TaP is rotated 15° with respect to the one of the Au(111) hexagonal arrangement of atomic lattice.

The STM in Fig. 5.7(b) shows another new component which is a triangular protrusion with height of $a.h. \approx 0.22$ nm, as seen in the inset in Fig. 5.7(b), characterized by an hexagonal arrangement of atomic lattice with a lattice constant of $a_{H-STM} \approx 0.3$ nm. Unfortunately, atomic resolution could not be achieved on other similar islands, hence more statistics is needed to assign proper values of the atomic lattice constant. Moreover, bright brims in the atomic rows adjacent to the outermost edge protrusions of the triangular islands were observed. Similar protrusions were studied in semiconducting transition metal dichalcogenides as one-dimensional metallic edge states effect [216, 217]. It is speculated here that a new semiconducting H-phase of a SL TaP compound, coming from an hexagonal crystal family, could be the component of these triangular islands. As a matter of facts, no bulk counterpart with an hexagonal crystal family has been characterized among TaP compounds yet [218, 219]. Such a novel phase seems to be stable at the 2D limit on a Au(111), though.

Fig. 5.7(c) shows XPS spectra of the Ta 4f core levels that were acquired at $h\nu = 140$ eV on the sample shown in Fig. 5.7(a) and (b) and on the bulk TaP (space group symmetry $I4_1md$) grown according to the procedure in Ref. [220] by co-workers from the Chemistry Department at Aarhus University, Denmark. By a qualitative analysis of the spectra it is visible that the Ta 4f core level doublet of the bulk (purple), caused by the $\pm 1/2$ spin component, is matching that of SL compounds (blue) at photon energies of $E_b \approx 22.8$ eV and $E_b \approx 24.7$ eV (light blue arrows) indicating the presence of a similar phase on the substrate. Similar peak energies (22.9 eV and 24.8 eV) were also observed after the furnace reaction of bulk Ta cartridges with PH_3 gas [195]. As the SL T-phase TaP shares the same symmetry of the TaP bulk, this doublet is assigned to the T-phase of TaP. Moreover, two additional peaks are found at $E_b \approx 23.8$ eV and $E_b \approx 25.7$ eV on the SL spectrum (very light blue arrows). These are still attributed to the Ta 4f core level

doublet but shifted of 1 eV to higher E_b. The two additional peaks from the SL TaP compounds cannot be attributed to metallic Ta which is expected to show a peak at lower E_b (21.6 eV) [195], meaning that no unreacted Ta was present at the surface. In this case they could be attributed to a higher oxidation state of Ta, e.g., similarly to the shift in binding energy observed on the ta 4f peak from TaS and TaS_2 but at different binding energies [221]. Therefore, it is speculated here that these two peaks are referred to the H-phase of SL TaP ad it points toward a different P-rich stoichiometric ratio between Ta and P. Diffraction techniques like grazing-incidence X-ray diffraction could help in understanding the stoichiometry of this TaP compound once it will be singled out with higher coverages at the surface [211].

Another possible reaction that could possibly take place at the surface is the hydrogenation of Ta to form TaH_x. This would open up the possibility that the SL compounds belong to the disordered phase α-TaH, which is the only phase among TaH compounds stable at room temperature [222, 223]. In such a structure the atomic hydrogen randomly occupies the tetrahedral sites of the $Im\bar{3}m$ space group of Ta that is a body-centred-cubic (BCC) structure. According to the hydrogen content the lattice constant was observed to vary between 0.3306 nm and 0.3405 nm. Even though the lattice parameters could reasonably match with that of the presented T-phase of TaP, desorption of hydrogen has been reported to occur at high temperatures [224, 225]. Nevertheless, other studies showed that hydrogen was not taken up from metallic Ta at temperatures of 1000 K and pressures 8×10^{-2} mbar [226]. This would lead to the conclusion that no hydrogen is left from the post-annealing procedure at 1000 K.

Until this point, a post-annealing in UHV at $T_{PA} = 800K$ for 20 min was adopted resulting in the desorption of elemental phosphorous compounds, as shown in Figs. 5.5 and 5.6, and a post-annealing in UHV at $T_{PA} = 1000K$ for 20 min was performed producing a SL H-phase TaP compound, as seen in Fig. 5.7(a)–(c). In order to further test the role of post-annealing on the composition and morphology of the overgrowth the post-annealing duration was drastically reduced by simply letting the sample cooling down in UHV from $T_{PA} = 1000K$ to room temperature at the end of step 2 of the growth (without changing the other growth parameters). Under these conditions yet a new phase can be spotted by means of STM and LEED in Fig. 5.7(d)–(g), while the other phases are still found at the surface.

The STM topographic image in Fig. 5.7(d) shows an overview of the overgrowth, where T-

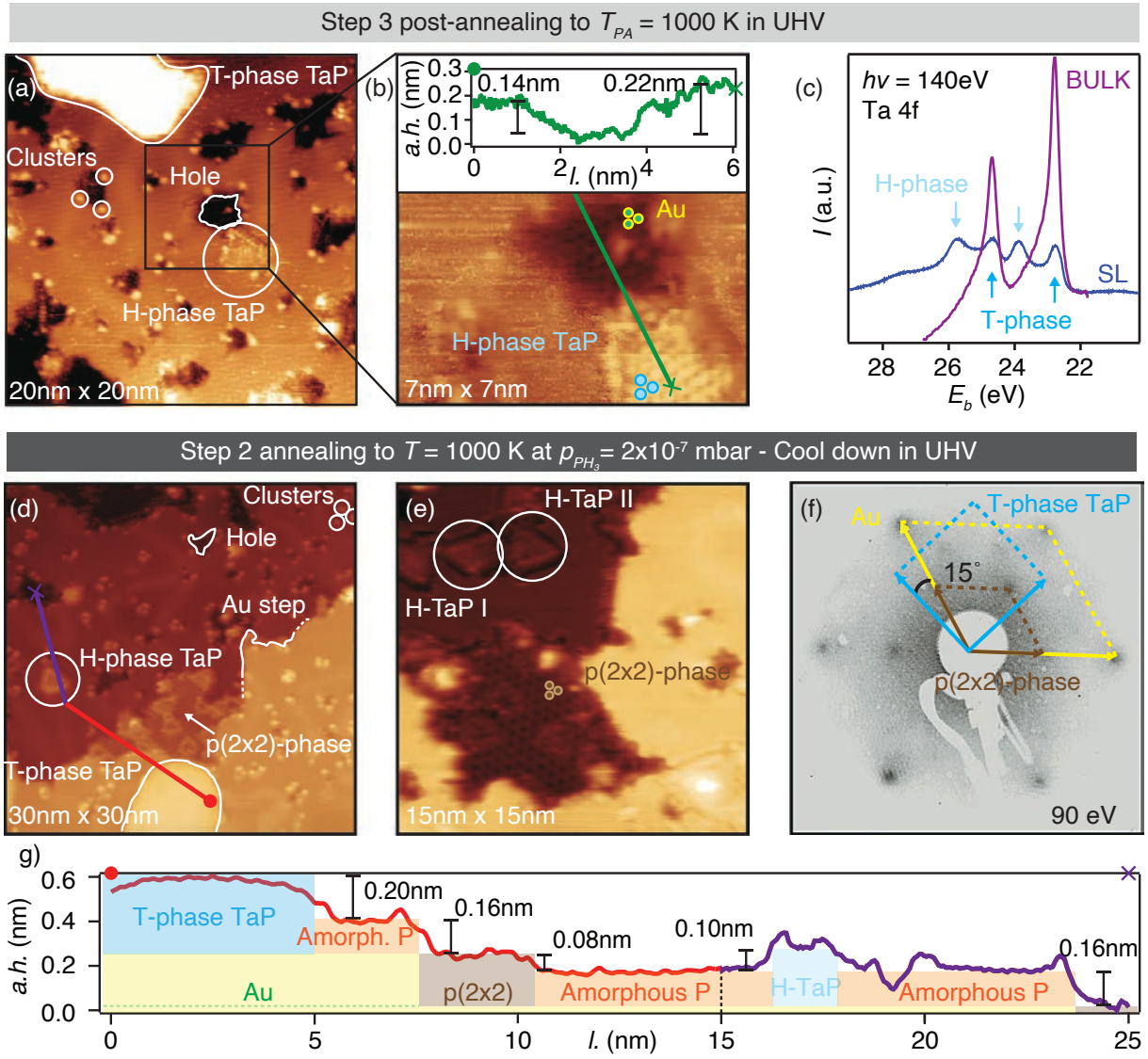

Figure 5.7: (a)–(c) STM and XPS of a sample post-annealed at T_{PA} = 1000 K after a two-step growth described in the text. (a) STM topographic image (V_b = 0.05 V, I_t = 0.35 nA and Δh = 0.5 nm) showing T- and H-phase of TaP, holes and clusters. (b) STM close-up image from panel (a) (V_b = -0.006 V, I_t = 0.37 nA and Δh = 0.3 nm). The H-phase TaP and Au lattice are marked by blue and yellow-green circles, respectively. The line profile in green is reported in the inset. (c) Ta 4f core levels for the bulk (purple) and SL (blue) TaP compounds (hν = 140 eV). The two spin-split doublets described in the text are labelled in the figure. (d)–(f) STM and LEED images of a sample annealed at 1000 K during the second step and cooled down in UHV, as described in the text. (d) STM image (V_b = 0.007 V, I_t = 0.29 nA and Δh = 0.8 nm) where holes, T- and H-phase of TaP and the p(2×2)-phase are marked. (e) STM image (V_b = 0.008 V, I_t = 0.26 nA and Δh = 0.35 nm) with two H-phase domains of TaP and the p(2×2)-phase labelled. (f) LEED image where Au, T-phase TaP and p(2×2)-phase related reciprocal vectors are marked in yellow, light blue and purple, respectively. (g) Red-purple *V-shaped* line profile taken from (a). The hypothetical components of the overgrowth are shown in different colours.

phase and H-phase of SL TaP, holes and clusters are visible and form a very similar morphology to the one shown in the overview in Fig. 5.7(a). In addition, a new hexagonal structure is found in the proximity of Au steps or on the surface of the holes, whose periodicity of the lattice does match neither with H-phase TaP nor with Au(111) lattice. From Fig. 5.7(e), and similar images, the STM extrapolated lattice constant is $a_{2x2-STM} = (0.52 \pm 0.01)$ nm, which does not quite match the value of $a_{2x2-LEED} \approx (0.56)$ nm estimated from the LEED diffraction spots marked by the brown BZ in Fig. 5.7(f). However, the difference of 8% between these two values could be traced back to a systematic error either in the determination of $a_{2x2-STM}$ or $a_{2x2-LEED}$. From a comparison of the crystal lattices in the STM images in Fig. 5.7(b) and (e) and from the LEED image in Fig. 5.7(f), it is clear that the Au(111) and the new hexagonal lattice share the same crystal orientation, but the proportion of the respective lattice constants is $a_{2x2}/a_{Au} = 2$, meaning that the latter one is characterize by a p(2×2) superstructure with respect to Au(111) lattice. A similar superstructure was found by STM and LEED for the polar (111) surface of NiO on Au(111) [227], alluding that such an arrangement of the atomic lattice could be constituted by P or TaP, without excluding the possibility or a p(2×2) reconstruction of the Au(111) surface. The study of the spectroscopic signature of this phase by means of XPS, similarly to Fig. 5.7(c), could help to the determine its composition of this phase in the future research.

In Fig. 5.7(d) and (e) the triangular islands present either an upward or downward orientation. These could possibly arise from two different domains of the H-phase of SL TaP rotated 60° with respect to each other. Such domains tend to aggregate in the proximity of the p(2×2) phase, as seen in Fig. 5.7(d). In order to comprehend the complex morphology of the overgrowth, a *V-shaped* red-purple line profile is taken in Fig. 5.7(d) through the p(2×2) phase as well as other phases and reported in Fig. 5.7(g). A hypothetical model of the overgrowth vertical structure that matches the line profile is overlapped in Fig. 5.7(g) in order to facilitate the comprehension of the several phases at the surface. According to this interpretation, T-phase and H-phase SL TaP, p(2×2) superstructure and SL amorphous P are believed to nucleate and grow on top of the Au(111) surface. Furthermore, p(2×2) superstructure typically grows on the step edges of Au(111), whereas the amorphous P uniformly covers the Au(111) surface adapting to the lifted-herringbone reconstruction that is still visible in Fig. 5.7(d).

The many growth strategies introduced until now resulted in the growth of several single layer crystal structures at the surface uncovering the rich chemistry between Ta and P. Never-

theless, it would be desirable to aim for chemical selectively by being able to grow and study the structural properties of a single phase at high coverages. In the next Section a new strategy is adopted in this regard.

5.6 c(2×4) reconstruction of Au(110) and formation of Au-P chains

As the chemical composition of the Ta-based compounds was swapped from sulphur in Chap. 3 to phosphorous in this Chapter, it is relevant at this point to test the outcome of the growth by keeping the same elements in the compound (TaP) while changing the substrate. It has been shown, for example, that the low-index crystal surfaces Au(111) and Au(110) exhibit different adsorption energies [228, 229], catalytic activities [230] and, in particular, they offer different templates for the epitaxial growth of 2D materials [231] with considerable effects on the yield and morphology of the growth [232].

The clean Au(110) surface, in fact, is characterized by a thermodynamically stable (1×2) *missing-row* reconstruction in UHV in relation to the bulk (1×1) structure, which is very different from the herringbone reconstruction of the closely-packed hexagonal arrangement of the atoms in Au(111) [233, 234]. The disposition of the atoms at the Au(110) surface is such that every second atomic row along the $[0\,0\,1]$ direction is missing, giving rise to a rectangular unit cell whose parameters are $a_{Au110,1} = a_{Au,bulk} = 0.288$ nm and $a_{Au110,2} = 0.816$ nm [235, 236]. The anisotropic nature of Au(110) granted the possibility to our group at Aarhus University to grow $V_{1+x}S_2$, both as 1T-phase and as a striped structure-phase [237]. In this Section the substrate Au(110) was adopted with the purpose of assisting the growth and characterization of T-phase SL TaP square lattice. Surprisingly, the reaction at the surface resulted in the unprecedented phosphorous driven reconstruction of the Au(110) substrate in a c(2×4) structure with respect to the bulk (1×1) structure and in the formation of novel AuP-chains along the $[1\,\bar{1}\,0]$ direction.

Au(110) has been thoroughly cleaned by repeated cycles of sputtering at 1.2 keV with Ar^+ gas at a pressure of 5×10^{-6} mbar followed by 1 hour annealing at $T = 750$ K until the surface locally exhibited the regular missing-row reconstruction with low contaminant concentration assessed by STM. In fact, some contaminants were observed to dislocate the missing-row recon-

struction perturbing the periodicity of the crystal in several $(1 \times n)$ reconstructions (with n being an integer number) which could affect the result of the epitaxial growth [237]. The annealing temperature and the cooling rate can have also an affect on the $(1 \times n)$ periodicity of the reconstruction [236, 238]. Even though the missing-row reconstruction was clearly visible by STM in this experiment, the atomic resolution of Au(110) surface was never reached. Nevertheless, the equidistant rows divided by darker regions along $[1\,\bar{1}\,0]$, like the ones seen in Fig. 5.8(a), allow the determination of $a_{Au110-STM,2}$, which is calibrated to match the one obtained from the analysis of the LEED diffraction spots of clean Au(110) of $a_{Au110-LEED,2} = (0.80 \pm 0.01)$ nm (not shown here). In this way the measure of the length performed on STM images can be calibrated to match $a_{Au110,2}$. Furthermore, as Au(110) atomic steps are clearly spotted in Fig. 5.8(a), it is possible to calibrate the measured apparent height, $a.h. = (0.11 \pm 0.01)$ nm, by comparison to a reference value of $a.h. = (0.14 \pm 0.01)$ nm [239] that coincides with the Au interplanar distance $a_{Au,bulk}/2 = 0.144$ nm.

The sample presented in the current section was prepared by a two-step 6 cycles growth where in the first step Ta deposition occurred at $F = 4.35 \times 10^{16}$ atoms $\mathrm{m}^{-2}\mathrm{s}^{-1}$ for 120 sec and in the second step the sample was heated up to $T = 750$ K for 20 min after PH_3 gas was leaked into PC1 at $p = 2.5{\times}10^{-7}$ mbar. The cooling of the second step took place in UHV conditions. A final post-annealing at $T = 900$ K was carried out. In Sec. 5.3, Ta was found to assist the cracking of PH_3 at high temperatures. In fact, when Au(110) is exposed to the above mentioned growth procedure, but without Ta, no significant changes were spotted at the surface (not shown here), while the addition of Ta brought new products at the surface. The presence of Ta and P on the surface after the reaction was verified by XPS analysis (not shown here) that exhibited Ta 4f and P 2p corelevels. The result of the reaction according to the growth procedure described above is presented in Fig. 5.8.

Fig. 5.8(a) gives an overview of the outcome of the growth on the Au(110) surface. First of all, large domains of a new *distorted-checkerboard* structure are found at the surface, as later confirmed by the analysis of the LEED pattern. The area of such domains extends up to $A \approx 100$ nm^2 and the surface is covered up to $\theta \approx 0.3$ ML. A larger caterpillar-shaped stripe structure can be also found on the surface with $\theta \approx 0.02$ ML. Such a structure can be even 40 nm long and it can form clusters of up to 4 stripes, as shown in Fig. 5.8(c). Finally, clusters of an average lateral size of $l. \approx 3$ nm are found at the surface, typically close or within the

distorted-checkerboard structure domains.

The distorted-checkerboard structure shown in Fig. 5.8(b) does not necessarily represent a new compound at the surface. Different reconstructions were proven to occur upon dosage of molecules like glycine [240], pentacene [241] or acetate [239] on Au(110). In particular a long-range displacive c(2×4) reconstruction of Au(110) [5] was driven by low coverage of sulphur molecules [242]. The spatial distribution of the LDOS imaged by STM of the c(2×4) sulphur driven reconstruction is very similar to the one observed in Fig. 5.8(b), and the possible presence of sulphur contaminants is excluded as relatively high coverage of S adatoms is require to form such structure, as it will be later explained. A careful inspection of Fig. 5.8(b) and (e) would show that both for the sulphur driven c(2×4) reconstruction and the distorted-checkerboard structure the bright spots are connected by faint lines of intensity along the diagonals of the checkerboard, but not along the horizontal directions. According to the model in Fig. 5.8(e) taken from Ref. [242], these faint lines are related to lines of coplanar Au atoms (green) that are diagonally, but not horizontally, contiguous. In fact such Au atoms are positioned in the topmost position and therefore are expected to influence the LDOS at the surface. Furthermore, the experimentally determined unit cell parameters match the values calculated in Ref. [242]. These were measured and labelled by the purple arrows in the FT image shown in Fig. 5.8(g) related to the STM in Fig. 5.8(b) and result in $|\mathbf{a}_{2\times4-STM,1}| = (1.15 \pm 0.01)$ nm and $|\mathbf{a}_{2\times4-STM,2}| = (0.80 \pm 0.01)$ nm, which roughly correspond to four times the periodicity of the underlying Au(110) (1×1) surface along $[1\,\bar{1}\,0]$ and two times along $[0\,0\,1]$, respectively. The line profile in Fig. 5.8(d) shows that the apparent height of the distorted-checkerboard reconstruction with respect to the missing-row one matches the Au (1×2) step height of 0.14 nm, confirming that the c(2×4) reconstruction can be characterized by monoatomic Au steps with adjacent domains. Furthermore, the FT image in Fig. 5.8(g) shows a feature, defined by the yellow reciprocal lattice vector, of the same periodicity of the missing-row reconstruction along $[0\,0\,1]$ that further proves the alignment of the c(2×4) reconstruction with the (1×2) one.

The DFT-based search performed in Ref. [242] among energetically competitive candidates structures for the as observed c(2×4) reconstruction required a coverage of $\theta = 0.25$ ML to obtain the model presented in Fig. 5.8(e), suggesting that a similar coverage of P was accomplished in the current experiment. The stability of the distorted-checkerboard reconstruction

[5] A displacive reconstruction is a reconstruction where the density of Au adatoms is conserved.

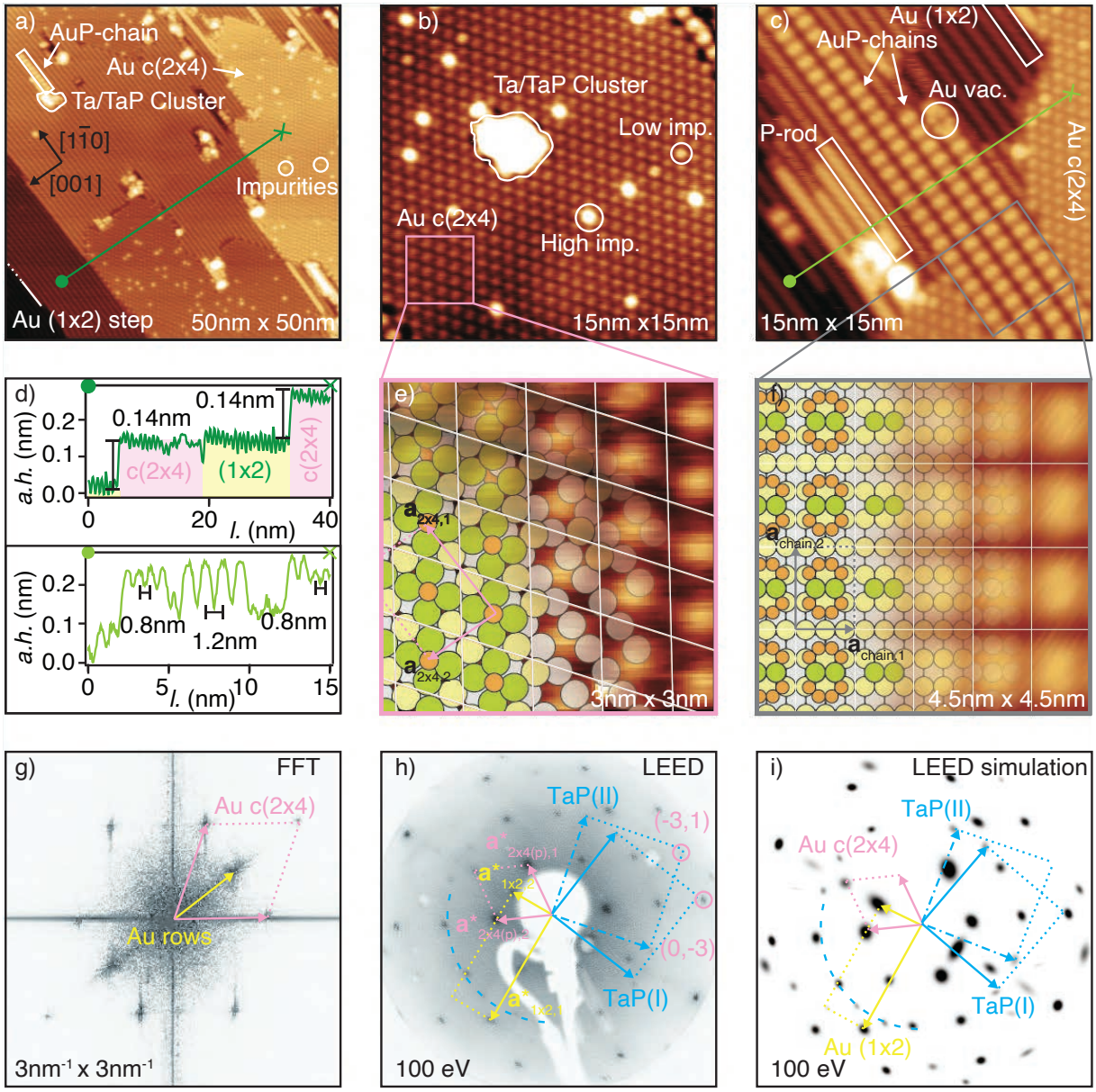

Figure 5.8: STM and LEED of Au c(2×4) reconstruction and Au-P chains on a Au(110) substrate. (a) STM topographic image ($V_b = 1.25$ V, $I_t = 0.21$ nA and $\Delta h = 0.7$ nm) showing the c(2×4) reconstruction, AuP-chains, Ta clusters and impurities on (1×2) reconstruction of Au(110). (b) STM image of Au c(2×4) ($V_b = 1.25$ V, $I_t = 0.20$ nA and $\Delta h = 0.1$ nm). The high and low profile impurities as well as the larger cluster are marked in the figure. (c) STM image ($V_b = 1.25$ V, $I_t = 0.2$ nA and $\Delta h = 0.3$ nm) showing the AuP-chains, Au c(2×4) reconstruction, the phosphorous rows and a Au vacancy within the AuP-chain. (d) dark and light green line profiles extracted from panel (a) and (c), respectively. (e) and (f) are STM close-up of (b) and (c), respectively, with ball models superimposed where the grey, yellow and green circles represent the stacking of three adjacent planes of coplanar Au atoms, while the orange circles represent P atoms. (g) FT of panel (b). The reciprocal lattice vectors are drawn in the panel. (h) LEED image of the sample with reciprocal lattice vectors for the different reconstructions at the surface and for the two TaP domains. (i) Simulation of the LEED pattern in (h).

was demonstrated to be partly granted by the presence of *pseudo-4-hollow sites* (p4hs) for sulphur adsorption, represented by the green upmost coplanar Au atoms in Fig. 5.8(e). On top of that, the STM simulated intensity was proven to ideally match the STM images performed on the reconstruction. Clearly, similar DFT-energy based arguments and STM simulation should be also perform in the future with P instead of S to prove the match between the model and the STM data. Nevertheless, the actual model presents a very strong guess based on the results obtained in Ref. [242].

Some impurities are found on top of the c(2×4) reconstruction that were immobile at room temperature. These exhibit either a high ($a.h. = 0.10 \pm 0.01$) nm or a low ($a.h. = 0.03 \pm 0.01$) nm apparent height profile. Such defects were not observed in the nearly-perfect domains reported in Ref. [242], and could be due to the presence of different adatoms on top of the p4hs. A reasonable guess could be that the *high impurities* correspond to the presence of a Au atom, while the low impurities correspond to the presence of P_2 instead of P on the p4hs. In fact, the c(2×4) reconstruction is characterized by a corrugation of $a.h. = 0.05 \pm 0.01$ nm which could correspond to the difference between the phosphorous (orange) and the topmost Au layer (green) in Fig. 5.8(e), while the Au interplanar distance is $a_{Au,bulk}/2 = 0.144$ nm, meaning that the difference between the two matches with the profile of the high impurity which could, therefore, be explained by the substitution of the P atom with a Au atom. The *low impurities*, instead, could arise as a consequence of the different LDOS due to the presence of an extra P atom, however greater resolution should be obtained and comparison with DFT simulation of the STM intensity should be carried for different models and XPS for different impurity concentration should be carried out in order to safely assess this guess. The bigger cluster at the center of the domain in Fig. 5.8(b), is attributed to Ta or TaP compounds. In fact, as previously pointed out, Ta is present at the surface and no other structure than the clusters was found to be a potential candidate for Ta, as all other structures were already assigned by the local STM analysis presented here. These Ta/TaP clusters could play a pivotal role for cracking PH_3 at the surface, as it will be later explained.

Atoms at the extremity of some *rods* were highly mobile with respect to those at the end of the missing-row reconstruction of Au(110). Moreover, sulphur was previously observed to be chemisorbed on the *pseudo-3-hollow-sites* established by two Au atoms in the top row, and one Au atom on the side of the facet within the empty rows of the (1×2) reconstruction, forming

long rods along $[1\,\bar{1}\,0]$. These are indications of the fact that either P or Ta should be the element forming such rods, as the ones seen in Fig. 5.8(c). Moreover, as these were always observed to diffuse in the proximity of the distorted-checkerboard reconstruction and of Ta clusters, here it is hypothesized that they are actually comprised of elemental P that was obtained by Ta cracking of PH_3 and chemisorbed within the rows in form of P-rods. These then drive the c(2×4) rearrangement of the Au(110) atomic lattice upon heating. Atomic resolution of the P-rod and of the Ta/TaP clusters should be found in order to further elucidate the nature of the reaction.

The unit cell of the caterpillar-shaped stripe structure was determined by FT analysis of Fig. 5.8(c) (not shown here) and compared to $a_{Au110,1}$ and $a_{Au110,2}$ resulting in a (3×3) supercell of Au(110), where $|\mathbf{a}_{chain-STM,1}| = (0.88 \pm 0.01)$ nm and $|\mathbf{a}_{chain-STM,2}| = (1.23 \pm 0.01)$ nm roughly correspond to three times the periodicity of the underlying Au(110) (1×1) surface along $[1\,\bar{1}\,0]$ and $[0\,0\,1]$, respectively. The lattice parameters can be also compared to the Au rows and P-rods by means of an apparent height profile shown in light green in Fig. 5.8(d) where the larger periodicity is clearly displayed. It is speculated here that these structures correspond to one-dimensional metal-inorganic AuP chains composed by Au_2P_8 units, as shown in Fig. 5.8(f). According to this interpretation, the Au_2P_8 units are located at the center of the unit cell drawn in Fig. 5.8(f) on top of a un-reconstructed Au(1x1) surface. In order to prove this model, a selective screening of the FT spots related to Fig. 5.8(c) is carried out and the real 2D intensity resulting from the inverse FT is considered. From this analysis it is possible to assess a high LDOS at the center, and even higher at the two shorter sizes of the unit cell, which is periodic along the AuP-chain. This is could be a confirmation of the presence of Au and P_4 clusters at the center and at the sides of the unit cell, respectively, the latter generating a higher LDOS in agreement with the similar structure observed in Ref. [243]. The circle in Fig. 5.8(c) marks a lower LDOS region at the center of a unit cell which is accompanied by an increase of the LDOS outside the shorter edges of the unit cell. According to the model described, the lack of LDOS could be explained taking into account a Au vacancy caused by the dislocation of the two Au atoms with the P_4 clusters to the two adjacent Au rows implying a consequent redistribution of LDOS. Such a Au vacancy was observed to move along the chain at room temperature.

A LEED image with several features is displayed in Fig. 5.8(h). Because of the complexity of the LEED image I personally developed a fitting procedure to fit each LEED diffraction spot with a two-dimensional Gaussian profile, as shown in the simulation pattern presented in

Fig. 5.8(i). The LEED fit was performed with a sufficiently small region to consider the background as constant and by constraining the amplitude, with and covariance of the 2D Gaussian profiles based on physically meaningful assumptions. Besides, the real space Bravais lattice was derived from the calculated reciprocal space vectors (not shown here). In addition to the diffraction spots related to the (1×2) (yellow) and c(2×4) (pink) reconstructions, that match the geometry of the FT in Fig. 5.8(g), the LEED pattern reveals a circular feature of radius $\approx 2|\mathbf{a}^*_{2\times4(p),1}|$, i.e. two times the reciprocal vector of the BZ related to the primitive unit cell of the c(2×4) reconstruction. Furthermore some more intense diffraction spots appear along the circumference of the feature. The radius of the circles is converted to a lattice parameter of $a_{T-LEED} \approx 0.33$ nm, which matches very well with the Ta–Ta interatomic distances of T-phase of SL TaP measured by LEED in Sec. 5.5.1. By drawing the unit cell of TaP in a similar way of Fig. 5.6(a) two TaP domains emerge with their (1,1) reciprocal lattice point roughly corresponding to the (0,$\bar{3}$) (domain I in the panel) and ($\bar{3}$,1) lattice point of the c(2×4) reconstruction labelled in pink. Furthermore, the circular feature indicates the presence of azimuthally disoriented TaP domains on the surface. Nevertheless, more evidence is required and, as mentioned above, atomic resolution of the clusters should be achieved in order to properly compare the LEED and the STM results. A comparison of the FT pattern obtained from Fig. 5.8(c) (not shown here) and the LEED in Fig. 5.8(h) shows no evidence of the AuP-chains signature on the LEED which should be found along the (1×2) reciprocal lattice directions. The lack of such signature is probably determined by the very low coverage of PAu-chains. A selective growth of this metal-inorganic chain could allow to obtain higher coverages and to determine its diffraction pattern.

The results presented so far showed a new viable way to the epitaxial growth of SL TaP compounds and blue phosphorene as well as other surface structures, such as the c(2×4) reconstruction of Au(110) triggered by deposition of phosphorous. The wide spectrum of possible outcomes of the reaction between Ta and P on low-index Au surfaces discussed in this chapter constitutes an ideal platform to further explore the growth procedure in order to obtain a improved selectivity toward the production of a single phase which would allow to study the electronic structure of the material on a macroscopic level. As pointed out at the beginning, single layer materials like TaP compounds and blue phosphorene could, one day, have great impact in the production clean energy and this work traces a first step in this yet unexplored direction.

Chapter 6

Conclusions and outlook

This chapter provides a summary of the most relevant results presented in this thesis and shows reflections on possible future research work to be done starting from the results obtained.

6.1 Summary

The results of the work presented in this thesis can be divided according to the growth and characterization of 2D TaS_2 and SL TaP compounds. In the first case the electronic properties were analysed by means of tr-ARPES, while in the second one the research was more focused on the structural characterization of the material by means of STM and LEED. The main results obtained by the investigation of these materials are summarized here:

Chapter 3. Electron dynamics in a 2D metal: tr-ARPES of TaS_2 on graphene - A 2D metallic TaS_2 was successfully grown in the 2H polymorph on graphene, this is mainly comprised of a SL or BL structure. The electronic structure of this material was widely studied by means of static and tr-ARPES experiment. The considerable changes of the occupied bandwidth and strong variation of the electron gas temperature were recorded in subsequent snapshots of the photoemitted intensity that composed an *ultrafast movie* of the valence band dynamic response to the probe pulses. The photoemission data were analysed quantitatively thanks to a novel 2D fitting scheme describing the entire resolution- and energy-broadened time-dependent photoemission intensity. The extrapolated electronic temperature dependent band shifts were theoretically framed by considering the chemical potential shift as well as the temperature-dependent

many-body screening effect, showing good agreement with the data.

Chapter 4. Hot carrier relaxation in 2D TaS_2 - A three-temperature model system of differential coupled equation is taken into account to describe the energy dissipation of the 2D electron gas to the lattice. It was demonstrated that the ultrafast dynamics in TaS_2 are well described by an energy exchange with the sc photons which later release their energy to the rest of the lattice. Intriguingly, the electron-phonon coupling strength, as well as the several characteristic time constants that describe the phonon relaxation, depend on the experimental pump fluence applied to the sample. It was speculated that the fluence-dependent electron-phonon coupling strength is motivated by the drastic changes in the screening induced by the wide range of the electronic temperatures probed in this experiment.

Chapter 5. Single layer tantalum phosphide compounds - It was demonstrated how Ta and P actively take part to the reaction involved on the Au(111) and Au(110) surface, bringing several new single layer phases and triggering the reconstruction of the Au(110) surface. In particular TaP compounds were grown and their yield was seen to be sensitive to the growth parameters, in particular showing an increase in coverage with t_{Ta}, whereas the recently discovered allotrope of phosphorous, BlueP, experienced a high coverage for low t_{Ta}. Two different phases of TaP were ascertained at the surface, namely T- and H- phase SL TaP compounds, whose structural analysis was carried out by means of STM and LEED. Finally, a c(2×4) reconstruction was observed taking place on Au(110) induced by the deposition of phosphorous. Such a reconstruction was accompanied by AuP-chains, whose model structure was presented here for the first time.

6.2 Outlook

The very large band shifts in a pumped 2D metallic systems, like 2D TaS_2, could potentially allow to create unconventional states of matter. The transient temperature-induced shift could be used, for example, to push a Van Hove singularity in the density of state close to the chemical potential, possibly inducing electronic instabilities at high temperatures [77]. Moreover, the study of the modification of 1-H TaS_2 CDW order with a laser pump-probe pulse scheme could bring light to the complex intertwined role between ordering mechanisms and collec-

tive effects. Such an intriguing phenomenon could be accessible by proper modelling of the time-resolved renormalization of the spectral function [244], which was developed in Sec. 3.5. However, the low-average typical size of the 2D TaS_2 domains and the azimuthal disorder of the crystal spoils the isotropic nature of the band structure and quenches the CDW ordering of the crystal.

Not only 2D TaS_2, but also SL TaP compounds on Au(111) and Au(110) were analysed by means of ARPES, yet without finding any new signature of the TaP crystal structures or of the Au(110) reconstructions. A pointed out in Sec. 5.1, Weyl semimetals are believed to be potential candidates to replace topologically trivial metallic catalysts. The study of the electronic properties of this novel class of materials by means of ARPES could help to predict its HER activity.

In order to be able to better comprehend the promising properties of TaS_2 and TaP 2D materials, the selectivity of the reaction at the surface has to be improved. Ideally, the reaction should occur in such a way that only one of the several compounds at the surface is left forming large, uniform and nearly-perfect domains with high control over the number of layers. Practically, such a model growth was proven to be hard to achieve, but some solutions are provided here for TaP in order to address the research to be done in the nearest future. Even though TaS_2 presents different properties from TaP, the solutions presented below are referred only to the latter, as similar solutions could be adopted also to improve the growth of 2D TaS_2.

A first path to consider is a single-step growth process where Ta and PH_3 are dosed simultaneously, like sketched in Fig. 6.1(a). For example, the formation of a sub-monolayer coverage of MoS_2 on Au(111) carried out with deposition of Mo in H_2S atmosphere prevented the presulfidisation of Mo, avoiding the formation of a Mo–Au alloy [245]. Similarly, it would be desirable to explore the effect of pre-phosphidation on Ta, as it could imply a significant impact on the result of the growth. Some attempts have been already carried out in the current project, resulting in the formation of undefined clusters at the step edges of Au(111). However the effect of tantalum deposition time on the growth has not been investigated yet, and more attempts have to be carried out in the future. Moreover, while a many-cycle growth procedure has been already tested on a Au(110) substrate, the growth on Au(111) was only carried out up to two-cycles of the two-step process presented in Fig. 5.7(d)–(g), but with a lower amount of Ta deposited during the first step, as shown in Fig. 6.1(b) and (c). This procedure resulted in a

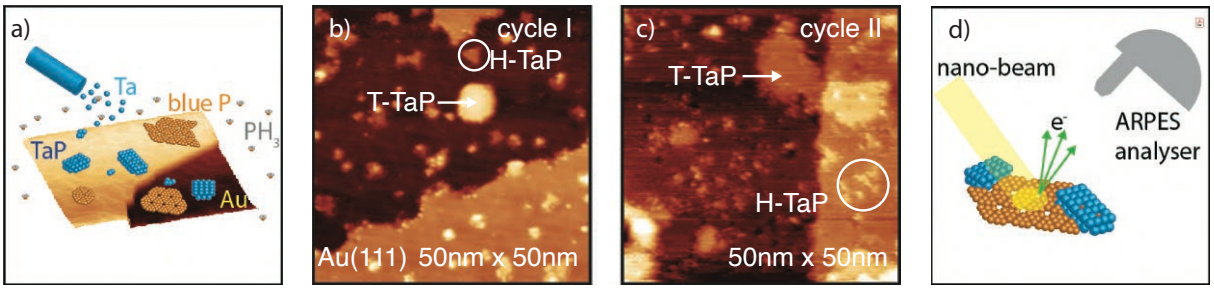

Figure 6.1: Strategies for future improvement of the growth and characterization of SL TaP compounds. (a) Model of the one-step MBE with deposition of evaporated Ta on Au(111) in PH_3 environment. (b) ($V_b = 1.87$ V, $I_t = 0.28$ nA and $\Delta h = 0.5$ nm) and (c) ($V_b = 0.23$ V, $I_t = 0.33$ nA and $\Delta h = 0.6$ nm) are STM topographic images of the two-cycles, two-step growth procedure presented in Fig. 5.7(d)–(g), with the only difference that Ta deposition time is kept to $t_{Ta} = 60sec$ for the first step of both cycles. (d) Model of the possible characterization of bigger domains (not in scale) of SL TaP and BlueP thanks to a synchrotron based nano-ARPES technique.

low coverage amount of only T- and H-phase of SL TaP compounds, with no amorphous phosphorous or p(2×2) phase present. A fine tuning and improvement of this growth procedure could be a good starting point to a selective growth of SL TaP compounds.

An experimental synthesis of different compounds of TaP could be by also assisted by a different substrate with highly-compatible lattice parameters. For example, a straightforward choice fot the growth of T-phase of SL TaP could be Ta which, with its cubic lattice constant of 0.3306 nm [223], could easily match $a_{T-phase} = 0.3334$ nm [173]. Another option could be the semiconducting Ga-terminated GaN(001), whose hexagonal arrangement of the atomic lattice exhibits a lattice constant of 0.325 nm [205] that is characterized by an unidirectional mismatch of only 1.5% with respect to $a_{T-phase} =$. Additionally, GaN(001) was predicted to be a viable substrate for the epitaxial growth of phosphorene [205] and, with its wide bandgap, could be a desirable alternative to the metallic Au(111), as GaN is known to be better suitable for electronic applications [246].

Once a high coverage on a monophase will be achieved on Au(111) a direct characterization of the electronic properties should be performed by ARPES available at the SGM3 beamline. Such a technique, sustained by spatially resolved STS analysis, could help to understand the topology of the band structure and to spot topologically non trivial edge states [247], possibly

paving the way for future integration in electronic devices [248].

Not only STS, but also sub-micrometer spatially-resolved ARPES (nano-ARPES) could be an efficient tool to measure the full spatial- and angle-resolved band structure [249]. A new nano-ARPES end station is actually on the way to be assembled by our group at Aarhus University [250]. For instance, considering the actual growth products as presented in Sec. 5.3.2 it seems advantageous to exploit the joint presence of SL TaP and BlueP at the surface to study the electronic structures of laterally interfacing atomic monolayers, especially if larger domains could be grown at the surface. For example, lateral epitaxy of WS_2 on MoS_2 edges was carried out and resulted in strong photoluminescence enhancement and intrinsic p-n junctions at the edges [251]. Unfortunately, nano-ARPES has not reached yet a sufficiently high spacial resolution to accurately image the band structure along lateral interfaces, but the electronic structure of microscopic single crystalline domains, if sufficiently large, could be accessed [252]. In fact, even though the spot sizes of the relatively close nanoARPES branch of I05 beamline based in Oxford (UK) is approximately $(0.7\times0.7)\ \mu m^2$ [253], it could be still appealing to explore the complex interplay of a BlueP/SL TaP intra-plane heterostructure, as the one shown in Fig. 6.1(d).

Bibliography

[1] K. C. Christoforidis. 2D materials for solar fuels production. In Zafeiratos, editor, *Micro Nano Technol.*, pp. 271–288. Elsevier (2020).

[2] N. D. Mermin. Crystalline order in two dimensions. *Phys. Rev.*, **176**, 250 (1968).

[3] S. Hagstrom, et al. Surface structures on the clean platinum (100) surface. *Phys. Rev. Lett.*, **15**, 491 (1965).

[4] J. W. May. Platinum surface LEED rings. *Surf. Sci.*, **17**, 267 (1969).

[5] J. C. Shelton, et al. Equilibrium segregation of carbon to a nickel (111) surface: A surface phase transition. *Surf. Sci.*, **43**, 493 (1974).

[6] K. S. Novoselov, et al. Electric field effect in atomically thin carbon films. *Science*, **306**, 666 (2004).

[7] A. K. Geim. Random walk to graphene (Nobel lecture). *Angew. Chemie Int. Ed.*, **50**, 6966 (2011).

[8] K. S. Novoselov, et al. Two-dimensional gas of massless Dirac fermions in graphene. *Nature*, **438**, 197 (2005).

[9] P. R. Wallace. The Band Theory of Graphite. *Phys. Rev.*, **71**, 622 (1947).

[10] K. F. Mak, et al. Atomically thin MoS_2: A new direct-gap semiconductor. *Phys. Rev. Lett.*, **105**, 136805 (2010).

[11] M. Donarelli and L. Ottaviano. 2D materials for gas sensing applications: A review on graphene oxide, MoS_2, WS_2 and phosphorene. *Sensors*, **18**, 3638 (2018).

[12] M. Eichberger, et al. Snapshots of cooperative atomic motions in the optical suppression of charge density waves. *Nature*, **468**, 799 (2010).

[13] Z. Zhang, et al. Recent progress in the controlled synthesis of 2D metallic transition metal dichalcogenides. *Nanotechnology*, **30**, 182002 (2019).

[14] T. Yokoya. Fermi surface sheet-dependent superconductivity in 2H-$NbSe_2$. *Science*, **294**, 2518 (2001).

[15] B. Sipos, et al. From Mott state to superconductivity in 1T-TaS_2. *Nat. Mater.*, **7**, 960 (2008).

[16] X. Zhu, et al. Signature of coexistence of superconductivity and ferromagnetism in two-dimensional $NbSe_2$ triggered by surface molecular adsorption. *Nat. Commun.*, **7**, 11210 (2016).

[17] K. Xu, et al. Ultrathin nanosheets of vanadium diselenide: A metallic two-dimensional material with ferromagnetic charge-density-wave behavior. *Angew. Chemie Int. Ed.*, **52**, 10477 (2013).

[18] E. Navarro-Moratalla, et al. Enhanced superconductivity in atomically thin TaS_2. *Nat. Commun.*, **7**, 11043 (2016).

[19] C. L. Kane and E. J. Mele. Quantum spin Hall effect in graphene. *Phys. Rev. Lett.*, **95**, 226801 (2005).

[20] A. H. Castro Neto and F. Guinea. Impurity-induced spin-orbit coupling in graphene. *Phys. Rev. Lett.*, **103**, 026804 (2009).

[21] S. Xu, et al. Discovery of a Weyl fermion semimetal and topological Fermi arcs. *Science*, **349**, 613 (2015).

[22] S. M. Young, et al. Dirac semimetal in three dimensions. *Phys. Rev. Lett.*, **108**, 140405 (2012).

[23] S. Y. Xu, et al. Experimental discovery of a topological Weyl semimetal state in TaP. *Sci. Adv.*, **1**, e1501092 (2015).

[24] A. G. Ekeberg. Uplysning om ytter jordens egenskaper, i synnerhet i jämförelse med berylljorden: om de fossilier, hvari förstnämnde jord innehålles, samt om en ny uptäckt kropp af metallisk naturTantarum. *Vetenskaps Acad. Handl.*, **1**, 68 (1802).

[25] F. Andreatta. *Electronic structure of a van der Waals heterostructure: TaS_2 on graphene*. Master Thesis, Aarhus University (2017).

[26] G. Ertl, et al. *Handbook of heterogeneous catalysis*, Vol. 2. Citeseer (1997).

[27] O. Leistiko, et al. Electron and hole mobilities in inversion layers on thermally oxidized silicon surfaces. *IEEE Trans. Electron Devices*, **12**, 248 (1965).

[28] A. Baldan. Adhesively-bonded joints and repairs in metallic alloys, polymers and composite materials: Adhesives, adhesion theories and surface pretreatment. *J. Mater. Sci.*, **39**, 1 (2004).

[29] S. Das, et al. Beyond graphene: Progress in novel two-dimensional materials and van der Waals solids. *Annu. Rev. Mater. Res.*, **45**, 1 (2015).

[30] E. Abbe. Beiträge zur Theorie des Mikroskops und der mikroskopischen Wahrnehmung. *Arch. für mikroskopische Anat.*, **9**, 413 (1873).

[31] S. I. Park and C. F. Quate. Scanning tunneling microscope. *Rev. Sci. Instrum.*, **58**, 2010 (1987).

[32] G. Binnig, et al. Surface studies by scanning tunneling microscopy. *Phys. Rev. Lett.*, **49**, 57 (1982).

[33] P. Sutter. *Science of microscopy - Scanning tunneling microscopy in surface science*. Springer New York (2008).

[34] J. Tersoff and D. R. Hamann. Theory of the scanning tunneling microscope. *Phys. Rev. B*, **31**, 805 (1985).

[35] C. Bai. *Scanning tunneling microscopy and its application*. Physics and astronomy online library. Springer (2000).

[36] E. Anguiano, et al. Optimal conditions for imaging in scanning tunneling microscopy: Theory. *Rev. Sci. Instrum.*, **69**, 3867 (1998).

[37] O. Nishikawa, et al. Piezoelectric and electrostrictive ceramics for STM. *Surf. Sci.*, **181**, 210 (1987).

[38] E. Laegsgaard, et al. A fully automated, thimble-size scanning tunnelling microscope. *J. Microsc.*, **152**, 663 (1988).

[39] E. Laegsgaard, et al. A high-pressure scanning tunneling microscope. *Rev. Sci. Instrum.*, **72**, 3537 (2001).

[40] J. B. Pendry. *Low energy electron diffraction: the theory and its application to determination of surface structure*. Academic Press (1974).

[41] M. A. VanHove, et al. *Low-energy electron diffraction: Experiment, theory and surface structure determination*, Vol. 6. Springer (2012).

[42] P. Hofmann. *Surface physics: An introduction* (2013).

[43] M. P. Seah and W. A. Dench. Quantitative electron spectroscopy of surfaces: A standard data base for electron inelastic mean free paths in solids. *Surf. Interface Anal.*, **1**, 2 (1979).

[44] J. Szajman, et al. Is there a universal mean-free-path curve for electron inelastic scattering in solids? *J. Electron Spectros. Relat. Phenomena*, **23**, 97 (1981).

[45] W. H. Miller. *A treatise on crystallography*. Cambridge: Pitt Press (1839).

[46] W. Friedrich, et al. Interferenzerscheinungen bei Röntgenstrahlen. *Ann. Phys.*, **346**, 971 (1913).

[47] H. Hertz. Ueber einen Einfluss des ultravioletten Lichtes auf die electrische Entladung. *Ann. der Phys. und Chemie*, **267**, 983 (1887).

[48] A. Einstein. Über einen die Erzeugung und Verwandlung des Lichtes betreffenden heuristischen Gesichtspunkt. *Ann. Phys.*, **322**, 132 (1905).

[49] A. Damascelli. Probing the electronic structure of complex systems by ARPES. *Phys. Scr.*, **2004**, 61 (2004).

[50] G. Grosso and G. P. Parravicini. *Solid state physics*. Elsevier LTD, Oxford (2013).

[51] M. Born. Zur Quantenmechanik der Stoßvorgänge. *Zeitschrift für Phys.*, **37**, 863 (1926).

[52] F. Bloch. Über die Quantenmechanik der Elektronen in Kristallgittern. *Zeitschrift für Phys.*, **52**, 555 (1929).

[53] C. Kittel, et al. *Introduction to solid state physics*, Vol. 8. Wiley New York (1996).

[54] G. D. Mahan. Theory of photoemission in simple metals. *Phys. Rev. B*, **2**, 4334 (1970).

[55] R. Matzdorf. Investigation of line shapes and line intensities by high-resolution UV-photoemission spectroscopy: Some case studies on noble-metal surfaces. *Surf. Sci. Rep.*, **30**, 153 (1998).

[56] R. L. Kronig. On the theory of dispersion of X-rays. *J. Opt. Soc. Am.*, **12**, 547 (1926).

[57] M. Bianchi, et al. Electron-phonon coupling in potassium-doped graphene: Angle-resolved photoemission spectroscopy. *Phys. Rev. B*, **81**, 41403 (2010).

[58] F. Reinert and S. Hüfner. Photoemission spectroscopy - From early days to recent applications. *New J. Phys.*, **7**, 97 (2005).

[59] S. Ulstrup, et al. Ultrafast electron dynamics in epitaxial graphene investigated with time- and angle-resolved photoemission spectroscopy. *J. Condens. Matter Phys.*, **27**, 164206 (2015).

[60] Z. Tao, et al. Direct time-domain observation of attosecond final-state lifetimes in photoemission from solids. *Science*, **353**, 62 (2016).

[61] G. Rohde, et al. Time-resolved ARPES with sub-15 fs temporal and near Fourier-limited spectral resolution. *Rev. Sci. Instrum.*, **87**, 103102 (2016).

[62] C. L. Smallwood, et al. Tracking cooper pairs in a cuprate superconductor by ultrafast angle-resolved photoemission. *Science*, **336**, 1137 (2012).

[63] C. Monney, et al. Revealing the role of electrons and phonons in the ultrafast recovery of charge density wave correlations in 1T-$TiSe_2$. *Phys. Rev. B*, **94** (2016).

[64] M. Ferray, et al. Multiple-harmonic conversion of 1064 nm radiation in rare gases. *J. Phys. B*, **21**, L31 (1988).

[65] S. Mathias, et al. Time-resolved photoelectron spectroscopy at surfaces using femtosecond XUV pulses. In *Dyn. Solid State Surfaces Interfaces*, Wiley Online Books, Ch. 21, pp. 499–535. John Wiley & Sons (2010).

[66] S. Ulstrup. *A direct study of the electronic structure of graphene: Tunability, many-body interactions and ultrafast Dirac fermions*. PhD thesis, Aarhus University (2014).

[67] F. Boschini, et al. Role of matrix elements in the time-resolved photoemission signal. *New J. Phys.*, **22**, 23031 (2020).

[68] S. Passlack, et al. Space charge effects in photoemission with a low repetition, high intensity femtosecond laser source. *J. Appl. Phys.*, **100**, 024912 (2006).

[69] S. Hellmann, et al. Vacuum space-charge effects in solid-state photoemission. *Phys. Rev. B*, **79**, 035402 (2009).

[70] S. Ulstrup, et al. Ramifications of optical pumping on the interpretation of time-resolved photoemission experiments on graphene. *J. Electron Spectros. Relat. Phenomena*, **200**, 340 (2015).

[71] L. Miaja-Avila, et al. Laser-assisted photoelectric effect from surfaces. *Phys. Rev. Lett.*, **97**, 113604 (2006).

[72] S. V. Hoffmann, et al. An undulator-based spherical grating monochromator beamline for angle-resolved photoemission spectroscopy. *Nucl. Instruments Methods Phys. Res. Sect. A Accel. Spectrometers, Detect. Assoc. Equip.*, **523**, 441 (2004).

[73] N. Hertel and S. V. Hoffmann. ASTRID2: A new Danish low-emittance SR source. *Synchrotron Radiat. News*, **24**, 19 (2011).

[74] I. C. E. Turcu, et al. Ultrafast science and development at the Artemis facility. In *Conf. Opt. Micro- to Nanophotonics II*. Vol. 7469, p. 746902. Society of Photo-Optical Instrumentation Engineers (2010).

[75] F. Frassetto, et al. Single-grating monochromator for extreme-ultraviolet ultrashort pulses. *Opt. Express*, **19**, 19169 (2011).

[76] C. Cacho, et al. Mid-IR pump, EUV probe femtosecond time-and-angle-resolved photoemission spectroscopy. In *19th International Conference on Ultrafast Phenomena*. Optical Society of America (2014).

[77] F. Andreatta, et al. Transient hot electron dynamics in single-layer TaS_2. *Phys. Rev. B*, **99**, 165421 (2019).

[78] J. A. Wilson and A. D. Yoffe. The transition metal dichalcogenides discussion and interpretation of the observed optical, electrical and structural properties. *Adv. Phys.*, **18**, 193 (1969).

[79] M. Chhowalla, et al. The chemistry of two-dimensional layered transition metal dichalcogenide nanosheets. *Nat. Chem.*, **5**, 263 (2013).

[80] F. Arnold. *Synthesis, structure and electronic properties of novel single layer transition metal chalcogenides*. Phd thesis, Aarhus University (2017).

[81] H. Sade, et al. Testing of $WS2_2$ nanoparticles functionalized by a humin-like shell as lubricant additives. *Lubricants*, **6**, 3 (2018).

[82] A. Kuc. Low-dimensional transition-metal dichalcogenides. In *Chem. Model.*, Vol. 11, pp. 1–29. The Royal Society of Chemistry (2015).

[83] J. Shi, et al. Physical properties and potential applications of two-dimensional metallic transition metal dichalcogenides. *Coord. Chem. Rev.*, **376**, 1 (2018).

[84] M. M. Ugeda, et al. Characterization of collective ground states in single-layer $NbSe_2$. *Nat. Phys.*, **12**, 92 (2016).

[85] Y. Yu, et al. Gate-tunable phase transitions in thin flakes of 1T-TaS_2. *Nat. Nanotechnol.*, **10**, 270 (2015).

[86] Y. Yang, et al. Enhanced superconductivity upon weakening of charge density wave transport in 2H-TaS_2 in the two-dimensional limit. *Phys. Rev. B*, **98**, 035203 (2018).

[87] F. Bonaccorso, et al. Graphene, related two-dimensional crystals, and hybrid systems for energy conversion and storage. *Science*, **347**, 1246501 (2015).

[88] S. Bae, et al. Roll-to-roll production of 30-inch graphene films for transparent electrodes. *Nat. Nanotechnol.*, **5**, 574 (2010).

[89] Y. H. Huang, et al. Electronic transport in $NbSe_2$ two-dimensional nanostructures: semiconducting characteristics and photoconductivity. *Nanoscale*, **7**, 18964 (2015).

[90] Y. Liu, et al. Self-optimizing, highly surface-active layered metal dichalcogenide catalysts for hydrogen evolution. *Nat. Energy*, **2**, 17127 (2017).

[91] Y. Yu, et al. High phase-purity 1T′-MoS_2 and 1T′-$MoSe_2$ layered crystals. *Nat. Chem.*, **10**, 638 (2018).

[92] J. L. Smith and P. J. Stiles. Electron-electron interactions continuously variable in the range $2.1 > r_s > 0.9$. *Phys. Rev. Lett.*, **29**, 102 (1972).

[93] A. A. Shashkin, et al. Spin-independent origin of the strongly enhanced effective mass in a dilute 2D electron system. *Phys. Rev. Lett.*, **91**, 046403 (2003).

[94] Z. Wan, et al. Induced superconductivity in high-mobility two-dimensional electron gas in gallium arsenide heterostructures. *Nature Commun.*, **6**, 7426 EP (2015).

[95] V. M. Pudalov, et al. Low-density spin susceptibility and effective mass of mobile electrons in Si inversion layers. *Phys. Rev. Lett.*, **88**, 196404 (2002).

[96] A. Bostwick, et al. Quasiparticle dynamics in graphene. *Nature Phys.*, **3**, 36 (2007).

[97] I. Pletikosic, et al. Dirac cones and minigaps for graphene on Ir(111). *Phys. Rev. Letters*, **102**, 056808 (2009).

[98] R. Larciprete, et al. Oxygen switching of the epitaxial graphene–metal interaction. *ACS Nano*, **6**, 9551 (2012).

[99] S. Ulstrup, et al. Sequential oxygen and alkali intercalation of epitaxial graphene on Ir(111): enhanced many-body effects and formation of pn-interfaces. *2D Materials*, **1**, 025002 (2014).

[100] S. Ulstrup, et al. Manifestation of nonlocal electron-electron interaction in graphene. *Phys. Rev. B*, **94**, 081403 (2016).

[101] G. Giuliani and G. Vignale. *Quantum theory of the electron liquid*. Cambridge University Press, 1^{st} ed. (2008).

[102] Y. Zhang and S. Das Sarma. Temperature-dependent effective mass renormalization in a Coulomb Fermi liquid. *Phys. Rev. B*, **70**, 035104 (2004).

[103] P. Coleridge, et al. Effective masses in high-mobility 2D electron gas structures. *Surf. Sci.*, **361-362**, 560 (1996).

[104] D.-H. Shin, et al. Analysis of quantum lifetime behaviour in modulation-doped n-channel $Si/Si_{1-x}Ge_x$ structures. *Semicond. Sci. Technol.*, **13**, 1106 (1998).

[105] J. C. Johannsen, et al. Direct view of hot carrier dynamics in graphene. *Phys. Rev. Lett.*, **111**, 027403 (2013).

[106] L. Perfetti, et al. Time evolution of the electronic structure of $1T-TaS_2$ through the Insulator-Metal Transition. *Phys. Rev. Lett.*, **97**, 067402 (2006).

[107] J. C. Petersen, et al. Clocking the melting transition of charge and lattice order in 1T-TaS_2 with ultrafast extreme-ultraviolet angle-resolved photoemission spectroscopy. *Phys. Rev. Letters*, **107**, 177402 (2011).

[108] T. Rohwer, et al. Collapse of long-range charge order tracked by time-resolved photoemission at high momenta. *Nature*, **471**, 490 (2011).

[109] S. Hellmann, et al. Time-domain classification of charge-density-wave insulators. *Nature Commun.*, **3**, 1069 EP (2012).

[110] C. Monney, et al. Revealing the role of electrons and phonons in the ultrafast recovery of charge density wave correlations in 1*T*-$TiSe_2$. *Phys. Rev. B*, **94**, 165165 (2016).

[111] H. M. Ahmad, et al. Effects of impurities on the electrochemical characterization of liquid-phase exfoliated niobium diselenide nanosheets. *J. Phys. Chem. C*, **123**, 8671 (2019).

[112] T. Ginley, et al. Topological insulator film growth by molecular beam epitaxy: A review. *Crystals*, **6**, 154 (2016).

[113] S. Manzeli, et al. 2D transition metal dichalcogenides. *Nat. Rev. Mater.*, **2**, 17033 (2017).

[114] H. Lin, et al. Growth of atomically thick transition metal sulfide films on graphene/6H-SiC(0001) by molecular beam epitaxy. *Nano Res.*, **11**, 4722 (2018).

[115] T. Shimada, et al. Polytypes and charge density waves of ultrathin TaS_2 films grown by van der Waals epitaxy. *Surf. Sci.*, **291**, 57 (1993).

[116] C. E. Sanders, et al. Crystalline and electronic structure of single-layer TaS_2. *Phys. Rev. B*, **94**, 081404(R) (2016).

[117] J. Hall, et al. Molecular beam epitaxy of quasi-freestanding transition metal disulphide monolayers on van der Waals substrates: a growth study. *2D Mater.*, **5**, 25005 (2018).

[118] J. Hall, et al. Environmental control of charge density wave order in monolayer 2H-TaS_2. *ACS Nano*, **13**, 10210 (2019).

[119] H. M. Lefcochilos-Fogelquist, et al. Substrate-induced suppression of charge density wave phase in monolayer 1H-TaS_2 on Au(111). *Phys. Rev. B*, **99**, 174113 (2019).

[120] X. Z. Yu, et al. New synthesis method for the growth of epitaxial graphene. *J. Electron Spectros. Relat. Phenomena*, **184**, 100 (2011).

[121] M. Dendzik. *Growth and electronic structure of single-layered transition metal dichalcogenides*. PhD thesis, Aarhus University (2016).

[122] J. A. Miwa, et al. Van der Waals epitaxy of two-dimensional MoS_2-Graphene heterostructures in ultrahigh vacuum. *ACS Nano*, **9**, 6502 (2015).

[123] S. G. Sørensen, et al. Structure and electronic properties of in situ synthesized single-layer MoS_2 on a gold surface. *ACS Nano*, **8**, 6788 (2014).

[124] L. Bellucci, et al. From the buffer layer to graphene on silicon carbide: Exploring morphologies by computer modeling. *Front. Mater.*, **6**, 198 (2019).

[125] J. Walter, et al. Electron diffraction and scanning tunneling microscope studies of $TaCl_5$-graphite intercalation compounds. *Carbon N. Y.*, **36**, 1277 (1998).

[126] D. W. Boukhvalov and M. I. Katsnelson. Destruction of graphene by metal adatoms. *Appl. Phys. Lett.*, **95**, 23109 (2009).

[127] M. Sicot, et al. Size-selected epitaxial nanoislands underneath graphene Moiré on Rh(111). *ACS Nano*, **6**, 151 (2012).

[128] S. Schumacher, et al. Europium underneath graphene on Ir(111): Intercalation mechanism, magnetism, and band structure. *Phys. Rev. B*, **90**, 235437 (2014).

[129] F. Jellinek. The system tantalum-sulfur. *J. Less Common Met.*, **4**, 9 (1962).

[130] L. F. Mattheiss. Band structures of transition-metal-dichalcogenide layer compounds. *Phys. Rev. B*, **8**, 3719 (1973).

[131] A. Meetsma, et al. Structure of 2H-TaS_2. *Acta Crystallogr. Sect. C*, **46**, 1598 (1990).

[132] N. F. Hinsche and K. S. Thygesen. Electron-phonon interaction and transport properties of metallic bulk and monolayer transition metal dichalcogenide TaS_2. *2D Materials*, **5**, 015009 (2018).

[133] A. Y. Kuzin, et al. Reconstructed silicon surfaces for calibration of scanning tunnel microscopes. *Meas. Tech.*, **55**, 773 (2012).

[134] R. J. Hamers, et al. Scanning tunneling microscopy of Si(001). In H. Neddermeyer, editor, *Scanning tunneling microscopy. Perspectives in condensed matter physics (a critical reprint series)*, Vol. 6, pp. 118–132. Springer, Dordrecht (1986).

[135] G. R. Yazdi, et al. Growth of large area monolayer graphene on 3C-SiC and a comparison with other SiC polytypes. *Carbon N. Y.*, **57**, 477 (2013).

[136] K. Oura, et al. *Surface science: An introduction*. Advanced Texts in Physics. Springer Berlin Heidelberg (2013).

[137] Q. Ji, et al. Chemical vapour deposition of group-VIB metal dichalcogenide monolayers: engineered substrates from amorphous to single crystalline. *Chem. Soc. Rev.*, **44**, 2587 (2015).

[138] J. Shi, et al. Two-dimensional metallic $NiTe_2$ with ultrahigh environmental stability, conductivity, and electrocatalytic activity. *ACS Nano*, **14**, 9011 (2020).

[139] T. Ohta, et al. Controlling the electronic structure of bilayer graphene. *Science*, **313**, 951 (2006).

[140] J. A. Scarfe and H. P. Hughes. Core-level lineshapes in photoemission from transition-metal intercalates of TaS_2. *J. Phys. Condens. Matter*, **1**, 6865 (1989).

[141] L. Rettig, et al. Ultrafast dynamics of occupied quantum well states in Pb/Si(111). *New J. Phys.*, **14**, 023047 (2012).

[142] L. S. Yang, et al. Electron propagation from a photo-excited surface: implications for time-resolved photoemission. *Appl. Phys. A*, **116**, 8590 (2013).

[143] J. Kröger, et al. The photoemission Fermi edge as a sample thermometer? *J. Electron Spectrosc. Relat. Phenom.*, **113**, 241 (2001).

[144] A. Crepaldi, et al. Ultrafast photodoping and effective Fermi-Dirac distribution of the Dirac particles in Bi_2Se_3. *Phys. Rev. B*, **86**, 205133 (2012).

[145] S. Ulstrup, et al. Extracting the temperature of hot carriers in time- and angle-resolved photoemission. *Rev. Sci. Instrum.*, **85**, 013907 (2014).

[146] S. L. Yang, et al. Electron propagation from a photo-excited surface: Implications for time-resolved photoemission. *Appl. Phys. A Mater. Sci. Process.*, **116**, 85 (2014).

[147] W. Widdra, et al. Time-resolved core level photoemission: Surface photovoltage dynamics of the SiO_2/Si(100) interface. *Surf. Sci.*, **543**, 87 (2003).

[148] E. Jensen and E. W. Plummer. Experimental band structure of Na. *Phys. Rev. Letters*, **55**, 1912 (1985).

[149] J. E. Northrup, et al. Theory of quasiparticle energies in alkali metals. *Phys. Rev. Letters*, **59**, 819 (1987).

[150] A. L. Walter, et al. Effective screening and the plasmaron bands in graphene. *Phys. Rev. B*, **84**, 085410 (2011).

[151] B. Monserrat. Electron-phonon coupling from finite differences. *J. Phys. Condens. Matter*, **30**, 83001 (2018).

[152] R. L. Liboff and G. K. Schenter. Electron-phonon scattering contributions to metallic resistivity at 0 K. *Phys. Rev. B*, **54**, 16591 (1996).

[153] P. B. Allen. Empirical electron-phonon λ values from resistivity of cubic metallic elements. *Phys. Rev. B*, **36**, 2920 (1987).

[154] J. Bardeen, et al. Theory of Superconductivity. *Phys. Rev.*, **108**, 1175 (1957).

[155] G. Profeta, et al. Phonon-mediated superconductivity in graphene by lithium deposition. *Nat. Phys.*, **8**, 131 (2012).

[156] D. L. Duong, et al. Ab initio computation of the transition temperature of the charge density wave transition in $TiSe_2$. *Phys. Rev. B*, **92**, 245131 (2015).

[157] W. Kohn. Image of the Fermi surface in the vibration spectrum of a metal. *Phys. Rev. Lett.*, **2**, 393 (1959).

[158] M. Calandra, et al. Effect of dimensionality on the charge-density wave in few-layer 2H-$NbSe_2$. *Phys. Rev. B*, **80**, 241108 (2009).

[159] X. Xi, et al. Strongly enhanced charge-density-wave order in monolayer $NbSe_2$. *Nat. Nanotechnol.*, **10**, 765 (2015).

[160] J. B. Lee, et al. Comparison of Theoretical Models of Electron-Phonon Coupling in Thin Gold Films Irradiated by Femtosecond Pulse Lasers. *Mater. Trans.*, **52**, 547 (2011).

[161] P. Majchrzak, et al. Hot carrier-assisted switching of the electron-phonon interaction in 1T-VSe_2. arXiv:2011.06358 (2020).

[162] L. Perfetti, et al. Ultrafast electron relaxation in superconducting $Bi_2Sr_2CaCu_2O_{8+\delta}$ by time-resolved photoelectron spectroscopy. *Phys. Rev. Letters*, **99**, 197001 (2007).

[163] E. P. Silaeva, et al. Ultrafast electron dynamics and orbital-dependent thermalization in photoexcited metals. *Phys. Rev. B*, **98**, 094306 (2018).

[164] S. L. Johnson, et al. Watching ultrafast responses of structure and magnetism in condensed matter with momentum-resolved probes. *Struct. Dyn.*, **4**, 061506 (2017).

[165] F. Caruso, et al. Photoemission signatures of nonequilibrium carrier dynamics from first principles. *Phys. Rev. B*, **101**, 035128 (2020).

[166] P. B. Allen. Theory of thermal relaxation of electrons in metals. *Phys. Rev. Lett.*, **59**, 1460 (1987).

[167] S. Dal Conte, et al. Disentangling the electronic and phononic glue in a high-T_c superconductor. *Science*, **335**, 1600 (2012).

[168] P. L. Dulong and A. T. Petit. Recherches sur quelques points importans de la théorie de la chaleur. *Ann. Chim. Phys.*, **10**, 395 (1819).

[169] A. Einstein. Die Plancksche Theorie der Strahlung und die Theorie der spezifischen Wärme. *Ann. Phys.*, **327**, 180 (1906).

[170] P. Debye. Zur Theorie der spezifischen Wärmen. *Ann. Phys.*, **344**, 789 (1912).

[171] J. Xu, et al. Crystal structure, electrical transport, and magnetic properties of niobium monophosphide. *Inorg. Chem.*, **35**, 845 (1996).

[172] H. Weyl. Gravitation and the electron. *Proc. Natl. Acad. Sci.*, **15**, 323LP (1929).

[173] Z. K. Liu, et al. Evolution of the Fermi surface of Weyl semimetals in the transition metal pnictide family. *Nat. Mater.*, **15**, 27 (2016).

[174] C. Shekhar, et al. Extremely large magnetoresistance and ultrahigh mobility in the topological Weyl semimetal candidate NbP. *Nat. Phys.*, **11**, 645 (2015).

[175] M. R. van Delft, et al. Two- and three-dimensional superconducting phases in the Weyl semimetal TaP at ambient pressure. *Crystals*, **10**, 288 (2020).

[176] C. R. Rajamathi, et al. Weyl semimetals as hydrogen evolution catalysts. *Adv. Mater.*, **29**, 1 (2017).

[177] S. Chu, et al. Roadmap on solar water splitting: current status and future prospects. *Nano Futur.*, **1**, 022001 (2017).

[178] Z. W. Seh, et al. Combining theory and experiment in electrocatalysis: Insights into materials design. *Science*, **355**, eaad4998 (2017).

[179] J.-Y. You, et al. Two-dimensional Weyl half-semimetal and tunable quantum anomalous Hall effect. *Phys. Rev. B*, **100**, 64408 (2019).

[180] T. F. Jaramillo, et al. Identification of active edge sites for electrochemical H_2 evolution from MoS_2 nanocatalysts. *Science*, **317**, 100 (2007).

[181] Y. Shao, et al. Electronic, magnetic, and catalytic properties of thermodynamically stable two-dimensional transition-metal phosphides. *Chem. Mater.*, **29**, 8892 (2017).

[182] S. Zhou, et al. Phosphorus quantum dots as visible-light photocatalyst for water splitting. *Comput. Mater. Sci.*, **130**, 56 (2017).

[183] V. Tran, et al. Layer-controlled band gap and anisotropic excitons in few-layer black phosphorus. *Phys. Rev. B*, **89**, 235319 (2014).

[184] V. Tayari, et al. Two-dimensional magnetotransport in a black phosphorus naked quantum well. *Nat. Commun.*, **6**, 7702 (2015).

[185] L. Li, et al. Black phosphorus field-effect transistors. *Nat. Nanotechnol.*, **9**, 372 (2014).

[186] R. Fei, et al. Enhanced thermoelectric efficiency via orthogonal electrical and thermal conductances in phosphorene. *Nano Lett.*, **14**, 6393 (2014).

[187] Z. Zhu and D. Tománek. Semiconducting layered blue phosphorus: A computational study. *Phys. Rev. Lett.*, **112**, 1 (2014).

[188] J. Guan, et al. Phase coexistence and metal-insulator transition in few-layer phosphorene: A computational study. *Phys. Rev. Lett.*, **113**, 046804 (2014).

[189] B. Ghosh, et al. Electric field induced gap modification in ultrathin blue phosphorus. *Phys. Rev. B*, **91**, 115433 (2015).

[190] N. Liu and S. Zhou. Gas adsorption on monolayer blue phosphorus: Implications for environmental stability and gas sensors. *Nanotechnology*, **28**, 175708 (2017).

[191] J. L. Zhang, et al. Epitaxial growth of single layer blue phosphorus: A new phase of two-dimensional phosphorus. *Nano Lett.*, **16**, 4903 (2016).

[192] F. Arnold, et al. Electronic structure of $Fe_{1.08}Te$ bulk crystals and epitaxial FeTe thin films on Bi_2Te_3. *J. Phys. Condens. Matter*, **30**, 065502 (2018).

[193] S. P. Cooil, et al. In situ patterning of ultrasharp dopant profiles in silicon. *ACS Nano*, **11**, 1683 (2017).

[194] G. Scappucci, et al. Ultradense phosphorus in germanium delta-doped layers. *Appl. Phys. Lett.*, **94**, 162106 (2009).

[195] R. Chow and Y. G. Chai. A PH_3 cracking furnace for molecular beam epitaxy. *J. Vac. Sci. Technol. A*, **1**, 49 (1983).

[196] M. Dendzik, et al. Growth and electronic structure of epitaxial single-layer WS_2 on Au(111). *Phys. Rev. B*, **92**, 245442 (2015).

[197] S. S. Grønborg, et al. Synthesis of epitaxial single-layer MoS_2 on Au(111). *Langmuir*, **31**, 9700 (2015).

[198] J. V. Barth, et al. Scanning tunneling microscopy observations on the reconstructed Au(111) surface: Atomic structure, long-range superstructure, rotational domains, and surface defects. *Phys. Rev. B*, **42**, 9307 (1990).

[199] N. Haag, et al. Epitaxial growth of thermally stable cobalt films on Au(111). *New J. Phys.*, **18**, 103054 (2016).

[200] P. Maksymovych, et al. Surface bonding and dynamical behavior of the CH_3SH molecule on Au(111). *J. Phys. Chem. B*, **109**, 22463 (2005).

[201] S. Rousset, et al. Self-ordering of Au(111) vicinal surfaces and application to nanostructure organized growth. *J. Phys. Condens. Matter*, **15**, S3363 (2003).

[202] J. Hall, et al. Molecular beam epitaxy of quasi-freestanding transition metal disulphide monolayers on van der Waals substrates: A growth study. *2D Mater.*, **5**, 025005 (2018).

[203] A. J. Leavitt and T. P. Beebe. Chemical reactivity studies of hydrogen sulfide on Au(111). *Surf. Sci.*, **314**, 23 (1994).

[204] X. L. Zhou and J. M. White. A comparative study of PF_3, PH_3 and $P(CH_3)_3$ on clean, K-covered, and Cl-covered Ag(111). *Surf. Sci.*, **221**, 534 (1989).

[205] J. Zeng, et al. Half layer by half layer growth of a blue phosphorene monolayer on a GaN(001) substrate. *Phys. Rev. Lett.*, **118**, 046101 (2017).

[206] J. P. Xu, et al. One-dimensional phosphorus chain and two-dimensional blue phosphorene grown on Au(111) by molecular-beam epitaxy. *Phys. Rev. Mater.*, **1**, 061002 (2017).

[207] L. Vitali, et al. Trimer adatom structure of phosphorus on Ge(111). *Phys. Rev. B*, **63**, 165320 (2001).

[208] E. Golias, et al. Band renormalization of blue phosphorus on Au(111). *Nano Lett.*, **18**, 6672 (2018).

[209] W. Zhang, et al. Epitaxial synthesis of blue phosphorene. *Small*, **14**, 1804066 (2018).

[210] J. Zhuang, et al. Band gap modulated by electronic superlattice in blue phosphorene. *ACS Nano*, **12**, 5059 (2018).

[211] T. Besara, et al. Coexistence of Weyl physics and planar defects in the semimetals TaP and TaAs. *Phys. Rev. B*, **93**, 245152 (2016).

[212] H. C. Luan, et al. High-quality Ge epilayers on Si with low threading-dislocation densities. *Appl. Phys. Lett.*, **75**, 2909 (1999).

[213] F. Sojka, et al. To tilt or not to tilt: Correction of the distortion caused by inclined sample surfaces in low-energy electron diffraction. *Ultramicroscopy*, **133**, 35 (2013).

[214] M. A. Van Hove, et al. The surface reconstructions of the (100) crystal faces of iridium, platinum and gold: I. Experimental observations and possible structural models. *Surf. Sci.*, **103**, 189 (1981).

[215] S. Shaikhutdinov, et al. Hexagonal heterolayers on a square lattice: A combined STM and LEED study of FeO(111) on Pt(100). *Phys. Rev. B*, **62**, 7535 (2000).

[216] M. V. Bollinger, et al. One-dimensional metallic edge states in MoS_2. *Phys. Rev. Lett.*, **87**, 196803 (2001).

[217] S. S. Grønborg, et al. Visualizing hydrogen-induced reshaping and edge activation in MoS_2 and Co-promoted MoS_2 catalyst clusters. *Nat. Commun.*, **9**, 2211 (2018).

[218] H. Boller and E. Parthé. The transposition structure of NbAs and of similar monophosphides and arsenides of niobium and tantalum. *Acta Crystallogr.*, **16**, 1095 (1963).

[219] R. Elsner, et al. New metal-rich phosphides of niobium, tantalum and tungsten. *Nature*, **2**, 407 (1966).

[220] C. H. Min, et al. Orbital fingerprint of topological Fermi arcs in the Weyl semimetal TaP. *Phys. Rev. Lett.*, **122**, 116402 (2019).

[221] J. F. Moulder, et al. *Handbook of X-ray photoelectron spectroscopy*, Vol. 3. Perkin-Elmer Corporation (1981).

[222] J. Hauck. Structural relations between vanadium, niobium, tantalum hydrides and deuterides. *Acta Crystallogr. Sect. A*, **34**, 389 (1978).

[223] A. San-Martin and F. D. Manchester. The H-Ta (hydrogen-tantalum) system. *J. Phase Equilibria*, **12**, 332 (1991).

[224] L. Charlot. *Reaction of hydrogen with niobium and tantalum in the ART gas loop*. Technical report, Pacific Northweast Laboratory, Washington (U.S.) (1965).

[225] J. J. Rush, et al. Study of hydrogen diffusion in tantalum hydrides by inelastic neutron scattering. *J. Chem. Phys.*, **59**, 6570 (1973).

[226] M. R. Andrews. Reaction of gases with incendescent tantalum. *J. Am. Chem. Soc.*, **54**, 1845 (1932).

[227] C. A. Ventrice, et al. Stable reconstruction of the polar (111) surface of NiO on Au(111). *Phys. Rev. B*, **49**, 5773 (1994).

[228] L. Buimaga-Iarinca, et al. DFT study on cysteine adsorption mechanism on Au(111) and Au(110). *AIP Conf. Proc.*, **1565**, 29 (2013).

[229] J. Fallaque-Najar, et al. A theoretical approach of the ethanol adsorption on Au(100), Au(110) and Au(111) surfaces. *Surf. Sci.*, **689**, 121458 (2019).

[230] K. Shen, et al. Comparison of catalytic activity between Au(110) and Au(111) for the electro-oxidation of methanol and formic acid: Experiment and density functional theory calculation. *Electrochim. Acta*, **256**, 129 (2017).

[231] I. Villegas and J. L. Stickney. Preliminary studies of GaAs deposition on Au(100), (110), and (111) surfaces by electrochemical atomic layer epitaxy. *J. Electrochem. Soc.*, **139**, 686 (1992).

[232] J. Shi, et al. Substrate facet effect on the growth of monolayer MoS_2 on Au foils. *ACS Nano*, **9**, 4017 (2015).

[233] G. Binnig, et al. (111) facets as the origin of reconstructed Au(110) surfaces. *Surf. Sci.*, **131**, L379 (1983).

[234] T. Gritsch, et al. A scanning tunneling microscopy investigation of the structure of the Pt(110) and Au(110) surfaces. *Surf. Sci.*, **257**, 297 (1991).

[235] J. C. Campuzano, et al. Au(110) (1 x 2)-to-(1 x 1) phase transition: A physical realization of the two-dimensional Ising model. *Phys. Rev. Lett.*, **54**, 2684 (1985).

[236] R. Koch, et al. High-temperature STM investigation of Au(110), Pt(110) and Ag(110). *Surf. Sci.*, **454-456**, 543 (2000).

[237] R. M. Stan. *Epitaxial growth of single-layer metallic transition metal dichalcogenides: Structural and electronic properties*. PhD thesis, Aarhus University (2019).

[238] R. Foulston, et al. Mono- and multi-layer adsorption of an ionic liquid on Au(110). *Phys. Chem. Chem. Phys.*, **14**, 6054 (2012).

[239] F. Hiebel, et al. Self-assembly of acetate adsorbates drives atomic rearrangement on the Au(110) surface. *Nat. Commun.*, **7**, 13139 (2016).

[240] X. Zhao, et al. Physisorption-induced surface reconstruction and morphology changes: Adsorption of glycine on the Au(110) 1 x 2 surface. *Langmuir*, **18**, 3910 (2002).

[241] P. Guaino, et al. Long-range order in a multilayer organic film templated by a molecular-induced surface reconstruction: Pentacene on Au(110). *Appl. Phys. Lett.*, **85**, 2777 (2004).

[242] H. Walen, et al. Long-range displacive reconstruction of Au(110) triggered by low coverage of sulfur. *J. Phys. Chem. C*, **119**, 21000 (2015).

[243] S. Sun, et al. Experimental realization of one-dimensional metal-inorganic chain: Gold-phosphorus chain. *ACS Mater. Lett.*, **2**, 873 (2020).

[244] F. Schmitt, et al. Ultrafast electron dynamics in the charge density wave material $TbTe_3$. *New J. Phys.*, **13**, 63022 (2011).

[245] S. G. Sørensen, et al. Structure and electronic properties of in situ synthesized single-layer MoS2 on a gold surface. *ACS Nano*, **8**, 6788 (2014).

[246] X. Lou, et al. Epitaxial growth of $Mg_xCa_{1-x}O$ on GaN by atomic layer deposition. *Nano Lett.*, **16**, 7650 (2016).

[247] S. Tang, et al. Quantum spin Hall state in monolayer 1T'-WTe_2. *Nat. Phys.*, **13**, 683 (2017).

[248] Z. Q. Fan, et al. Improving performances of in-plane transition-metal dichalcogenide Schottky barrier field-effect transistors. *ACS Appl. Mater. Interfaces*, **10**, 19271 (2018).

[249] S. Hellmann, et al. Vacuum space-charge effects in nano-ARPES. *Phys. Rev. B*, **85**, 75109 (2012).

[250] S. Ulstrup. Experiments - Nanoscale and femtosecond electronic structure (2021).

[251] Y. Gong, et al. Vertical and in-plane heterostructures from WS_2/MoS_2 monolayers. *Nat. Mater.*, **13**, 1135 (2014).

[252] J. Avila, et al. Exploring electronic structure of one-atom thick polycrystalline graphene films: A nano angle resolved photoemission study. *Sci. Rep.*, **3**, 2439 (2013).

[253] M. Hoesch, et al. A facility for the analysis of the electronic structures of solids and their surfaces by synchrotron radiation photoelectron spectroscopy. *Rev. Sci. Instrum.*, **88**, 013106 (2017).